2024-01-04

Design, Development, and Examination of New Lightweight High-Entropy Alloy for Structural Applications

Alam, Intekhab

UNIVERSITY OF CALGARY

Design, Development, and Examination of New Lightweight High-Entropy Alloy for Structural

Applications

by

Intekhab Alam

A THESIS

SUBMITTED TO THE FACULTY OF GRADUATE STUDIES

IN PARTIAL FULFILMENT OF THE REQUIREMENTS FOR THE

DEGREE OF MASTER OF SCIENCE

GRADUATE PROGRAM IN MECHANICAL ENGINEERING

CALGARY, ALBERTA

JANUARY, 2024

Abstract

The use of lightweight materials for structural applications can reduce energy consumption and greenhouse gas emissions towards climate change mitigation. However, lightweight materials must be carefully designed without compromising strength and safety; hence the continued search for high specific-strength materials. This thesis contributes to these efforts: to discover, develop, and characterize lightweight high-entropy alloys (LHEAs) for structural applications.

Obtaining solid-solution (SS) in alloys instead of intermetallic (IM) compounds is usually desirable because IM compounds can detrimentally reduce ductility and corrosion resistance. HEAs are multi-principal element alloys in which complex pair-wise interactions between constituent elements can favour IM compound formation. As such, empirical rules for predicting SS formation (over IM compound) and crystal structure in HEAs exist—atomic size difference, enthalpy of mixing, mixing entropy, entropy to enthalpy ratio, Pauling electronegativity difference, and valence electron concentration. However, these rules break down.

This thesis first re-examines the empirical rules' effectiveness by conducting a systematic study that isolates the effect of processing pathways known to impact phase stability. A new conservative phase and SS formation criteria for AlTiCuZn-based LHEAs are proposed; the revised rules are verified by developing new LHEAs that are accurately predicted—$AlTi_{0.37}CuZn_{0.97}$ and $AlTi_{0.56}Cu_{1.24}Zn_{1.2}$. As a next step, the thermal degradation pattern of a new dual-phase $AlTi_{0.45}CuZn$ LHEA ($\rho = 5.71 \ g/cc$) from phase decomposition to evaporation was further investigated. Using multimodal advanced characterization techniques, $AlTi_{0.45}CuZn$ is found to be thermally-stable up to between 250 and 360 °C. Beyond this limit, multistep decomposition occurs: *phase decomposition* at ~360 °C forms Al-Ti phase off the $AlTi_{0.45}CuZn$ matrix due to the largest negative mixing enthalpy for Al-Ti than other binary pairs; Zn *evaporation* at ~750 °C due to its

faster evaporation rate than other constituent elements; and LHEA *melting* at 880 °C. The LHEA possesses sluggish grain growth and better nano-indentation hardness among other LHEAs of close density range due to combined grain size and phase strengthening effects. This work offers new insight into the processing-structure-properties relationship of LHEAs and further advances the field's understanding of LHEA thermal deteriorative behavior in structural applications at elevated temperatures.

Preface

This thesis is the author's original work containing four chapters. Among them, Chapter 2 is already published in a peer-reviewed journal, while Chapter 3 is submitted for publication in a reputable materials science journal. These works contribute towards the field of materials science and engineering, especially to the field of high-entropy alloys (HEAs). Since a manuscript-based format is used for this thesis, these chapters are copies of the submitted manuscripts. Chapter 2 focuses on the modification of empirical phase stability rules to design solid-solution HCP-phase containing HEAs, and it is published in a reputed materials science journal as:

> *I. Alam, M. A. Adaan-Nyiak, and A. A. Tiamiyu, "Revisiting the phase stability rules in the design of high-entropy alloys: A case study of quaternary alloys produced by mechanical alloying," Intermetallics, vol. 159, p. 107919, Aug. 2023, doi: 10.1016/j.intermet.2023.107919.*

Chapter 3 focuses on the thermal deteriorative behavior of novel $AlTi_{0.45}CuZn$ lightweight HEA for potential high-temperature structural applications, and it is submitted for peer-review in a reputed materials science journal as:

> *I. Alam, M. A. Adaan-Nyiak, S. Hwang, K. Kisslinger, M. Topsakal, E. Jossou, S. K. Gill, and A. A. Tiamiyu, "From phase decomposition to evaporation: A multi-modal evaluation of thermally-degraded model lightweight high-entropy alloy," (Submitted).*

It should be noted that some similar figures exist in both manuscripts; these are Figure 2.8 (a) and Figure 3.1 (b, c); and Figure 2.9 (c) and Fig. 3.2 (c).

It should also be noted that the author has co-authored three other papers (two of them are published and one of them is under review in different peer-reviewed journals) and filed a patent

during his MSc program. Although these works are not included in this thesis, they are mentioned below:

- *M. A. Adaan-Nyiak,* **I. Alam***, and A. A. Tiamiyu, "Ball milling process variables optimization for high-entropy alloy development using design of experiment and genetic algorithm," Powder Technol., vol. 427, p. 118766, Sep. 2023, doi: 10.1016/j.powtec.2023.118766.*

- *M. A. Adaan-Nyiak,* **I. Alam***, G. A. Arcuri, and A. A. Tiamiyu, "Design of Self-Stabilized Nanocrystalline High-Entropy Alloy," Materials and Des., vol. 236, p. 112482, 2023, doi: https://doi.org/10.1016/j.matdes.2023.112482.*

- *M. A. Adaan-Nyiak,* **I. Alam***, E. Jossou, S. Hwang, K. Kisslinger, S. K. Gill, and A. A. Tiamiyu, "Design and development of stable nanocrystalline high-entropy alloy: coupling self-stabilizing and "solute" grain boundary segregation effects," (Under review).*

- *A. A. Tiamiyu, M. A. Adaan-Nyiak, and* **I. Alam***, "Stable nanocrystalline high-entropy alloy, and the method of making the same," US Patent Application No. 63/587,563.*

Acknowledgements

Dedication

To

my family and friends

who have always supported me during the ups and downs of my life.

Table of Contents

List of Tables

List of Figures

Chapter 1: Introduction and Motivation

This chapter contains the background, motivations, objectives, thesis organization, and statement of contribution of this study. To avoid repetition, it only contains relevant literature that is not addressed in detail in the introduction sections of Chapters 2 and 3.

1.1   Background

1.1.1   Traditional Alloys

Exploration of metallic materials began with pure metals (e.g., Cu); afterwards, it gradually shifted towards binary (e.g., Cu-Ag and Fe-C), ternary (e.g., Al-Cr-Ni and Ni-Co-Al), and higher-order alloy systems [5,18]. For a long time, alloying was carried out to impart desirable material properties, which entails the addition of relatively small amounts of secondary elements as solutes to a primary element (solvent) [19,20]. For instance, Cu (solute) was added to Ag (solvent) to produce sterling silver which is used for coin-making since pure Ag is not durable, and steels mainly contain Fe with added C and Cr for improved strength and corrosion resistance, respectively [19,21]. Until now, about thirty practical alloy systems (typically a principal element and minor additions of multiple elements) have been developed which are named after their principal constituent, including Cu-, Ti-, Mg-, Fe-, Al-, and Ni-based alloys [22]. However, the total number of probable elemental combinations is significantly minimized by this "principal-constituent" approach; hence, the alloys that can be discovered via the traditional approach are nearly exhausted after many years of exploration [5,19]. By 1970s, most of the high-performance alloys that are currently in use were already developed; hence traditional alloys were considered to be close to exhaustion [22]. Since materials drive advancements in our society, improved high-

performance materials with unique mechanical and functional properties are constantly sought to meet the demand for such advancements.

1.1.2 High-entropy Alloys

A new class of alloy—high-entropy alloys (HEAs)—have emerged when traditional alloys are considered to be nearly exhausted [23]. HEA-related works were first published in 2004 by Yeh et al. [24] and Cantor et al. [25], which introduced new possibilities of alloy compositions and the capability to influence the solid-solution phase stability by regulating configurational entropy [6]. HEAs were initially defined to contain at least five major elements with 5-35 at.% concentration in solid-solution with no differentiation between solvent and solute; this offers a vast compositional space and the possibilities of 10^{100} new alloy systems that are unexplored, according to Cantor's conservative estimate [4,5]. Another definition of HEA is based on the concept of entropy. Configurational entropy of mixing that characterizes chaos or degree of randomness enhances as the number of constituent elements and their concentrations rises based on the following relation [5]:

$$\triangle S_{mix,ideal} = -R \sum_{i=1}^{n} c_i ln c_i \ .... \ .... \ .... \ (1.1)$$

where R is the gas constant, n is the total number of the constituent elements, and c_i is the molar fraction of the i-th component. For equiatomic quaternary, quinary, and senary alloys, the $\triangle S_{mix,ideal}$ values are calculated as $1.39R$, $1.61R$, and $1.79R$, respectively. Initially, as shown in **Figure 1.1(a)**, alloys were classified into four groups based on their $\triangle S_{mix,ideal}$ values: (i) HEAs with $\triangle S_{mix,ideal} > 1.61R$ for alloys with five or more principal elements, (ii) medium-entropy alloys (MEAs) with $1.61R \geq \triangle S_{mix,ideal} \geq 0.69R$ for alloys with two to four principal elements, (iii) low-entropy alloys (LEAs) with $\triangle S_{mix,ideal} < 0.69R$ for traditional alloys, and (iv) ultrapure
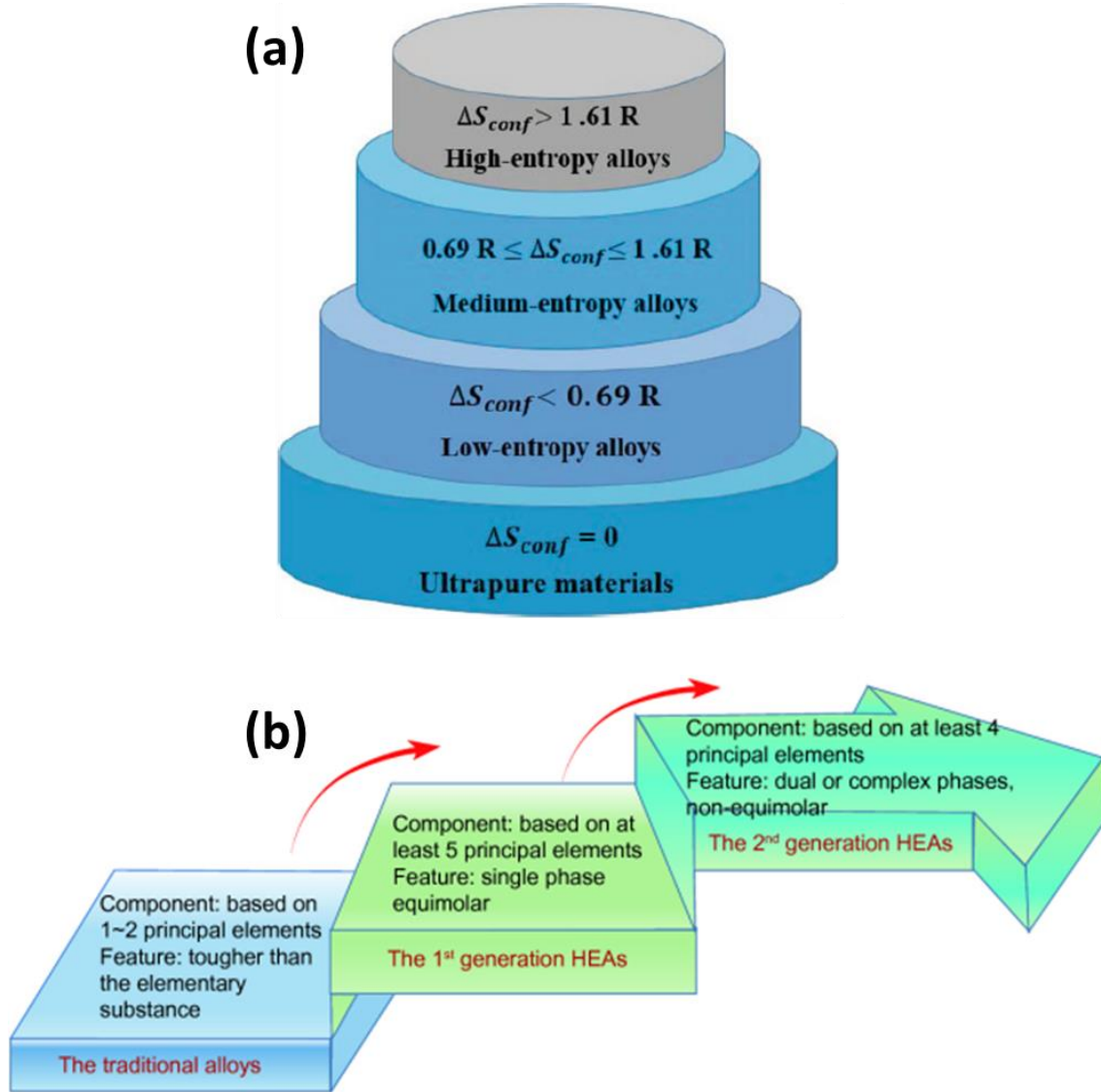
Figure 1.1: (a) Alloy classification based on the configurational entropy of mixing; **(b)** Alloy evolution from traditional alloys to 2nd generation HEAs. The figures (a) and (b) are reproduced from Ref. [1] and [2], respectively.

materials for which $\triangle S_{mix,ideal}$ is nearly 0 [1]. However, alloys with four principal elements in equimolar/non-equimolar ratios are now widely considered as HEAs [26,27]. These quaternary HEAs can be identified by $\triangle S_{mix,ideal} \geq 1.36R$ criterion [28]. The non-equiatomic quaternary HEAs have recently garnered attention because of the ease in tailoring phase stability to ensure superior mechanical properties; also, attractive dual-phase microstructure, twinning-induced plasticity (TWIP), and transformation-induced plasticity (TRIP) can be introduced in this type of

HEAs [26]. To summarize, although the 1st generation HEAs were initially restricted to single phase solid-solution HEAs with five or more major elements in an equiatomic ratio, the non-equiatomic HEAs with four or more major elements are now considered as the 2nd generation HEAs as illustrated in **Figure 1.1(b)**.

According to Yeh et al. [4], the high configurational entropy of HEAs would be adequate for the thermodynamic stabilization of a single-phase solid-solution by declining Gibbs free energy. So far, the primary single-phase solid-solution structures in HEAs are BCC, FCC, or HCP; and multiple phase structures such as BCC + HCP, BCC + FCC, and FCC + HCP have also been reported [7,29]. However, intermetallic (IM) compound phases can exist in HEAs, which detrimentally influence the alloy's performance by lowering its ductility [29]. Furthermore, if mechanical alloying—a solid-state non-equilibrium process widely used to produce nanocrystalline solid-solution HEAs—is adopted to develop HEAs [30,31], longer milling time can result in transforming the solid-solution phases into amorphous phases as observed in BeCoMgTi and BeCoMgTiZn low-density alloys [32].

1.1.3 Core Effects of High-entropy Alloys

HEAs have been extensively reported to possess excellent specific-strength and hardness, good resistance against oxidation, corrosion, and wear, improved magnetic properties, and outstanding thermal/structural stability, in comparison with their traditional alloy counterparts [23,33]. These excellent properties stem from four widely-accepted unique core effects: *high-entropy*, *sluggish diffusion*, *cocktail*, and *severe lattice distortion* [4], and they are discussed in detail in what follows:

- ***High entropy effect***: The high-entropy effect simply states that the higher the configurational mixing entropy in HEAs, the lower the solid-solution free energy that promotes their

4

formation, especially at elevated temperatures [20]. This can be realized by examining the thermodynamics of phase stability. Gibbs free energy in Eqn. (1.2) determines whether a reaction can win when the reaction is in competition with others [5]:

$$\Delta G_{mix} = \Delta H_{mix} - T\Delta S_{mix} \ldots \ldots \ldots (1.2)$$

where, T is the absolute temperature, ΔS_{mix} is the entropy of mixing—it quantifies system randomness at the atomic level, and ΔH_{mix} is the enthalpy of mixing—it quantifies the energy variation under fixed pressure and temperature. For solid-solution to form in HEA at the expense of IM compound, it is assumed that $\Delta H_{mix,ideal}^{SS} = 0$, thus $\Delta G_{mix,ideal}^{SS} = -T\Delta S_{mix,ideal}^{SS}$. Conversely, for perfectly-ordered IM compounds to form, it is assumed that $\Delta S_{mix,ideal}^{IM} = 0$, thus $\Delta G_{mix,ideal}^{IM} = \Delta H_{mix,ideal}^{IM}$. Due to the high entropy effect, $\Delta H_{mix,ideal}^{IM} > -T\Delta S_{mix,ideal}^{SS}$ (because $-T\Delta S_{mix,ideal}^{SS}$ reduces as $\Delta S_{mix,ideal}^{SS}$ increases) and in turn, $\Delta G_{mix,ideal}^{IM} > \Delta G_{mix,ideal}^{SS}$, thus solid-solution formation is favored in HEA instead of ordered IM compound [5,19]. However, IM compounds can sometimes be present in HEA when the competition between its enthalpy and entropy favors IM compound formation instead of a complete solid-solution [34]. Put differently, the dominant phase(s) depends on whether the free energies of the formation of IM compounds are more or less negative than the Gibbs free energy of mixing. Using three-elements model, the four possible competing mixing reactions are depicted in **Figure 1.2**: (i) where *single solid-solution* forms as only one phase is present in the lowest Gibbs free energy envelope for the whole composition range after competing with other phases [35], as shown in **Figure 1.2(a)**; (ii) where the *IM compound* forms in a solid-solution matrix as shown in **Figure 1.2(b)**, and the relevant change in free-energy is the total of the solid-
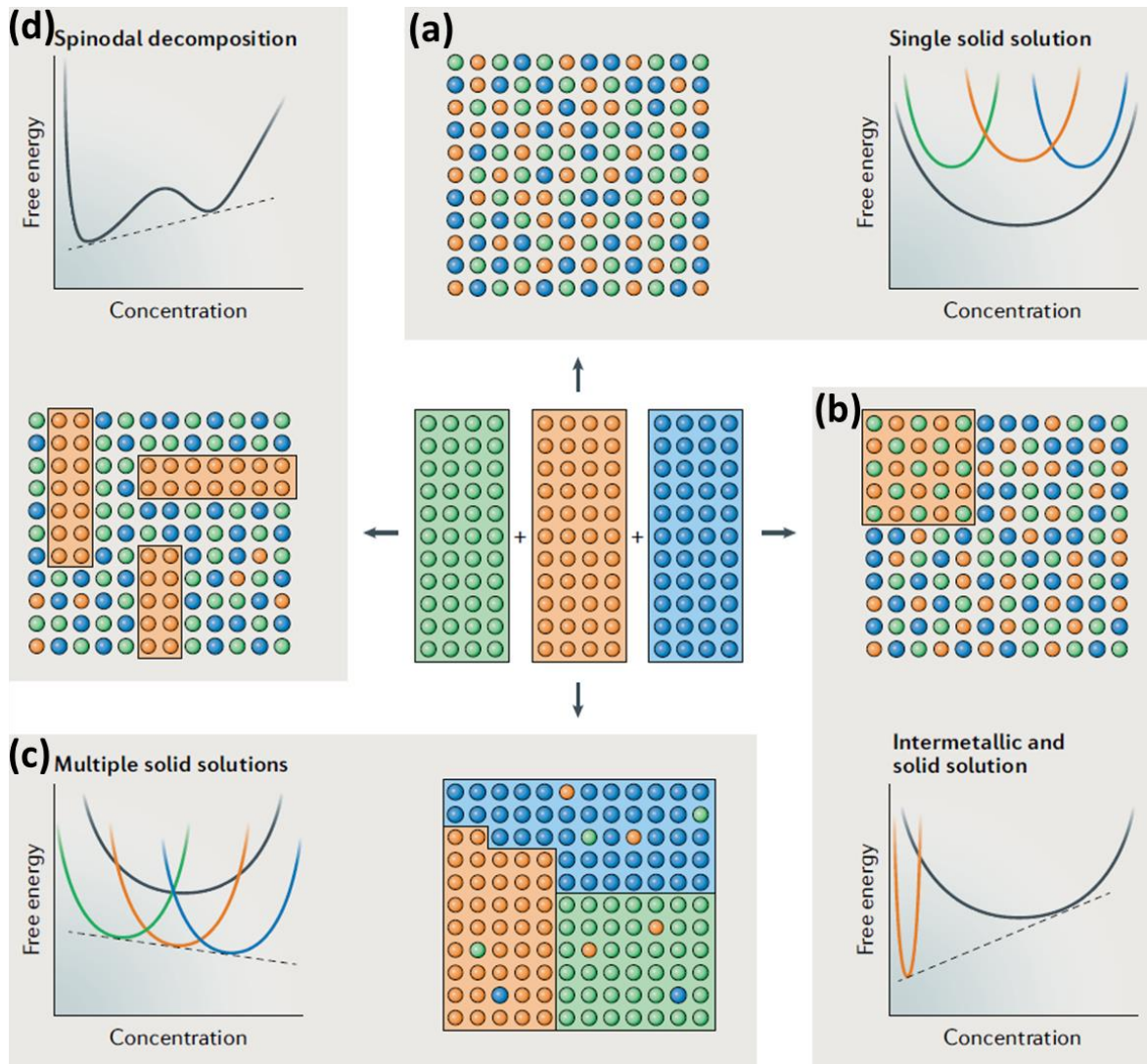
Figure 1.2: Probable reactions that can take place after mixing three distinct elements (green, red, and blue spheres) in equal ratios, such as **(a)** Single solid-solution formation; **(b)** Precipitation of IM compound in a solid-solution; **(c)** Multiple solid-solutions formation; and **(d)** Spinodal decomposition. The figure is reproduced from Ref. [19].

solution's free energy of mixing and IM compound's free energy of formation [19]; (iii) where the solution mixture decomposes into *multiple solid-solutions* to form varied crystal structures, compositions, and/or lattice parameters instead of a single solid-solution [19,36], so that the lowest Gibbs free energy envelope contains multiple phases in the whole composition range [35], as shown in **Figure 1.2(c)**; and (iv) where *spinodal decomposition* occurs because the curvature of the Gibbs free-energy curve is negative ($d^2G/dx^2 < 0$) for the

6

spinodal region, as shown in **Figure 1.2(d)**, and no thermodynamic barrier exists for the

reaction within the spinodal region [37].
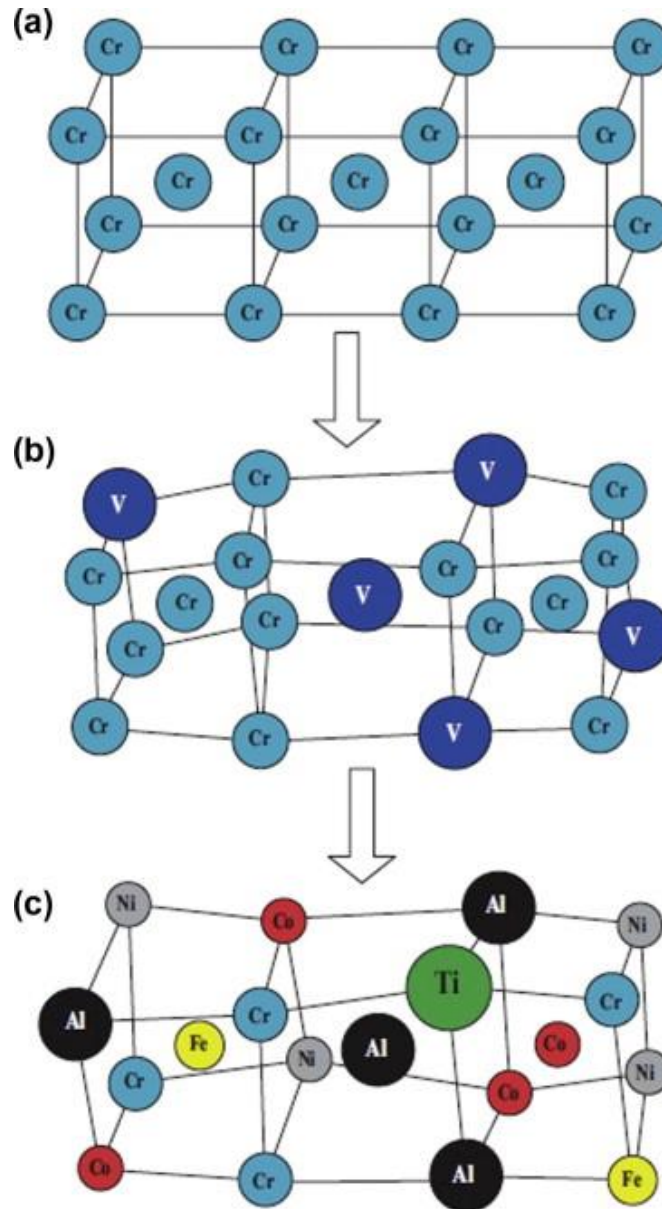
Figure 1.3: Schematic illustrations showing BCC structures: **(a)** Perfect lattice (e.g., Cr pure metal); **(b)** Distorted lattice after adding one solute element with different atomic radius to the solvent (e.g., Cr-V solid-solution binary alloy); **(c)** Severely distorted lattice due to various types of atoms with varied sizes randomly distributed in the crystal lattice; all these atoms have the same chance to occupy the lattice sites in $AlCoCrFeNiTi_{0.5}$ solid-solution HEA. The figures are reproduced from Ref. [3].

- ***Severe lattice distortion effect***: Compared to *pure metal* with no distortion—same atom type at the lattice sites (**Figure 1.3(a)**) and *dilute-binary alloys* with slight distortion—small amount of second atom at the lattice sites of host element (**Figure 1.3(b)**), the lattice distortion in HEAs is severe due to forced coexistence of multiple different-sized atoms in high concentration, as shown in **Figure 1.3(c)** [3,38]. The neighbors of larger atoms get pushed away by them (larger atoms), while smaller atoms possess additional space around them. The enhancement of HEA lattice's overall free energy occurs due to the strain energy incorporated with lattice distortion [20]. This affects the HEA characteristics, and the reasons behind this can be explained by the equation of the total yield strength, σ_y of HEAs [39]:

$$\sigma_y = \sigma_f + \varDelta\sigma_s \ldots \ldots \ldots (1.3)$$

where, σ_f denotes the lattice friction stress, and $\varDelta\sigma_s$ indicates the summation of all other possible strengthening effects that include solid-solution strengthening ($\varDelta\sigma_{ss}$), grain-boundary strengthening, dislocation strengthening, and precipitation strengthening. The higher the lattice distortion in a HEA, the higher the lattice resistance to dislocation movement, resulting in increased σ_f that improves the σ_y according to Eqn. (1.3) [20]. In other words, σ_f is an inherent strengthening contributor that originates from severe lattice distortion and can be expressed by: $\varDelta\sigma_f \propto E \cdot 3\delta$ relation, where E and δ are elastic modulus and lattice distortion, respectively [39].

In an equiatomic HEA where no solute atom exists and the lattice distortion is completely uniform and global, the σ_f will dominate and the $\varDelta\sigma_{ss}$ can be ignored [39,40]. However, in the case of non-equiatomic HEAs, it can be envisioned that deviation from an equiatomic composition enhances the contribution from $\varDelta\sigma_{ss}$. The $\varDelta\sigma_{ss}$ in HEAs is sourced from the elastic interactions between the local stress fields of "solute" atoms and surrounding

dislocations, which significantly contribute to σ_y [41,42]. The relationship between $\Delta\sigma_{ss}$ and δ can be established by the following equation [43,44]:

$$\Delta\sigma_{ss} = AG\delta^{4/3}C^{2/3} \ldots \ldots \ldots (1.4)$$

where, A is a dimensionless parameter that depends on the material, and it is of the order of 0.1, and G and C are the shear modulus of the alloy and the weighted-average of the concentration of atoms in solution, respectively.

- ***Cocktail effect***: The cocktail effect indicates that "mixing" different types of elements in an alloy can inadvertently result in outstanding properties [5]. These macroscopic properties emanate from the combination of properties induced by individual constituent elements, as well as those from the interactions among them [5,20]. For instance, MoNbTaVW HEA has 5250 MPa Vickers hardness, which is much higher than 1596 MPa as determined via the mixture rule [5]. Also, Al is a relatively "soft" element with a low melting point, but the
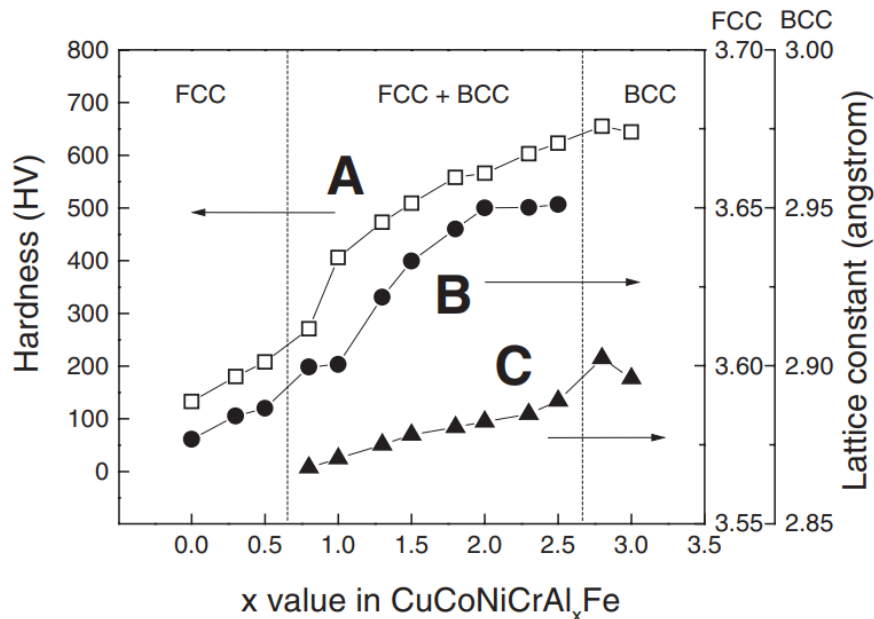
Figure 1.4: Hardness variation of $Al_xCoCrCuFeNi$ HEA with varying x values. The figure is reproduced from Ref. [4].

9

hardness of $Al_x CoCrCuFeNi$ HEA increases with increasing Al content as shown in **Figure 1.4**. Stronger cohesive bonding of Al with other constituent elements along with the larger atomic size of Al partially contributes to this hardening effect [20].

- ***Sluggish Diffusion***: HEAs are known to have slower diffusion kinetics as compared to traditional alloys [45]. This is because neighboring atoms of every lattice site in HEAs are dissimilar to a certain extent as opposed to a dilute-binary alloy system. Hence, local atomic configurations prior to and after an atom jumps into a vacancy are not the same in HEAs (resulting in varied local energies for every site); this is different in traditional alloys where local atomic configurations prior to and after an atom jumps into a vacancy are mostly identical [20]. The local atomic configurations difference in HEAs results in sluggish diffusion due to the combined effect of two jump scenarios: (i) an atom gets trapped after jumping into a low-energy site, then the atom will have a lower probability to jump out from that site; and (ii) for a high-energy site, the atom has a greater probability to jump back to its initial site [20].

Again, the diffusion rate varies from element to element in a HEA; for instance, high melting point elements have lower diffusion rates than lower melting point elements [20]. The elements with lower diffusion rates have lower success rates for jumping into vacancies as compared to other elements. As the coordinated diffusion of different types of elements is generally needed for the phase transformations, the elements with lower diffusion rates act as the rate-limiter, thus hindering phase transformation [20]. **Figure 1.5** shows the diffusion coefficients of nickel (D_{Ni}) in various FCC alloys (including HEAs) plotted against the inverse homologous temperature (T/T_m), with T_m representing the melting temperature. It is observed that alloys with increased compositional complexity generally display reduced

D_{Ni} at a given homologous temperature [5]. In application, this sluggish diffusion effect in HEA can be harnessed to develop multifunctional coatings with both outstanding diffusion barriers and greater structural stability, high-temperature strength, and creep resistance [20].
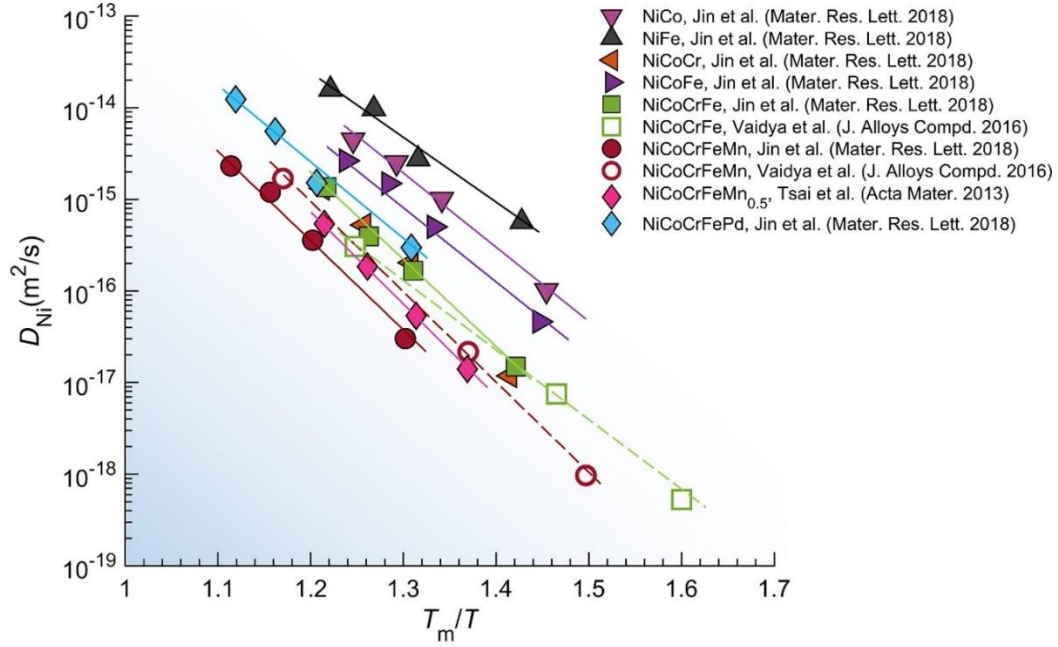
Figure 1.5: The diffusion coefficients of nickel in various Ni-based FCC alloys as a function of inverse homologous temperature. The figure is reproduced from Ref. [5].

Due to the four unique core effects, some interesting and unusual properties can be observed, derived, and tailored in HEAs. For instance, FCC-structured CoCrFeMnNi HEA has a significantly high fracture toughness, especially at cryogenic temperatures, and its strength and ductility improve at lower temperatures [46]. Again, for the first time, dual-phase $Fe_{50}Mn_{30}Co_{10}Cr_{10}$ HEA overcomes strength-ductility trade-off via a partial martensitic transformation [47].

1.1.4   Classification of High-entropy Alloys

Following the classifications provided by Miracle and Senkov [6], HEAs are classified into seven alloy families, which are provided in **Figure 1.6** and briefly discussed below:

- ***3d Transition metal-based HEAs***: This is the most widely investigated alloy family that usually possesses Al, Co, Cr, Ti, V, Cu, Fe, Mn, and Ni elements. The most popular example of this family is 'Cantor alloy' (CoCrFeMnNi), and the most common elemental groupings are AlCrFeNi, AlCoFeNi, AlCoCrNi, CoCrFeNi, and AlCoCrFe. They are mostly considered as extension of the traditional superalloys (heat-resistant alloys of Ni, Fe-Ni, and Co that frequently withstand temperatures greater than 1050 °C [48]) and stainless steels.

- ***Refractory metal HEAs***: The aim behind developing refractory metal HEAs was to introduce novel high-temperature structural metals. The primary elements of this alloy family are the refractory elements—Zr, Nb, Mo, Hf, Ta, Ti, V, Cr, and W. This type of HEA must contain at least four of these refractory elements; the most common element groupings are MoNbTaW, HfNbTaZr, CrMoNbTa, or CrNbVZr.

- ***Light metal or Low-density HEAs***: This alloy family was introduced to develop novel low-density structural alloys for applications in the aerospace and transportation sectors. The principal elements of this alloy family are Al, Be, Li, Mg, Sc, Si, Sn, Ti and Zn, and examples of this alloy family are $Al_{20}Li_{20}Mg_{10}Sc_{20}Ti_{30}$ [49] and AlMgSiCrFeNi [9]. Processing of this alloy family is difficult due to the presence of constituent elements with a wide range of melting and boiling points; hence, mechanical alloying solid-state process or careful choice of master alloys for liquid-state process is used for successfully developing this alloy family.

- ***Lanthanide transition metal HEAs***: This alloy family is simply born out of scientific curiosity to develop single-phase, solid-solution HCP-structured HEAs. They possess at least 4 of the lanthanide (4f) elements: Lu, Tb, Dy, Gd, and Tm, as well as the Y element. Examples of this alloy family are DyGdLuTbY and DyGdLuTbTm.

- ***HEA brasses and bronzes***: This class of HEA is still at its infant stage. The goal behind the development of these alloys is to attain greater strength levels (beyond the traditional brasses and bronzes) via concentrated solid-solutions. The primary constituent elements for this family include Al, Cu, Mn, Ni, Sn and Zn with a representative formula of $Al_xSn_yZn_z[CuMnNi]_{(1-x-y-z)}$.
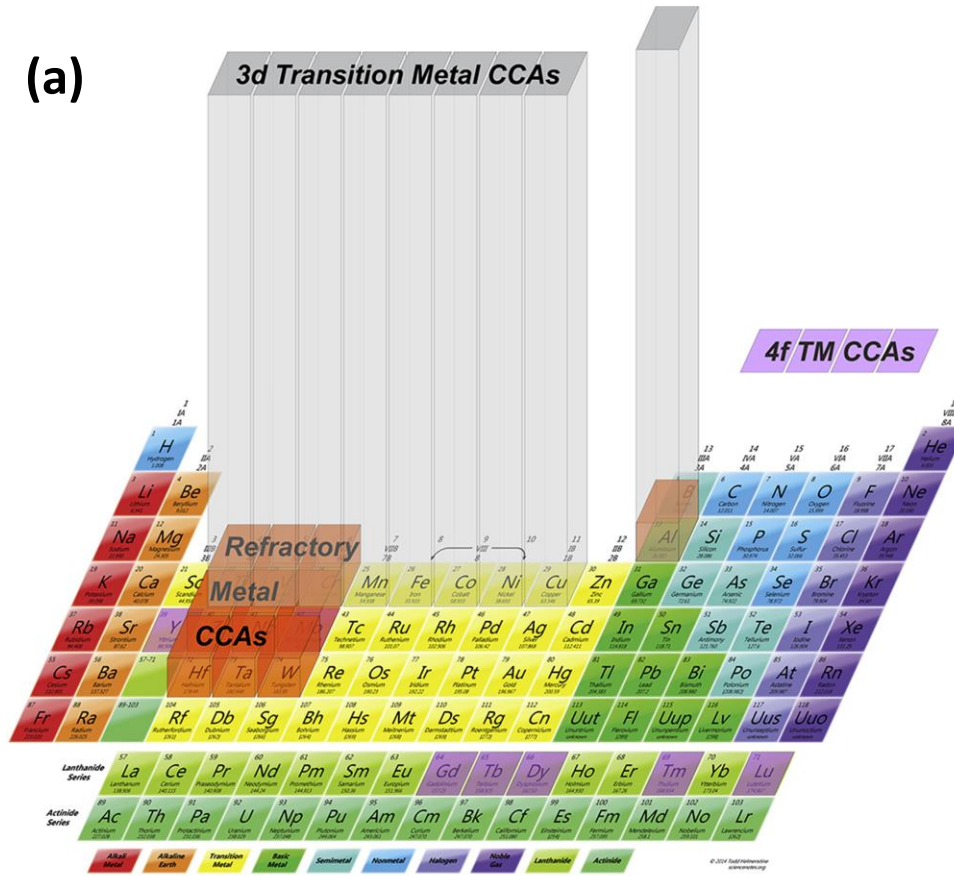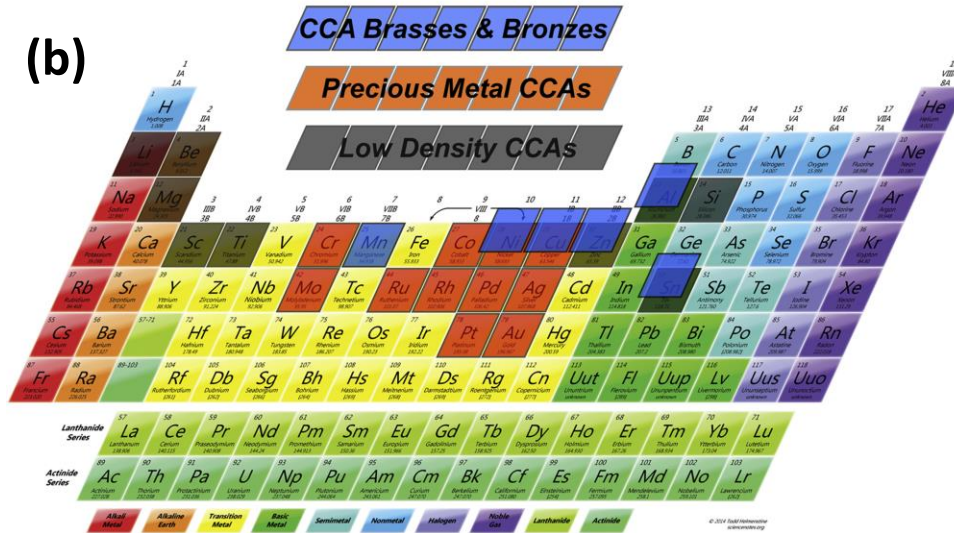
Figure 1.6: Classification of HEAs. **(a)** 345 3d transition metal HEAs, 29 refractory metal HEAs, and 2 lanthanide (4f) transition metal HEAs; and **(b)** 7 low-density HEAs, precious metal HEAs, and HEA brasses and bronzes. The figure is reproduced from Ref. [6].

- *Precious metal HEAs*: These alloys are mainly employed for catalysis applications, and they primarily include at least four of these elements: Ag, Au, Co, Cr, Cu, Ni, Pd, Pt, Rh, and Ru. A prior phase diagram study found a single-phase HCP MoPdRhRu alloy.

- *Interstitial compound HEAs*: In addition to containing elements from the 3d transition metal or refractory metal HEA families, this class of HEA contains B, C, or N. The presence of B, C, or N has a significant influence on the phases and microstructures of the alloys, and most of these alloys are developed as thin films.

In what follows, the lightweight HEAs (LHEAs) are discussed in more detail.

1.1.5 Lightweight High-entropy Alloys

LHEAs have the potential to be used in structural applications in transportation, aerospace, and energy sectors, where lowering the engineering components' weight is essential to improve energy efficiency [21,33]. These alloy classes usually have a density of less than 7 g/cc and show excellent oxidation resistance, good specific hardness and strength, and high wear and corrosion resistance [6,50]. As compared to traditional lightweight materials, LHEAs tend to show better mechanical properties; for example, $Al_{20}Li_{20}Mg_{10}Sc_{20}Ti_{30}$ LHEA and traditional aerospace Al-Cu alloys with comparable densities possess hardness values of 599 and 131 HV, respectively [33,51,52]. Also, compared to Ti-6Al-4V alloy (4.43 g/cc, 349 HV), $Al_{20}Be_{20}Fe_{10}Si_{15}Ti_{35}$ LHEA with a density of 3.91 g/cc shows a high hardness of 911 HV and improved oxidation resistance [53,54]. Other encouraging results have already been reported with respect to high-strength LHEA development; for instance, Stepanov et al. [55] produced BCC-structured AlNbTiV LHEA with a low density of 5.59 g/cc that possesses a high compressive yield strength of 1.02 GPa at room temperature. Senkov et al. [56] developed NbTiVZr (with 6.52 g/cc density), $NbTiV_2Zr$ (6.34 g/cc), NbTiCrZr

(6.67 g/cc), and NbTiCrVZr (6.57 g/cc) LHEAs with high Vickers microhardness values of 3.29, 2.99, 4.10, and 4.72 GPa, respectively, which are due to the presence of disordered BCC solid-solutions. According to Yang et al. [34], $Al_{80}Li_5Mg_5Zn_5Cu_5$ and $Al_{80}Li_5Mg_5Zn_5Sn_5$ low-density alloys possess outstanding compressive strengths of 879 and 836 MPa, respectively.

Other works also show the high specific strength and hardness of LHEAs; for example, Youssef et al. [49] produced mechanically-alloyed HCP-structured $Al_{20}Li_{20}Mg_{10}Sc_{20}Ti_{30}$ LHEA with low density of 2.67 g/cc but an ultra-high strength of ~2 GPa. $Mg_x(MnAlZnCu)_{100-x}$ LHEAs with HCP and Al-Mn icosahedral quasicrystalline phases were developed by Li et al. [57]; these alloys have densities between 2.20 and 4.29 g/cc and show good compressive strengths between 400 and 500 MPa at ambient temperature. According to Maulik et al. [58], $AlFeCuCrMg_x$ LHEAs have densities between 4.91 and 5.79 g/cc and hardness values between 533 and 853 HV; these high hardness values are due to the combined effect of solid-solution strengthening, grain size strengthening, and precipitation hardening. Du et al. [59] synthesized MgCaAlLiCu LHEA by casting method that has a single-phase tetragonal structure with a high compressive strength of 910 MPa. Among the potential applications of LHEAs, AlCoCrFeNiCu LHEA demonstrates its applicability as coatings on A301 steel, providing effective protection against mechanical failures that occur during aerospace structural applications [14]. BCC-structured $MgZrTiFe_{0.5}Co_{0.5}Ni_{0.5}$ LHEA produced by mechanical alloying is a potential candidate for hydrogen storage devices [60]. $Al_{2.08}CoCrFeNi$ LHEA has near-constant resistivity in 4.2-360 K temperature range, and thus can be employed in fabricating electronic device parts [38]. As the AlCoFeNiTi LHEA system shows superior binding properties, it can be applied as hard metal alloy binder [61]. LHEAs are also known to show superior thermal stability as compared to traditional Al-based alloys [50,55,62,63], which will be elaborately discussed in **Section 3.1** of **Chapter 3**. At the time of writing this thesis,

no Al-based dual phase (FCC + HCP) LHEA has been reported or developed (based on the author's knowledge) aside from the newly-discovered LHEA reported and investigated in this thesis.

1.2 Motivation

One of the most challenging research areas in materials science is to develop novel lightweight materials with high specific-strength and thermal stability for structural applications in the transportation, aerospace, and energy sectors. These lightweight materials, if developed, can contribute to the ongoing global efforts to improve energy efficiency—reduce fuel consumption by lowering the weight of structural components, and in turn, reduce greenhouse gas emissions to combat global warming issue. The widespread applications of lightweight materials are therefore sought after to replace the generally used heavier and energy-consuming materials. However, the main drawbacks of traditional lightweight materials are their lower mechanical properties in comparison with most high-density materials; these hampers their (lightweight materials) extensive use in structural applications, particularly at elevated temperatures. The discovery and development of a new class of lightweight materials, LHEA, has recently enabled researchers to access a combination of excellent properties that are not found in traditional lightweight materials, even at elevated temperatures.

This research takes advantage of the inherent moderately-high mechanical and functional properties in solid-solution LHEAs that are further optimized by the development of nanocrystalline structure. As such, the outcome of the research—newly developed LHEAs—can also be extended to develop hard lightweight coatings with functional properties. The successfully developed nanocrystalline solid-solution LHEA with improved mechanical properties and thermal stability can improve energy efficiency in the transportation, aerospace, and energy sectors and

can contribute to efforts to reduce emissions that detrimentally impact the environment. Overall, this research hopes to develop the "strongest among the lightest alloys" that will benefit the economy and environment via energy-efficiency improvement and greenhouse gas mitigation.

1.3 Objectives

The overall goal of this research is to discover, design, and develop new LHEAs for structural applications at elevated temperatures. The specific objectives are:

- Determine, develop, and characterize new solid-solution LHEAs. The effectiveness of the existing empirical rules for determining phase stability will be re-examined by conducting a systematic study that isolates the effect of processing pathways known to impact phase stability. *The manuscript in Chapter 2 addresses this objective.*

- Examine and determine the thermal degradation pattern of the newly developed LHEAs using multimodal characterization techniques, and their (LHEAs) mechanical response to external loading conditions. *The manuscript in Chapter 3 addresses this objective.*

1.4 Thesis Organization

Chapter 1 provides an overview of the pertinent literature that underpins and gives context to the following chapters, which is followed by the motivation and objectives of this study. **Chapter 2** discusses the assessment of classical empirical phase stability rules to design solid-solution HCP-phase containing-LHEAs. The theoretical and experimental results presented in this chapter show that the range of empirical phase stability model values varies based on the specific alloy being studied, which can be attributed to the distinct bonding characteristics of the constituent elements present in HEAs. **Chapter 3** represents the study of the thermal degradation pattern of novel

AlTi$_{0.45}$CuZn LHEA from phase decomposition to evaporation by using multi-modal characterisation techniques. It is observed that AlTi$_{0.45}$CuZn LHEA can potentially be used for structural applications even at elevated temperatures. In the end, **Chapter 4** offers a thorough summary of the research carried out in this thesis along with the necessary future research directions that can potentially transition this work to industry for scaling.

Statement of Contribution:

I. Alam is the author of this thesis and the first author of papers included here as Chapters 2 and 3. Dr. A. Tiamiyu is the supervisor of the author's MSc program and the corresponding author of both papers. Their contributions are as follows:

> *Intekhab Alam*: Writing- Original Draft, Conceptualization, Methodology, Formal Analysis, Investigation, Data Curation, Visualization, Validation.

> *Ahmed A. Tiamiyu*: Writing- Reviewing and Editing, Conceptualization, Investigation, Visualization, Validation, Funding acquisition, Supervision.

The contributions of other co-authors on the two papers are as follows: *Moses A. Adaan-Nyiak* (UofC) assisted with the ball milling experiment, some data curation, and in the review of the manuscript drafts, while *Sooyeon Hwang*, *Kim Kisslinger*, *Mehmet Topsakal*, *Ericmoore Jossou*, and *Simerjeet K. Gill*, all of Brookhaven National Laboratory, USA, provided resources (the use of FIB, STEM, and s-XRD facilities, and software trainings) and also reviewed the manuscript drafts.

Chapter 2: Revisiting the phase stability rules in the design of high-entropy alloys: A case study of quaternary alloys produced by mechanical alloying

Abstract

High-entropy alloys (HEAs) have the potential for many structural applications because of their outstanding mechanical properties. Achieving solid-solution (SS) in HEAs is desirable since intermetallic (IM) compounds can, in most cases, be deleterious. While empirical phase stability rules have been widely used to predict SS or IM compound phases in HEAs, there are substantial reported cases of their breakdown. To assess the effectiveness of the empirical rules—atomic size difference (δ), mixing enthalpy (ΔH_{mix}), mixing entropy (ΔS_{mix}), entropy to enthalpy ratio (Ω), electronegativity difference ($\triangle \chi$), and valence electron concentration (*VEC*), a systematic study that isolates the effect of processing pathway was conducted. As a starting point and as a benchmark, an existing equiatomic AlCoCrFe BCC HEA was correctly predicted (following the classical empirical rules) and developed. This was followed by the SS FCC prediction and development of five novel semi-equiatomic AlTiCuZn-based quaternary HEAs (Al$_{0.57}$TiCuZn, AlTi$_{0.45}$CuZn, Al$_{0.45}$TiCuZn, AlTiCu$_{1.76}$Zn, and AlTiCu$_2$Zn) by mechanical alloying. Among the AlTiCuZn-based HEAs, only AlTi$_{0.45}$CuZn showed SS, but with FCC+HCP phase contradicting the traditional VEC rule that predicts FCC. Using AlTi$_{0.45}$CuZn as a guide, conservative SS formation criteria for AlTiCuZn-based HEAs were determined—$\Omega \geq 1.6$, $\delta \leq 5\%$, and $\Delta H_{mix} \geq -8$ kJ/mol, while retaining conventional ΔS_{mix} and $\triangle \chi$ range. Also, FCC+HCP phase formation is stable at $7.5 \leq VEC \leq 8.4$. The revised rules were verified by correctly predicting the phases in newly-fabricated non-equiatomic HEAs—AlTi$_{0.37}$CuZn$_{0.97}$ and AlTi$_{0.56}$Cu$_{1.24}$Zn$_{1.2}$. This study shows the range of empirical phase stability model values is not fixed, but alloy-dependent due to the differences in bonding nature of HEA-constituting elements.

2.1 Introduction

High-entropy alloys (HEAs) are multi-principal element alloys that contain at least four principal elements with concentrations between 5 and 35 at% [27]. They exhibit four core effects such as high-entropy, sluggish diffusion, cocktail, and severe lattice distortion [4]. These core effects contribute to their excellent specific strength, impressive oxidation resistance, outstanding thermal stability, and good wear resistance, making them potential candidates for many structural applications [33]. The principal single-phase solid-solution (SS) structures in HEAs are BCC, FCC, or HCP [29]. However, the co-evolution of phases (BCC + HCP, BCC + FCC, FCC + HCP, and BCC + FCC + HCP), intermetallic (IM) compound phases, as well as amorphous phases can also develop in HEAs [32,64,65]. The presence of IM compounds in HEAs can be deleterious, and in most cases, their mechanical performances are impacted due to the lowering of their ductility which makes processing difficult; therefore, obtaining SS structures in HEAs is usually desirable [66].

To predict SS and crystal structure/phase stability of HEAs, various criteria such as atomic size difference (δ), enthalpy of mixing (ΔH_{mix}), mixing entropy (ΔS_{mix}), ratio of entropy to enthalpy value (Ω), Pauling electronegativity difference ($\triangle \chi$), and valence electron concentration (*VEC*) have been established based on thermodynamic and Hume-Rothery rules [33]. For crystal structure prediction, Guo et al. [67] proposed that the HEA systems (e.g., MoNbTaVW, AlCoCrCuFeNi, etc.), excluding the Mn-containing HEAs, fulfil the conditions that the HEAs with *VEC* < 6.87 have a BCC phase, *VEC* > 8.0 have a single FCC phase, and 6.87 < *VEC* < 8.0 have a dual FCC + BCC phase. Using AlCoCrFeNi alloy system as a case study, the VEC rule has recently been revised to BCC: 5.7 ≤ *VEC* ≤ 7.2 and FCC: *VEC* ≥ 8.4 [68]. In general, the VEC range has been

shown to be influenced by temperature, concentration, and type of constituting elements, and also on the assumption that no IM compound or amorphous phase is formed in HEAs [68,69]. Furthermore, the VEC rule is reported to be mainly applicable for HEAs that constitute primarily 3d or 4d transitional metals and is reliable mainly for the equiatomic or semi-equiatomic HEAs [12]. These limitations have impacted the accurate prediction of the crystal structure formation in HEAs [34,66].

According to several experiments, the SS formation in HEAs is favourable when the ΔH_{mix} is between 5 kJ/mol and -15 kJ/mol and $\delta \leq 6.6\%$, whereas amorphization and IM compound formation can occur outside this region [70]. Similarly, $\triangle \chi \leq 0.175$, $\Omega \geq 1.1$, and 11 J/K-mol $\leq$ $\Delta S_{mix} \leq$ 19.5 J/K-mol effectively benefit the formation of SS instead of IM compound [33,34]. Yang et al. [34] observed that the phase formation rules erroneously predicted the SS in low-density HEAs consisting of Al, Mg, and Li as their microstructures contained several IM compounds. Therefore, they estimated that the rules for the SS formation in such alloys might be more conservative, such as $\Omega \geq 10$, $\delta < 4.5\%$, and -1 kJ/mol $\leq \Delta H_{mix} \leq$ 5 kJ/mol. Moreover, refractory HEAs, such as MoNbTaW, HfNbTaTiZr, and MoNbTaWV, exhibited a single BCC phase in a narrow range of $\Delta H_{mix} >$ -7.5 kJ/mol and $\delta <$ 4.5% [71]. Also, on the contrary, $Al_{0.5}TiZrPdCuNi$ alloy exhibited a single BCC phase without IM compounds despite having a ΔH_{mix} of -46.7 kJ/mol and δ of 8.8%, which are outside the traditional SS region [71],[72]. Similarly, AlTiVCr showed an ordered B2 phase and $Co_{0.5}Cr_{0.5}Fe_{0.5}NiAlMnV_{0.5}$ possessed a single BCC phase even with ΔH_{mix} values of -16.75 kJ/mol and -15.96 kJ/mol, respectively [66,71]. These collections of many separate studies suggest that the conventional crystal structure and phase stability rules can also be alloy-dependent.

In addition, processing methods from the liquid state (e.g., arc melting), solid state (e.g., mechanical alloying), gas state (e.g., sputtering technique), and electrochemical process (e.g., electrodeposition), also influence the evolved crystal structure and final phase formation in HEA system [38]. For instance, CoCrCuFeNi alloy processed by arc melting formed an FCC single-phase SS following the structure predicted by the empirical rules, whereas under spark plasma sintering processing conditions, this alloy showed the evolution of sigma phases [73]. Similarly, $Al_{0.3}$CoCrFeNi HEA processed by vacuum induction melting and magnetron sputtering shows single (FCC) [74] and dual (FCC and BCC) [75] phases, respectively. The same contrasting phase evolution was observed for CoCrFeMnNi HEA developed by arc melting (FCC) [76] and mechanical alloying (MA) plus spark plasma sintering (FCC and Cr-carbide) [77], respectively. All these studies suggest that the evolution of phases can be process-dependent, and the empirical rules can face breakdown depending on different processing routes.

To adequately assess the empirical rules and their possible breakdown, a systematic study that isolates the effect of processing pathway is necessary. In this study, an existing equiatomic AlCoCrFe and five novel semi-equiatomic AlTiCuZn-based quaternary HEAs were developed by a single processing method—mechanical alloying (MA)—to revisit and determine the efficacy of the empirical rules, and how the composition of HEA might influence their accuracy. MA is a solid-state powder processing technique that involves welding, fracturing, and rewelding of elemental powder mixtures by continuously colliding milling balls in a vial, leading to nanograin formation while the powder particles remain at the microscale [30,31]. The choice of MA is because it prevents the evaporation of low-melting elements that would occur during traditional casting methods [6,32], especially for HEAs whose constituent elements' melting points vary significantly. AlTiCuZn-based HEAs are selected for this study because they are newly-identified

low density-HEAs, and there exists a wide range of the HEA compositions that initially fulfilled all the classical phase stability criteria. In the end, this work establishes modified sets of criteria for phase stability for AlTiCuZn-based HEAs, which are later verified by fabricating two completely new non-equiatomic AlTiCuZn-based HEAs.

2.2   Materials and Methods

To develop AlCoCrFe and AlTiCuZn-based HEAs, Al, Co, Cr, and Fe powders were mixed in equiatomic ratio for AlCoCrFe, while Al, Ti, Cu, and Zn powders were mixed in the appropriate atomic ratios to obtain $Al_{0.57}TiCuZn$, $AlTi_{0.45}CuZn$, $Al_{0.45}TiCuZn$, $AlTiCu_{1.76}Zn$, and $AlTiCu_2Zn$ HEAs. The morphology and details of these as-received powders are given in **Figure 2.1** and **Table 2.1**, respectively. Milling of these powders was conducted in a planetary ball mill (PBM-04, MicroNano Tools) in an argon gas inert atmosphere with a ball-to-powder ratio of 10:1. Stainless steel balls (50 and 8 balls that are 6 mm and 10 mm in diameters, respectively) and zirconia vacuum grinding jars with stainless steel jackets were used. To prevent excessive cold-welding and to increase powder recovery, a process control agent (PCA) is usually used during the milling process [78]. Both 1 weight percent (wt.%) and 1.5 wt.% of ethanol PCA were used to observe whether the PCA concentration affects the phase stability rules. Initially, the starting element powders were mixed at 100 rpm for 1 h to ascertain their uniform mixing. Then the actual milling was performed at 350 rpm up to 40 h with samples being taken out at 10 h intervals for characterizations.
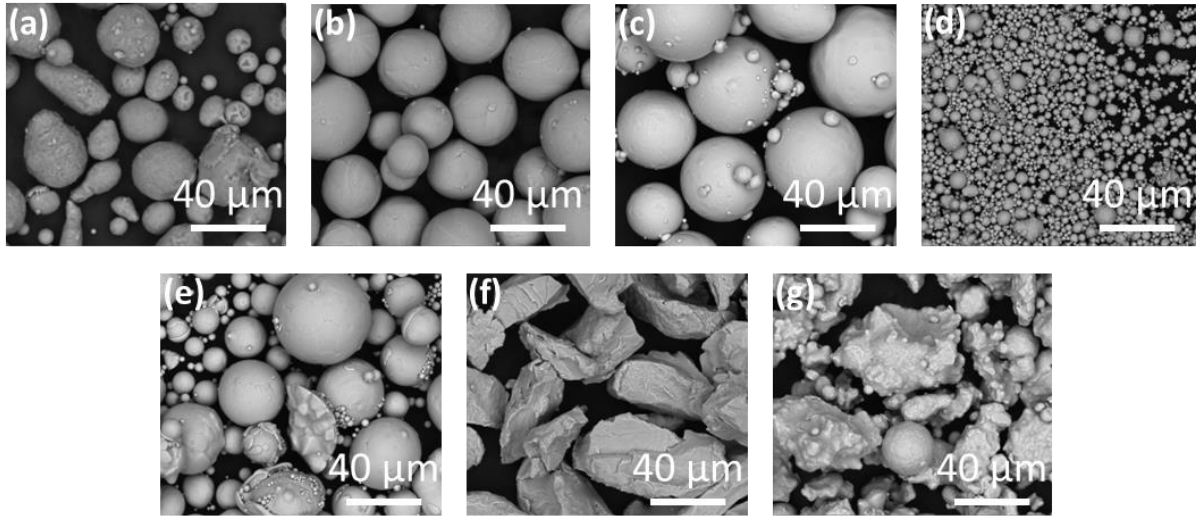
Figure 2.1: SEM images of the initial metal powders- **(a)** Al, **(b)** Ti, **(c)** Cu, **(d)** Zn, **(e)** Co, **(f)** Cr, and **(g)** Fe.

Table 2.1: Details of the as-received metal powders used in the experiment.

Element	Source	Production methods	Average Particle Size (micron)	Purity (%)
Al	Solvus Global	Gas Atomization	29.07 ± 0.54	99.7
Ti	Solvus Global	Gas Atomization	19.15 ± 3.03	>99.5
Cu	Solvus Global	Gas Atomization	16.13 ± 2.96	99.99
Zn	Solvus Global	Distillation	3.09 ± 0.31	>99.9
Co	GoodFellow	Gas Atomization	28.63 ± 0.86	99.8
Cr	GoodFellow	Aluminothermic Reaction	41.52 ± 1.08	>99.0
Fe	GoodFellow	*	29.52 ± 1.08	>99.0

*Powder production method was not provided by GoodFellow at the time of writing.

The crystal structure, phases, and grain size of the as-milled powders were analysed by X-ray diffraction (XRD) technique using Bruker D8 Advance (ECO) with Cu K_α ($\lambda = 0.15418$ nm) source and $10°$-$90°$ scanning angle range with $2.3°$/min rate of scanning. The crystal structure and phases of the samples were obtained from the XRD patterns using the DIFFRAC.EVA (Bruker) software. The morphology, composition, and elemental distribution of the powders were

investigated by scanning electron microscopy (SEM) using Bruker Nano GmbH Berlin, Germany with a XFlash 5030 energy dispersive spectroscopy (EDS) detector. The SEM was operated at 20 keV. Furthermore, transmission electron microscopic (TEM) observations of AlCoCrFe HEA were performed using Tecnai F20 at 160 kV. For the TEM sample preparation, the alloy powder was processed in a sonicator for 10 min with ethanol suspension. Subsequently, 3 µL of the suspension was dropped on the 400 mesh copper grids of 3 mm diameter and then dried in the air for 15 min. Open-source ImageJ software was used to calculate the particle sizes from the SEM images and grain sizes from the TEM images. While using ImageJ, the image calibration was initially conducted to correlate the image dimensions in pixel to physical dimensions [79]. The reported particle and grain sizes are average values of several measurements.

2.3   Result and Discussion

2.3.1   Alloy selection using phase stability rules

Using the classical empirical equations for theoretical density calculation (Eqn. 2.1) and the prediction parameters in Eqns. 2.2-2.7 for crystal structure and phase prediction in HEAs [34], we developed ΔH_{mix} - δ, ΔS_{mix} - δ, Ω - δ, $\triangle \chi$ - δ, and VEC - δ plots for AlCoCrFe and AlTiCuZn-based equiatomic and semi-equiatomic HEAs, as shown in **Figure 2.2**; the theoretical density, ρ_{theor} is given by the following equation:

$$\rho_{theor} = \frac{\sum_{i=1}^{n} c_i A_i}{\sum_{i=1}^{n} c_i A_i / \rho_i} \dots \dots \dots (2.1)$$

where, c_i, A_i, and ρ_i are the atom fraction, atomic weight, and density of each i-th respective constituent element, respectively, and n is the total number of elements.

Atomic size difference, δ is given by the following equation:

26

$$\delta = \sqrt{\sum_{i=1}^{n} c_i (1 - r_i/\bar{r})^2} \ \dots \dots \dots (2.2)$$

Enthalpy of mixing, $\triangle H_{mix}$ is given by the following equation:

$$\triangle H_{mix} = \sum_{i=1, i \neq j}^{n} \Omega_{ij} c_i c_j \ \dots \dots \dots (2.3)$$
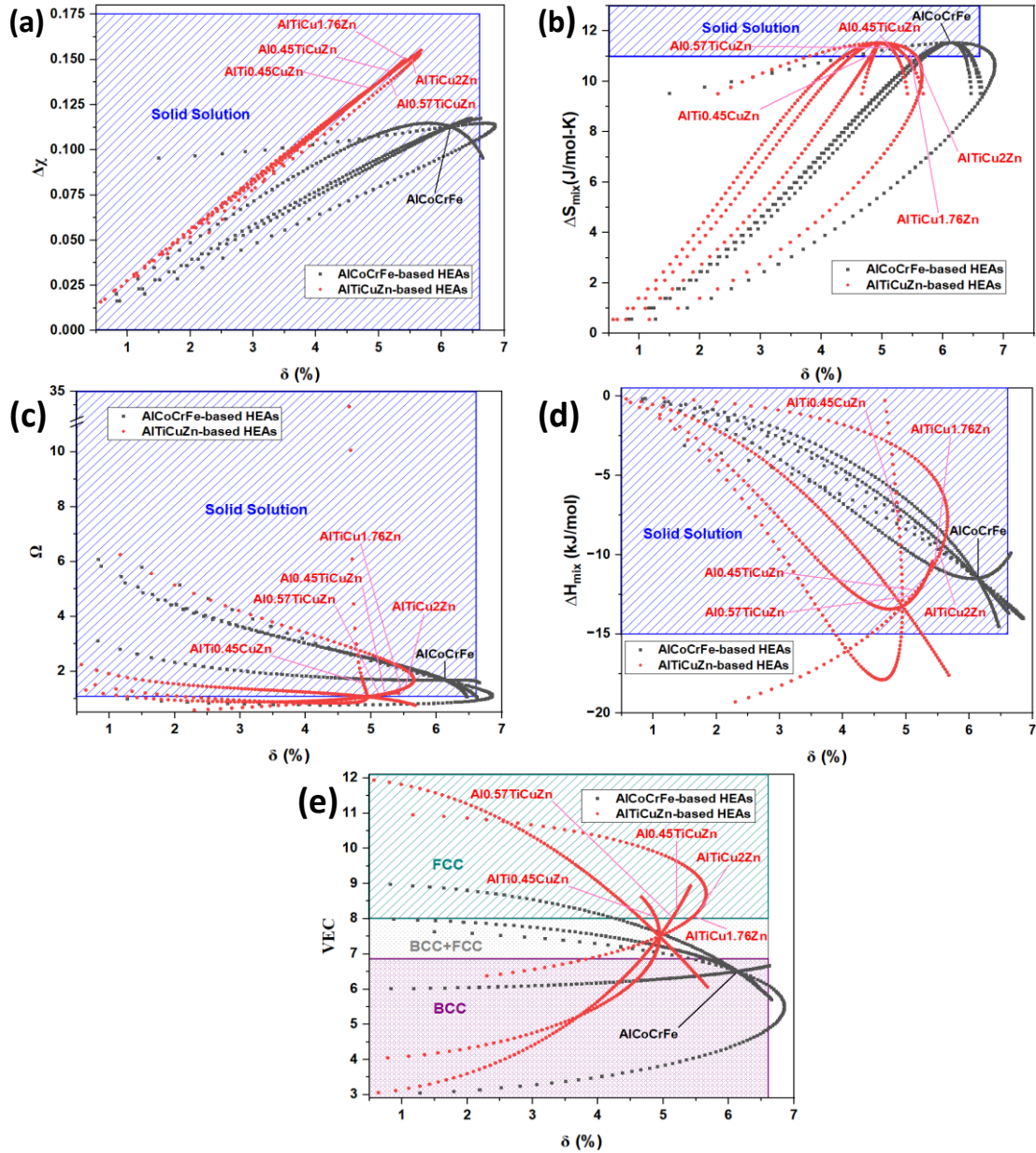
Figure 2.2: (a) $\Delta\chi$-δ, **(b)** ΔS_{mix}-δ, **(c)** Ω-δ, **(d)** ΔH_{mix}-δ, and **(e)** *VEC*-δ plots for AlCoCrFe and AlTiCuZn-based HEAs. Shaded regions cover a range of empirical model values for predicting (a-d) solid-solution and (e) phase formation.

27

Entropy of mixing, $\triangle S_{mix}$ is given by the following equation:

$$\triangle S_{mix} = -R \sum_{i=1}^{n} c_i lnc_i \ \dots \dots \dots (2.4)$$

Ratio of entropy to enthalpy values, Ω is given by the following equation:

$$\Omega = \frac{T_m \triangle S_{mix}}{|\triangle H_{mix}|} \ \dots \dots \dots (2.5a)$$

$$T_m = \sum_{i=1}^{n} c_i (T_m)_i \ \dots \dots \dots (2.5b)$$

Pauling electronegativity difference, $\triangle \chi$ is given by the following equation:

$$\triangle \chi = \sqrt{\sum_{i=1}^{n} c_i (\chi_i - \bar{\chi})^2} \ \dots \dots \dots (2.6)$$

Valence electron concentration, VEC is given by the following equation:

$$VEC = \sum_{i=1}^{n} c_i (VEC)_i \ \dots \dots \dots (2.7)$$

where, c_i or c_j represents the atomic percentage (at.%) of the i-th or j-th component, $\bar{r}$ is the average atomic radius, r_i denotes the atomic radius, $\Omega_{ij} (= 4 \triangle H_{AB}^{mix})$ is the regular solution interaction parameter between the i-th and j-th elements, $\triangle H_{AB}^{mix}$ represents the enthalpy of mixing of binary liquid alloys, T_m is the melting point of n-elements alloy, $(T_m)_i$ denotes the melting point of the i-th component of alloy, $\bar{\chi} = \sum_{i=1}^{n} c_i \chi_i$, χ_i is the Pauling electronegativity for the i-th component, and $(VEC)_i$ represents the VEC of the i-th element. In addition, the required data for the density and empirical rule calculations are listed in **Tables 2.2** and **2.3**.

To improve the confidence of single-phase SS HEA prediction, semi-equiatomic quaternary alloys that simultaneously fulfil all empirical rules as indicated within the rectangular marked regions in

28

Figure 2.2 were selected—Al$_{0.57}$TiCuZn, AlTi$_{0.45}$CuZn, Al$_{0.45}$TiCuZn, AlTiCu$_{1.76}$Zn, and AlTiCu$_2$Zn HEAs. As a form of "benchmarking" to validate the correctness of our MA process, an equiatomic AlCoCrFe HEA that also fulfils all the empirical rules were selected; this is a known HEA with single-phase BCC structure [80]. The theoretical density and phase prediction parameters calculated for the selected HEAs along with the SS ranges considered are presented in **Table 2.4**—it shows all selected alloys are predicted to be in SS, while the AlCoCrFe and AlTiCuZn-based HEAs are predicted to constitute single-phase BCC and FCC structure,

Table 2.2: Atomic radius (r), standard atomic weight (A), crystal structure, Pauling electronegativity (χ), valence electron concentration (VEC), density (ρ), and melting temperature (T_m) of the constituent elements of the HEAs used in the present work.

Elements	r (Å) [34,67]	A (g/mol) [34,67]	Crystal Structure [34,67]	χ [34,81]	VEC [34,81]	ρ (g/cm^3) [34,67]	T_m (K) [34,67]
Al	1.43	26.98	FCC	1.61	3	2.7	933.5
Co	1.251	58.9332	HCP	1.88	9	8.9	1768
Cr	1.249	51.996	BCC	1.66	6	7.19	2180
Fe	1.241	55.874	BCC	1.83	8	7.874	1811
Ti	1.462	47.867	HCP	1.54	4	4.507	1941
Cu	1.28	63.55	FCC	1.9	11	8.93	1358
Zn	1.39	65.39	HCP	1.65	12	7.13	692.7

Table 2.3: The enthalpy data used in the present work for the empirical rule calculations.

Binary Alloy	$\triangle H_{mix}$ (kJ/mol) [8]	Binary Alloy	$\triangle H_{mix}$ (kJ/mol) [8]
Al-Co	-19	Al-Ti	-30
Al-Cr	-10	Al-Zn	1
Al-Fe	-11	Al-Cu	-1
Co-Cr	-4	Ti-Zn	-15
Co-Fe	-1	Ti-Cu	-9
Cr-Fe	-1	Zn-Cu	1

respectively. It should be noted that AlCoCrFe and AlTiCuZn-based HEAs are 3d transition metals-dominated HEAs, hence, accurate prediction of crystal structure and phases is somewhat expected [12],[68].

Table 2.4: Selected quaternary alloys with predicted single phase using the following empirical rules: δ ($\delta \leq 6.6\%$), ΔH_{mix} (-15 kJ/mol $\leq \Delta H_{mix} \leq$ 5 kJ/mol), ΔS_{mix} (11 J/K-mol $\leq \Delta S_{mix} \leq$ 19.5 J/K-mol), Ω ($\Omega \geq 1.1$), $\triangle \chi$ ($\triangle \chi \leq 0.175$), and *VEC* (*VEC* < 6.87: BCC; 6.87 < *VEC* < 8: BCC+FCC; *VEC* >8: FCC).

Alloy	δ (%)	ΔH_{mix} (kJ/mol)	ΔS_{mix} (J/K-mol)	$\triangle \chi$	Ω	*VEC*	Theoretical Density (g/cm³)
AlCoCrFe	6.14	-11.50	11.53	0.113	1.68	6.50 (BCC)	6.26
Al$_{0.45}$TiCuZn	5.20	-12.26	11.16	0.143	1.16	8.22 (FCC)	6.02
Al$_{0.57}$TiCuZn	5.14	-12.59	11.33	0.142	1.14	8.04 (FCC)	5.89
AlTi$_{0.45}$CuZn	4.88	-7.81	11.16	0.134	1.60	8.06 (FCC)	5.71
AlTiCu$_{1.76}$Zn	5.45	-10.56	11.23	0.149	1.33	8.06 (FCC)	5.96
AlTiCu$_2$Zn	5.53	-9.92	11.08	0.151	1.40	8.20 (FCC)	6.07

2.3.2 Phase evolution and evaluation of AlCoCrFe HEA for benchmarking

The XRD plot for AlCoCrFe HEA with varying milling time and 1 wt.% ethanol as the PCA is shown in **Figure 2.3**. At 0 h of milling, peaks corresponding to FCC-Al, HCP-Co, BCC-Cr, and BCC-Fe elements can be observed. As the milling time increases, that is, the occurrence of repeated cold-welding and collision of the particles, lattice diffusion sets on [82]; this manifested as the disappearance of certain peaks (Al and Co) until dominant all-BCC peaks, (101), (200), and (211), evolve at 20 h of milling at 2θ values, 44.4°, 64.7°, and 81.5°, respectively. Prior work on mechanically-alloyed binary systems reported that the earlier peak disappearance in an XRD pattern is a function of atomic number (Z)—peaks for lower Z elements disappear first because of lower atomic scattering factor, while those of higher Z persist; i.e., Al ($Z = 13$) peaks disappeared while Mo ($Z = 42$) peaks persisted in an Al-Mo system, similarly, Ni ($Z = 28$) peaks disappeared while Ru ($Z = 44$) peaks persisted in a Ni-Ru system [83]. For the equiatomic HEA under

30

consideration, Al ($Z = 13$) and Cr ($Z = 24$) are the elements with the lowest atomic number, and their respective peaks should disappear based on the "atomic number theory". Hence, the disappearance of Al ($Z = 13$) and Co ($Z = 27$) peaks instead, in **Figure 2.3**, reignite the question of how the characteristic of constituting elements in an alloy might inform the order of peak disappearance in a diffraction pattern.
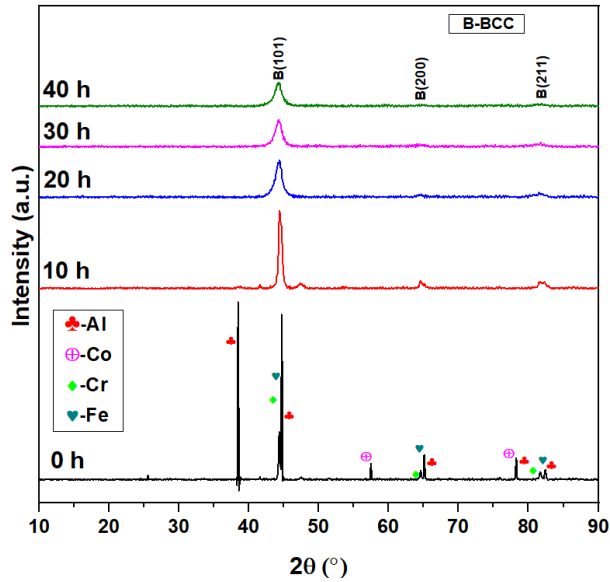
Figure 2.3: XRD plot for AlCoCrFe HEA processed with 1 wt.% of ethanol as the PCA, for varying milling times.

Since alloy formation during milling is driven by a diffusion process, the rate of diffusion varies for each element, and the peak disappearance can be explained by the diffusion coefficient, D [84];

$$D = D^0 \exp\left(\frac{-Q}{RT}\right) \dots \dots \dots (2.8)$$

where, D^0 is the pre-exponential factor, Q is the activation energy for diffusion and it is proportional to T_m (melting point), and T is the absolute temperature. This expression implies that the element with high T_m has a lower diffusion rate due to stronger interatomic bonds than the element with low T_m during MA, i.e., $T_m^{Cr} > T_m^{Fe} > T_m^{Co} > T_m^{Al}$ or $D_{Cr} < D_{Fe} < D_{Co} < D_{Al}$. The

31

lower melting point (or higher diffusivities) of Al and Co could therefore suggest their more rapid diffusion during milling, and in turn, their decreased peak intensities at a lower milling time [85]. This culminates in the earlier disappearance of Al and Co peaks as early as 10 h milling time in **Figure 2.3**, and it further provides evidence for the dissolution of the "disappearing" elements—Al and Co—in the "persistent" ones—Fe and Cr [83]. It is therefore concluded that the disappearance or persistence of peaks in an XRD pattern for mechanically-alloyed material is a function of the *melting point* of the constituting elements rather than the atomic number. We note that for the studied binary alloys in Refs. [83,86,87], Z and T_m of the constituting elements follow the same trend, Al ($T_m = 933$ K) - Mo ($T_m = 2890$ K), Ni ($T_m = 1726$ K) - Ru ($T_m = 2523$ K), and Al-Ni, so that the "atomic number theory" for peak disappearance can be erroneously suggested at the expense of the "melting point theory". The conclusion that early dissolution of low melting point elements occurs at lower milling time is consistent with prior observations in TiZrNbTa, AlCrCuFeNi, MoNbTaTiV, and CuNiCoZnAl alloy systems [82,88–90].
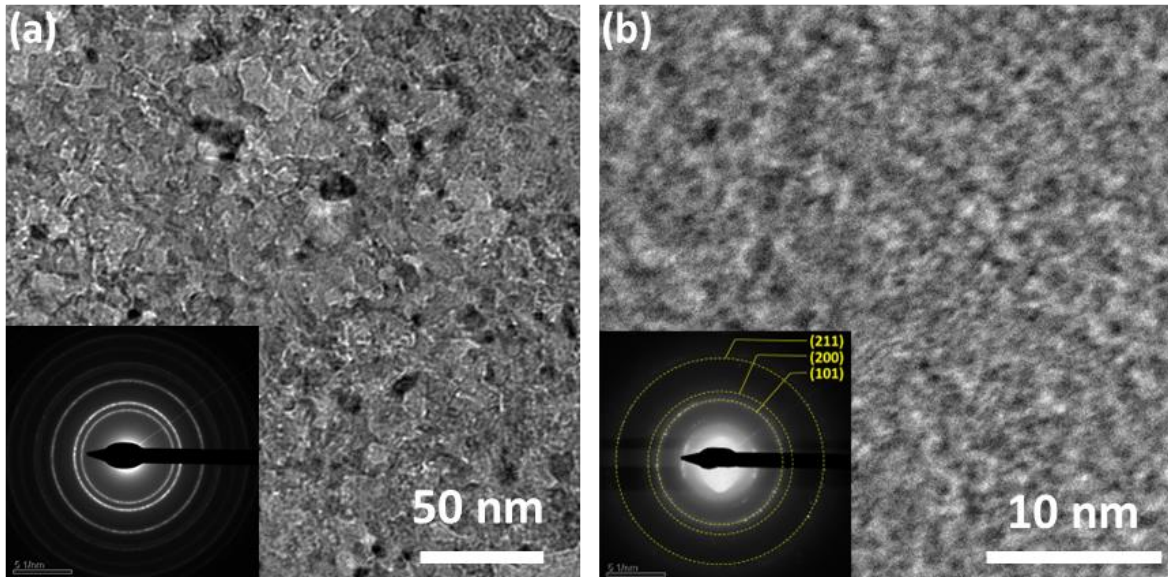
Figure 2.4: TEM images and associated SAED patterns (inset) for AlCoCrFe HEA at **(a)** 10 h and **(b)** extended milling time.

Figure 2.3 also shows apparent intensity reduction and broadening of the peaks as the milling time increases; this suggests refinement of grains to the nanoscale due to the repetition of plastic deformation and complete dissolution of atoms during milling [85]. The evolution of nanograins in as-milled AlCoCrFe HEA is confirmed in the TEM micrographs in **Figure 2.4**—~9 and 6 nm average grain sizes for 10 h and extended milling time, respectively. In agreement with the XRD pattern in **Figure 2.3**, the selected-area electron diffraction (SAED) pattern in **Figure 2.4(a)** also confirms the absence of SS at 10 h due to the presence of multiple concentric diffraction rings. Meanwhile, major rings with slight halo corresponding to single-phase BCC (101), (200), and (201) planes are observed at extended milling time in **Figure 2.4(b)**.
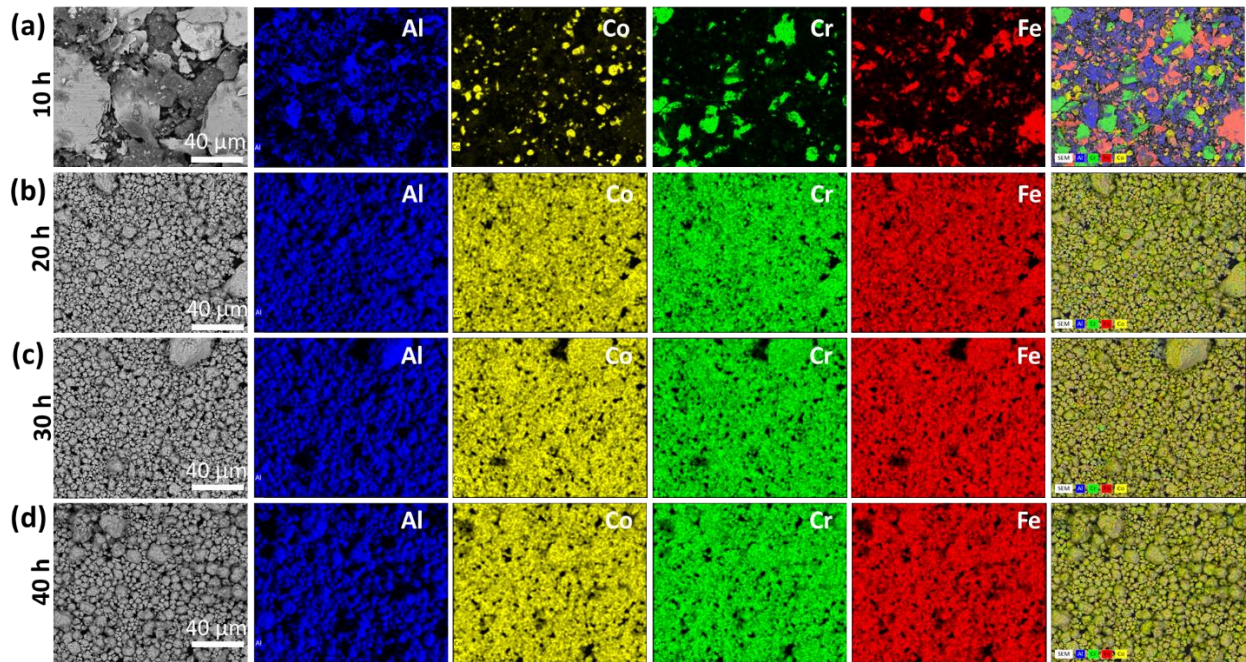
Figure 2.5: SEM images and EDS maps for AlCoCrFe HEA after **(a)** 10 h, **(b)** 20 h, **(c)** 30 h, and **(d)** 40 h of milling time and 1 wt.% ethanol as the PCA.

Figure 2.5 shows the SEM images and EDS maps for AlCoCrFe HEA corresponding to the milling hours. In agreement with the XRD pattern, uniformly mixed Al-Co-Cr-Fe suggest the onset of SS for AlCoCrFe HEA at 20 h of milling and above. Based on the EDS point analysis, the at.% of Al,

Co, Cr, and Fe elements after 40 h of milling are 22.4 ± 4, 26.4 ± 2, 25.1 ± 2, and 26.1 ± 2 %, respectively. This confirms the successful fabrication of SS equiatomic AlCoCrFe HEA with BCC structure as rightly predicted by structure and phase prediction rules in **Figure 2.2**, and also previously confirmed in previous works [80,91]. In what follows, we characterize the new AlTiCuZn-based HEAs that simultaneously fulfil all empirical rules in **Figure 2.2**. Millings were conducted using a new set of jars and balls to avoid possible contaminations from other non-constituting elements.

2.3.3 Evaluation of AlTiCuZn-based HEAs

2.3.3.1 *Phase evolution and its correlation with the predictions of the phase stability criteria*

The XRD patterns for AlTi$_{0.45}$CuZn and Al$_{0.57}$TiCuZn HEAs milled with 1 wt.% ethanol up to 40 h milling time are shown in **Figures 2.6(a)** and **2.6(b)**, respectively. Accordingly, peaks relating to FCC-Al, HCP-Ti, FCC-Cu, and HCP-Zn elements were observed prior to milling (0 h). As established earlier for equiatomic AlCoCrFe HEA, peaks for lower melting point elements—Al and Zn—disappeared at a lower milling time than those of high melting point—Cu and Ti—in **Figures 2.6(a)** and **2.6(b)**. At 20 h of milling and above, SS was obtained for AlTi$_{0.45}$CuZn HEA following the phase stability rules (**Figure 2.6(a)**), but with FCC and HCP dual phases instead of the single-phase FCC structure predicted from the VEC rule. The formation of HEAs with FCC and HCP dual phases is rare, however, few have been reported including Fe$_{50}$Mn$_{30}$Co$_{10}$Cr$_{10}$ [47,65], Co$_{20}$Cr$_{20}$Fe$_{34}$Mn$_{20}$Ni$_{6}$ [92], Fe$_{39}$Mn$_{20}$Co$_{20}$Cr$_{15}$Si$_{5}$Al$_{1}$ [93], and Fe$_{38.5}$Mn$_{20}$Co$_{20}$Cr$_{15}$Si$_{5}$Cu$_{1.5}$ [93] HEAs. Li et al. [47,65] reported a transition from FCC single phase to FCC + HCP dual phase for Fe$_{80-x}$Mn$_{x}$Co$_{10}$Cr$_{10}$ HEA with the declination of Mn content from 45 at.% to 30 at.%. Compared to many FCC single-phase HEAs, this fabricated FCC + HCP dual-phase HEA with 28% HCP phase showed superior ultimate tensile strength and yield strength [94]. Following the same

34

process, Li et al. [92] synthesized $Co_{20}Cr_{20}Fe_{40-x}Mn_{20}Ni_x$ FCC + HCP dual-phase HEAs (where, x varied from 0 at.% to 20 at.%) having between 6% and 69% HCP phase. Greater strain-hardening ability and tensile strength were shown by the dual phase HEA with 69% HCP phase; hence, the development of FCC + HCP dual phase HEA is a design strategy for improving the mechanical properties of HEAs [94].

Also, as the milling progressed, the intensity reduction and broadening of the peaks were obvious for $AlTi_{0.45}CuZn$ HEA, indicating the reduction of grain sizes. On the contrary, $Al_{0.57}TiCuZn$ shows a complete breakdown of the empirical rules: evolution of dual phases—FCC and HCP, and IM compound phases (**Figure 2.6(b)**). A plot of all AlTiCuZn-based HEAs—$Al_{0.57}TiCuZn$, $AlTi_{0.45}CuZn$, $Al_{0.45}TiCuZn$, $AlTiCu_{1.76}Zn$, and $AlTiCu_2Zn$—milled for 40 h with 1 wt.% ethanol is shown in **Figure 2.6(c)**. Despite the prediction of single-phase FCC SS for all AlTiCuZn-based HEAs, only $AlTi_{0.45}CuZn$ shows promising dual FCC + HCP phase SS without IM compound phases.
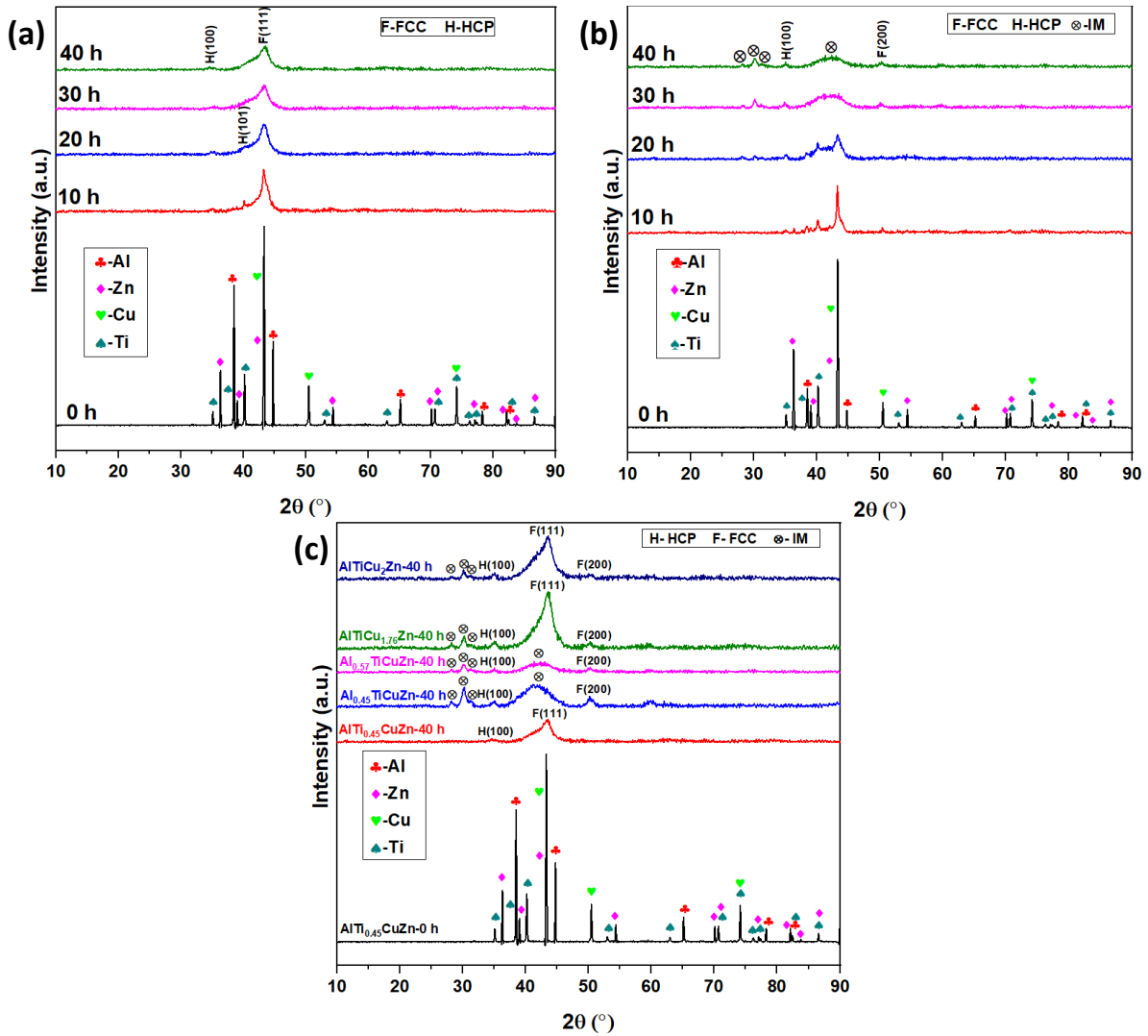
Figure 2.6: XRD plots for **(a)** $AlTi_{0.45}CuZn$ and **(b)** $Al_{0.57}TiCuZn$ HEAs with varying milling time, **(c)** AlTiCuZn-based five semi-equiatomic HEAs at 40 h of milling. 1 wt% ethanol was used as the PCA in every case.

There are certainly previous works that report the influence of PCAs on IM compound and unwanted phase formation [30,95]. To this end, we ball-milled new $AlTi_{0.45}CuZn$ and $Al_{0.57}TiCuZn$ HEAs but with 1.5 wt.% ethanol as the PCA. The corresponding XRD patterns for $AlTi_{0.45}CuZn$ and $Al_{0.57}TiCuZn$ HEAs as a function of milling time are shown in **Figure 2.7**. The PCA concentration affects the onset of peak dissolution because higher PCA concentration during MA works as a lubricant and a "barrier" between particles and balls, and also between particles so

36

that the rate of cold welding and fracture processes is retarded [82]. However, the final structure

for both alloys at 40 h of milling remained unaltered; therefore, the SS or IM compound formation

is unaffected by the PCA concentration.
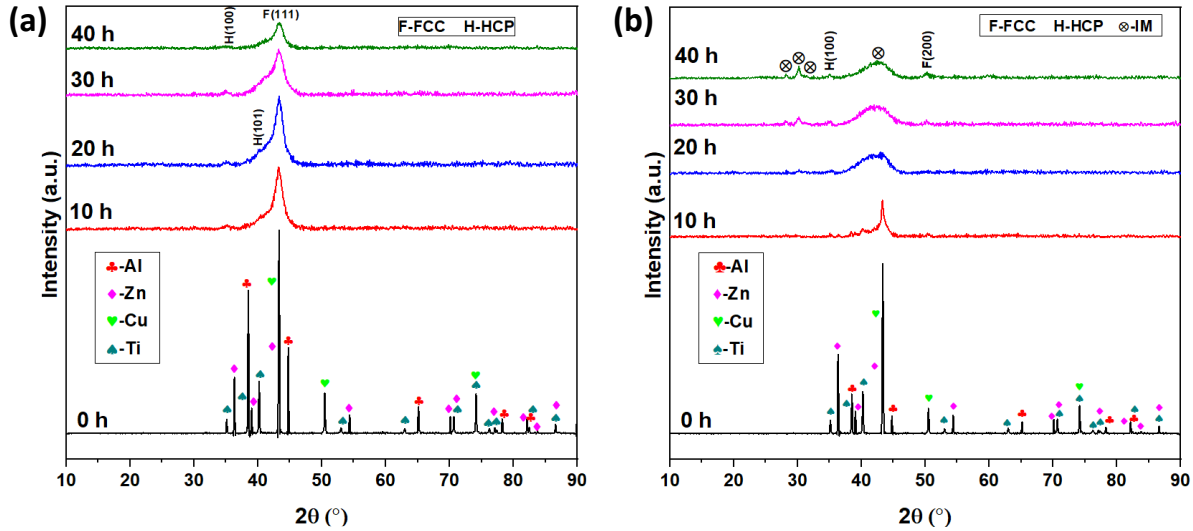
Figure 2.7: XRD plots for **(a)** AlTi$_{0.45}$CuZn and **(b)** Al$_{0.57}$TiCuZn HEAs with varying milling time and 1.5 wt.% ethanol as the PCA.

Another possible cause of departure from the phases predicted by the empirical model for

AlTiCuZn-based HEAs can be the inaccurate determination of T_m in Eqn. 2.5. To validate this, an

alternate approach to estimating T_m for HEAs as proposed by Qi et al. [96] was used; T_m calculation

from the liquidus temperatures in binary phase diagrams was carried out using the following

equation:

$$T_m = \frac{\Sigma_{i \neq j} T_{i-j} \times c_i \times c_j}{\Sigma_{i \neq j} c_i \times c_j} \ldots \ldots \ldots (2.9)$$

where, c_i and c_j are the atomic percentages of the i-th and j-th element. The binary liquidus

temperatures, T_{i-j}, can be found at the composition at which the relative ratio of i-th and j-th

element is c_i: c_j for the binary pair i-j [96]. The T_{i-j} values for Al-Ti, Al-Zn, Al-Cu, Ti-Zn, Ti-Cu,

and Zn-Cu binary alloys were determined to be 1773, 843, 853, 1500, 1255, and 1143 K,

respectively, from their corresponding phase diagrams [97–99]. It can be seen in **Table 2.5** that

the estimated T_m values from both methods are very close. Similarly, the modified T_m values for

AlTiCuZn-based HEAs were used to calculate their corresponding modified Ω values as shown in

Table 2.5. It is observed that this alternative approach does not significantly affect the values of

Ω, and the SS requirement—$\Omega \geq 1.1$ is still maintained for all HEAs. Hence, the previous

approach to estimating T_m (Eqn. 5b) is not responsible for the inaccuracy of phase stability rules.

Table 2.5: Comparison between the T_m *and* Ω values when T_m is calculated using different methods.

Alloy	T_m based on Eqn. 5(b)	Previous Ω	$\Sigma(T_{i-j} \times c_i \times c_j)$	$\Sigma(c_i \times c_j)$	T_m based on Eqn. 9	Modified Ω
$Al_{0.45}TiCuZn$	1278.95	1.16	4586031	3654	1255.07	1.14
$Al_{0.57}TiCuZn$	1267.04	1.14	4610144	3696	1247.33	1.12
$AlTi_{0.45}CuZn$	1117.75	1.60	4094655	3654	1120.60	1.60
$AlTiCu_{1.76}Zn$	1251.57	1.33	4341183	3654	1188.06	1.26
$AlTiCu_2Zn$	1256.64	1.40	4247200	3600	1179.78	1.32

Sample SEM images with EDS maps for $AlTi_{0.45}CuZn$ and $Al_{0.57}TiCuZn$ HEAs as a function of

milling time are shown in **Figure 2.8** to confirm the complete formation of the alloy after the

milling ended. At 20 h of milling, the constituents of $AlTi_{0.45}CuZn$ (**Figure 2.8(a)**) and

$Al_{0.57}TiCuZn$ (**Figure 2.8(b)**) were mostly mixed, but a few unmixed Ti particles were present.

The EDS maps confirm the earlier XRD results on the dissolution of peaks: higher melting point

elements possess stronger bonds between atoms so that Ti exhibits a lower alloying rate and longer

milling time to uniformly dissolve compared to other elements [84]. The lower dissolution rate of

Ti is more prominent in $Al_{0.57}TiCuZn$ due to its higher Ti content (EDS point analysis: Al, Cu, Zn,

and Ti are 13.4 ± 4, 27.1 ± 2, 26.6 ± 2, and 32.9 ± 2 at.%, respectively) compared to that of

$AlTi_{0.45}CuZn$ HEA (EDS point analysis: Al, Cu, Zn, and Ti are 26.2 ± 4, 28.9 ± 2, 29.5 ± 2, and
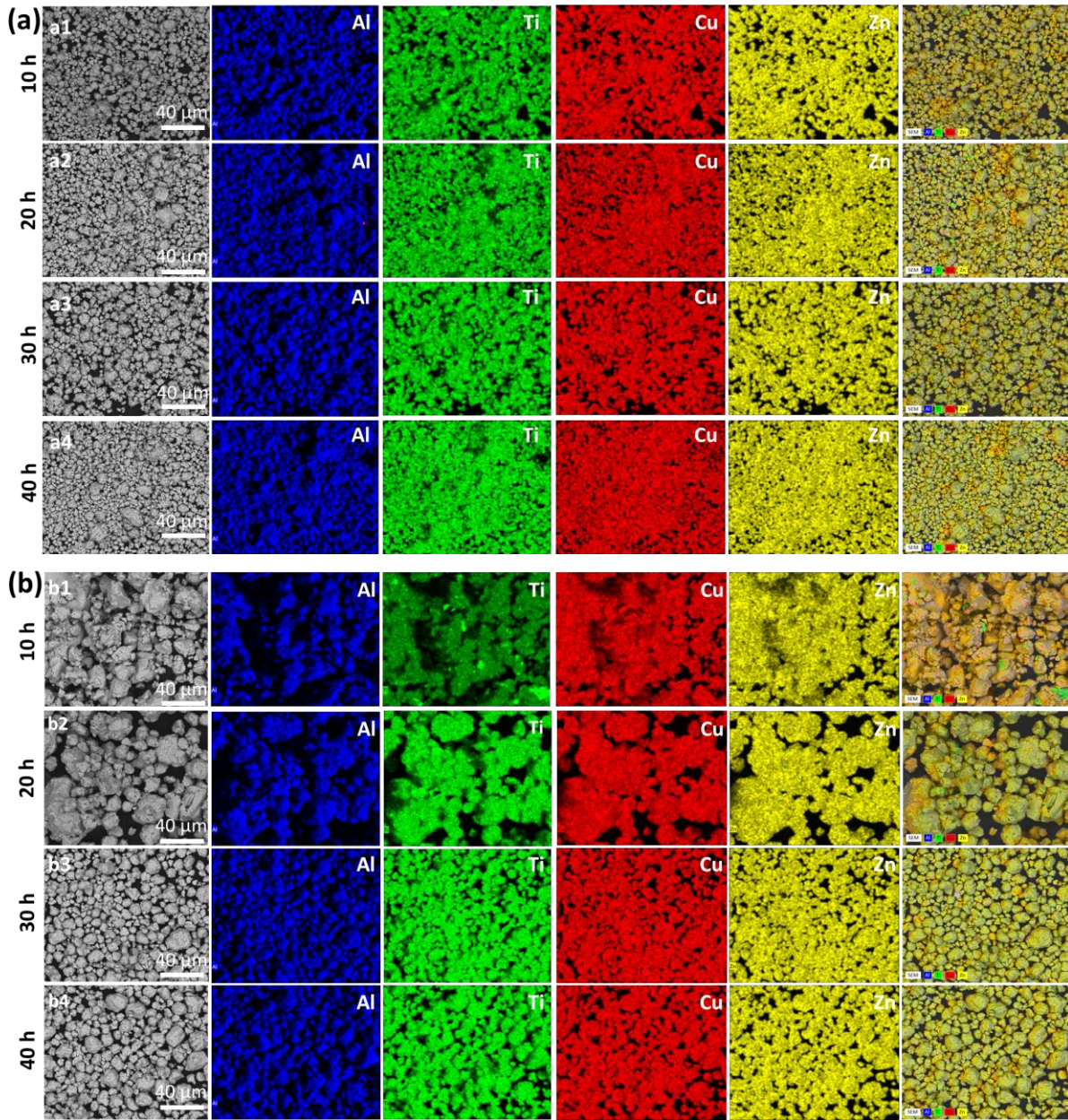
Figure 2.8: SEM images and EDS maps for **(a)** $AlTi_{0.45}CuZn$ and **(b)** $Al_{0.57}TiCuZn$ HEAs with varying milling time and 1 wt.% ethanol as the PCA.

15.4 ± 2 at.%, respectively). At 30 h of milling and above, each constituent of both alloys was uniformly mixed which alloy formation in agreement with the XRD results. At 40 h of milling, the particles of both HEAs are nearly spherical; this is because both cold-welding and fracture processes are balanced at higher milling times [82]. Also, with the progression of milling, the average particle sizes for $AlTi_{0.45}CuZn$ and $Al_{0.57}TiCuZn$ HEAs initially increased up to 7.5 µm

(at 30 h) and 16.3 μm (at 20 h), respectively, and then declined to 6.9 μm and 8.7 μm, respectively, at 40 h of milling. The initial increase in particle size with milling time can be attributed to cold-welding agglomeration, while the reduction in particle size for further milling can be due to fragmentation [85]. In agreement with the XRD observations, the TEM micrographs and the diffraction pattern in **Figure 2.9** confirms the dual phase FCC + HCP SS formation in $AlTi_{0.45}CuZn$ HEA with an average grain size of 8 nm.
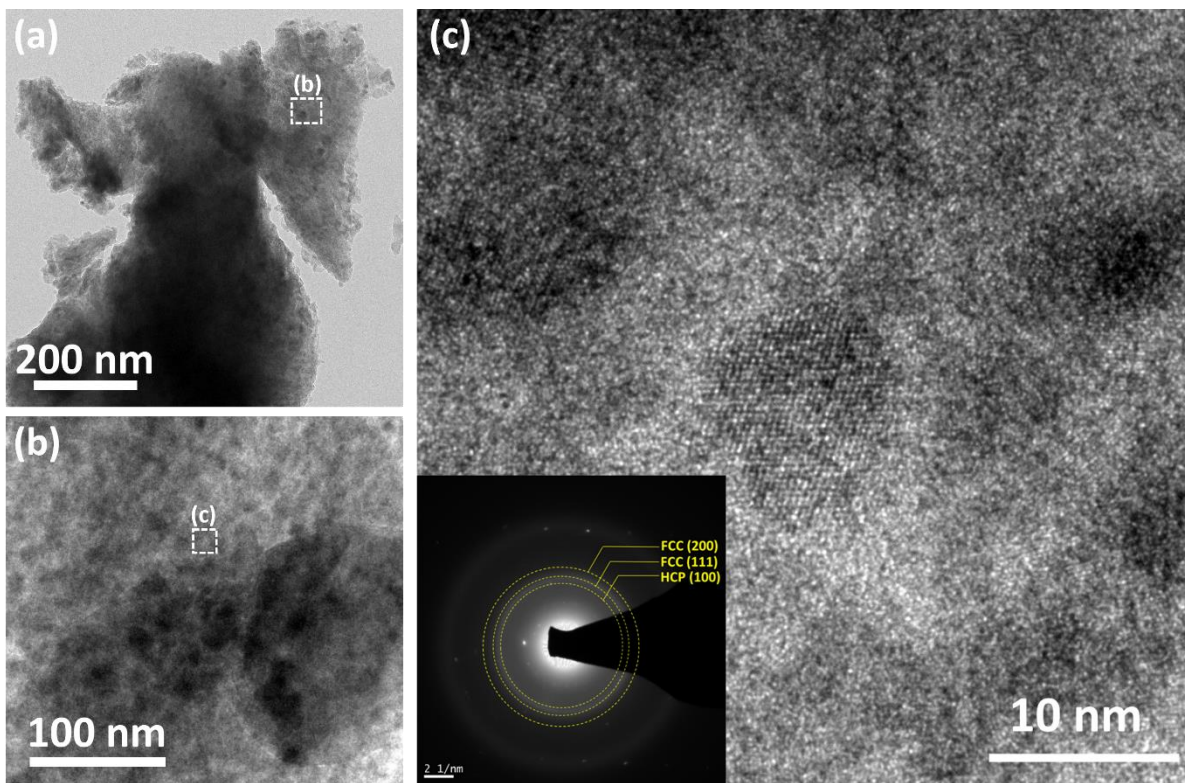
Figure 2.9: TEM image and associated SAED pattern (inset) for $AlTi_{0.45}CuZn$ HEA at extended milling time.

Despite the development of other empirical phase rules, the formation of SS at the expense of IM compounds during MA has been attributed to mainly high ΔS_{mix} of the system, and the severe strain applied to the powder particles enhances the accumulated energy of the system [82]. However, in this work, ΔS_{mix} between 11 and 11.53 J/K-mol (theoretical maximum for quaternary alloys) was

not enough to prevent IM compound formation in all AlTiCuZn-based HEAs except for AlTi$_{0.45}$CuZn (ΔS_{mix} = 11.16 J/K-mol); this suggests that configurational entropy alone may not be sufficient to overrule the competing driving forces which regulate phase stability [100],[101]. Similarly, only the AlTi$_{0.45}$CuZn with the highest values of ΔH_{mix} and Ω, and lowest value of δ among the AlTiCuZn-based HEAs experimentally validate the predicted SS criteria in **Table 2.4**. This suggests that higher Ω and ΔH_{mix}, and lower δ values than the conventional values might be required to obtain SS in AlTiCuZn-based HEAs.

2.3.3.2 More conservative phase prediction criteria for AlTiCuZn-based HEAs

As can be seen in **Figure 2.6(c)**, Al$_{0.45}$TiCuZn and Al$_{0.57}$TiCuZn HEAs showed IM compound phases majorly with minor FCC and HCP phases, whereas AlTiCu$_{1.76}$Zn and AlTiCu$_2$Zn HEAs exhibited major FCC phase with minor HCP and IM compound phases. From all these observations (also tabulated in **Table 2.6**), we can safely conclude that the empirical SS formation criteria for AlTiCuZn-based HEAs are more conservative than the classical empirical rules. Hence, using AlTi$_{0.45}$CuZn HEA as a guide, the approximate requirement for complete SS formation in AlTiCuZn-based HEAs is: $\Omega \geq 1.6$, $\delta \leq 5\%$, and $\Delta H_{mix} \geq$ -8 kJ/mol, while the traditional ΔS_{mix} and $\triangle \chi$ requirements are maintained. As the Ω and ΔH_{mix} values decline and δ value increases outside this range, the probability of IM compound formation will also increase accordingly. Based on these new ranges, the updated ΔH_{mix}-δ and Ω-δ plots for AlTiCuZn-based HEAs are presented in **Figure 2.10**.

Table 2.6: Theoretical values of δ, ΔH_{mix}, and Ω and experimentally obtained phases for AlTiCuZn-based HEAs with descending order of ΔH_{mix} and Ω.

Alloy	δ (%)	ΔH_{mix} (kJ/mol)	Ω	Predicted Phases	Actual Phases
AlTi$_{0.45}$CuZn	4.88	-7.81	1.60	FCC	FCC (major) + HCP (minor)
AlTiCu$_2$Zn	5.53	-9.92	1.40	FCC	FCC (major) + HCP (minor) + IM (minor)
AlTiCu$_{1.76}$Zn	5.45	-10.56	1.33	FCC	FCC (major) + HCP (minor) + IM (minor)
Al$_{0.45}$TiCuZn	5.20	-12.26	1.16	FCC	IM (major) + FCC (minor) + HCP (minor)
Al$_{0.57}$TiCuZn	5.14	-12.59	1.14	FCC	IM (major) + FCC (minor) + HCP (minor)
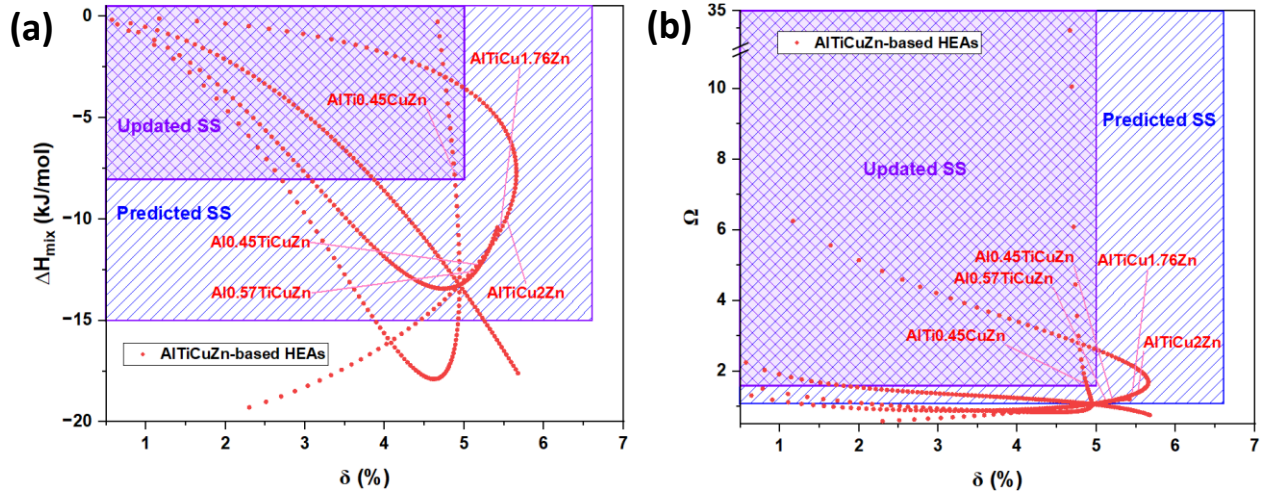
Figure 2.10: Modified **(a)** ΔH_{mix}-δ and (b) Ω-δ plots with updated SS ranges for AlTiCuZn-based equiatomic and semi-equiatomic HEAs.

The updated SS requirements for AlTiCuZn-based HEAs are close to that of MoNbTaW, HfNbTaTiZr, and MoNbTaWV refractory HEAs (ΔH_{mix} > -7.5 kJ/mol and δ < 4.5%), but less conservative than that of low-density alloys consisting of considerable amounts of Al, Mg, and Li ($\Omega \geq 10$, δ < 4.5%, and -1 kJ/mol $\leq \Delta H_{mix} \leq$ 5 kJ/mol) [34],[71]. This conservation in SS formation criteria for AlTiCuZn-based HEAs could be attributed to the differences in bonding nature of their constituent elements, and the competition between their entropy and enthalpy

facilitates IM compound formation instead of SS [34],[101]. Also, previous work suggested that the conservation in SS formation criteria is due to the lack of d-orbitals in the constituent elements of the HEA that impedes higher-order hybridization [34]. But this may not be applicable for AlTiCuZn-based HEAs as all the constituent elements are d-block, except Al. However, good chemical compatibility among the Al, Ti, Cu, and Zn elements, rather than configurational entropy, could be more vital to determine the microstructural condition of the AlTiCuZn-based HEAs [101].

2.3.3.3   A revisit of the VEC rule for HEA with HCP structure

While the benchmarked AlCoCrFe HEA showed a single-phase BCC structure in agreement with the traditional VEC rule, none of the AlTiCuZn-based HEAs completely followed the traditional VEC rule that predicts an all-single-phase FCC structure. Although $AlTi_{0.45}CuZn$, $AlTiCu_{1.76}Zn$, and $AlTiCu_2Zn$ primarily exhibited the FCC phase following the conventional VEC rules, other minor phases including an HCP structure constitute the microstructure. It has previously been observed that for low-density HEAs containing Al, Zn, and Cu, the conventional VEC rules can be unreliable [34]. Moreover, the traditional VEC rule is known to be effective mainly for equiatomic or semi-equiatomic HEAs without having IM compound phases [11]. Since the semi-equiatomic $Al_{0.45}TiCuZn$, $Al_{0.57}TiCuZn$, $AlTiCu_{1.76}Zn$, and $AlTiCu_2Zn$ HEAs contained IM compound phases, the violation of the conventional VEC rules becomes valid. But even though semi-equiatomic $AlTi_{0.45}CuZn$ HEA did not contain any IM compound phase, the conventional VEC rule was unable to predict its crystal structure accurately.

The traditional VEC rule reported by Guo et al. [67] does not include the criteria for the formation of an HCP structure, and thus requires a revisit. Recently, stable HCP structure was reported for

lightweight elements (*VEC* = 2.8), lanthanide alloys (*VEC* = 3), and $Ir_{25.5}Mo_{20}Rh_{20}Ru_{25}W_{9.5}$ and $Ir_{26}Mo_{20}Rh_{22.5}Ru_{20}W_{11.5}$ HEAs (*VEC* ~ 7.86) [102]. Specifically, a $7.5 \leq VEC \leq 8.4$ modified VEC rule for HEAs with HCP phase (i.e., HCP or BCC + HCP or FCC + HCP or BCC + FCC + HCP) has been deemed accurate for the HEAs constituting 4d and 5d transitional metals along with the requirement that these alloys are annealed near the solidus temperature [102,103]. From the *VEC* values of the AlTiCuZn-based HEAs (**Table 2.4**), it is obvious that *VEC* ~ 8 promotes the formation of FCC + HCP dual-phase. However, the AlTiCuZn-based HEAs mainly constitute 3d transitional metals, and these alloys did not undergo any annealing process. Therefore, we posit that d-block elements in HEAs, irrespective of their energy levels, can facilitate FCC + HCP dual phase formation as long as the $7.5 \leq VEC \leq 8.4$ criterion is satisfied. The *VEC* values of other dual phases FCC + HCP HEAs (calculated using Eqn. 2.7), $Fe_{50}Mn_{30}Co_{10}Cr_{10}$ (*VEC* = 7.6) [47,65], $Co_{20}Cr_{20}Fe_{34}Mn_{20}Ni_6$ (*VEC* = 7.72) [92], $Fe_{39}Mn_{20}Co_{20}Cr_{15}Si_5Al_1$ (*VEC* ~ 7.5) [93], and $Fe_{38.5}Mn_{20}Co_{20}Cr_{15}Si_5Cu_{1.5}$ (*VEC* = 7.545) [93], also fall within this range. Based on this new criterion combined with the modified δ range ($\delta \leq 5\%$), an updated *VEC*-δ plot for AlTiCuZn-based HEAs is shown in **Figure 2.11**.
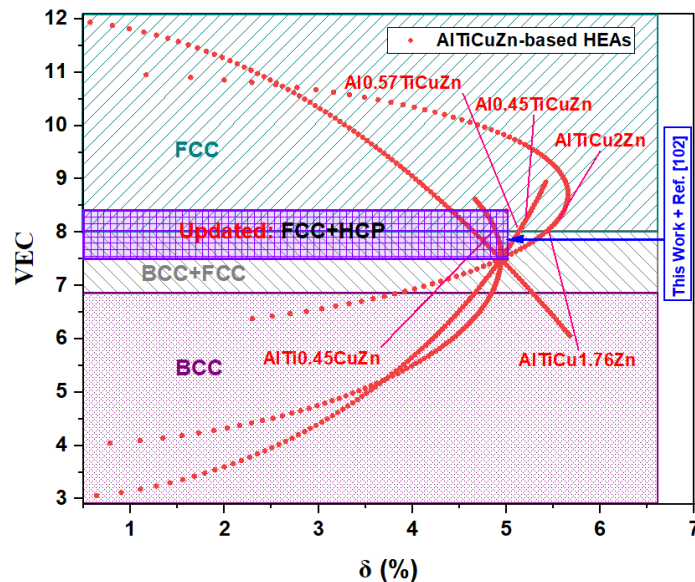
Figure 2.11: Modified *VEC-δ* plot for AlTiCuZn-based HEAs. The violet marked region in this plot shows the required *VEC* range for HCP SS-containing phases (i.e., HCP or BCC + HCP or FCC + HCP or BCC + FCC + HCP).

2.3.3.4   Verification of the revised criteria: the development of new non-equiatomic AlTiCuZn-based HEAs

To verify the revised SS and VEC criteria for AlTiCuZn-based HEAs, two new non-equiatomic HEAs that fulfilled the revised criteria—$AlTi_{0.37}CuZn_{0.97}$ and $AlTi_{0.56}Cu_{1.24}Zn_{1.2}$—were fabricated by following the same processing condition as the previously developed alloys. From the revised empirical rules in *Sections 3.3.2 and 3.3.3*, dual phase FCC and HCP SS is predicted for both $AlTi_{0.37}CuZn_{0.97}$ ($VEC = 8.12$, $\Omega = 1.8$, $\delta = 4.88\%$, $\Delta H_{mix} = $ -6.73 kJ/mol, $\Delta S_{mix} = 11.01$ J/K-mol, and $\triangle \chi = 0.134$) and $AlTi_{0.56}Cu_{1.24}Zn_{1.2}$ ($VEC = 8.32$, $\Omega = 1.6$, $\delta = 4.97\%$, $\Delta H_{mix} = $ -7.92 kJ/mol, $\Delta S_{mix} = 11.19$ J/K-mol, and $\triangle \chi = 0.137$) alloys. As observed from their XRD patterns (**Figure 2.12**), these new HEAs also exhibited SS with FCC and HCP dual phases at 40 h of milling similar to $AlTi_{0.45}CuZn$ HEA. This verifies the updated VEC and SS criteria for AlTiCuZn-based HEAs.

45
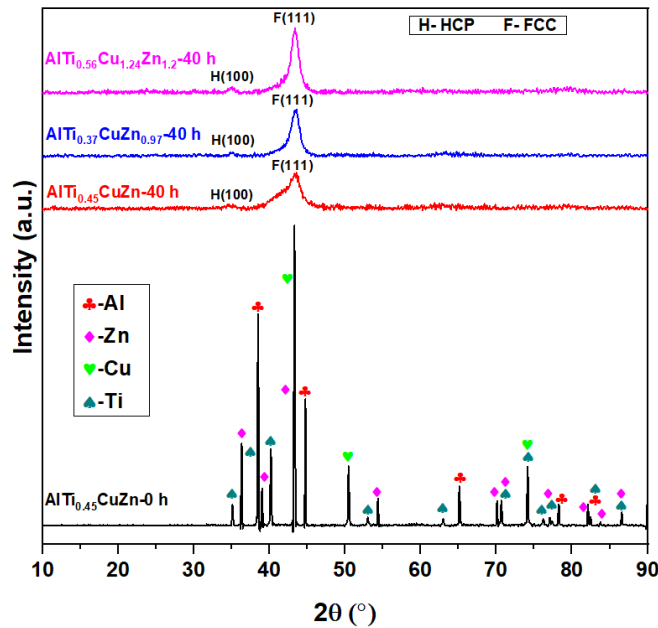
Figure 2.12: XRD patterns of newly fabricated $AlTi_{0.37}CuZn_{0.97}$ and $AlTi_{0.56}Cu_{1.24}Zn_{1.2}$ non-equiatomic HEAs at 40 h of milling with 1 wt.% Ethanol as the PCA. XRD patterns of $AlTi_{0.45}CuZn$ HEA at 0 h and 40 h of milling are added here for comparison.

2.4 Summary and Conclusion

Obtaining SS structures is usually desirable in HEAs as the presence of IM compounds can, in some cases, be deleterious. Over the years, the empirical phase stability rules have become a very useful tool to predict the SS formation and crystal structure in HEAs. This study was conducted to assess the accuracy of these rules by isolating the effect of processing pathways, and further investigating the alloy-specific nature of these rules. To this end, an existing AlCoCrFe HEA was first benchmarked, and novel AlTiCuZn-based quaternary HEAs—$Al_{0.57}TiCuZn$, $AlTi_{0.45}CuZn$, $Al_{0.45}TiCuZn$, $AlTiCu_{1.76}Zn$, and $AlTiCu_2Zn$—were fabricated via MA process and characterized. The following conclusions can be drawn:

I.   As the milling progressed, the dissolution of the peaks for the alloys in XRD patterns depends on the melting point of constituting elements instead of the atomic number.

II. PCA concentration affected the dissolution of peaks in the XRD patterns but had no impact on the formation of SS or IM compound.

III. According to the phase stability rules, fabricated AlCoCrFe and AlTiCuZn-based HEAs should possess single-phase BCC and FCC SS structures, respectively. Experimentally, AlCoCrFe develop a BCC SS following the empirical rules, whereas only $AlTi_{0.45}CuZn$ developed SS among all the AlTiCuZn-based HEAs but contained FCC and HCP dual phases that violated the VEC rule.

IV. More conservative SS criteria for AlTiCuZn-based HEAs were established considering $AlTi_{0.45}CuZn$ HEA as a guide—$\Omega \geq 1.6$, $\delta \leq 5\%$, and $\Delta H_{mix} \geq -8$ kJ/mol, apart from the

conventional ΔS_{mix} and $\triangle \chi$ requirements. IM compound formation probability is enhanced outside these ranges. Also, the *VEC* range was revised to $7.5 \leq VEC \leq 8.4$ for the formation of dual-phase FCC + HCP in HEAs. Two new non-equiatomic HEAs—$AlTi_{0.37}CuZn_{0.97}$ and $AlTi_{0.56}Cu_{1.24}Zn_{1.2}$ were fabricated to verify the revised phase stability rules.

V.   For the AlTiCuZn-based HEAs, good chemical compatibility among the constituent elements instead of the configurational entropy might have more contribution in controlling their microstructural conditions.

VI. Despite isolating the effect of processing pathway, the classical empirical rules breakdown in some alloy systems; this strongly affirm that the breakdown can be alloy-dependent.

Chapter 3: From phase decomposition to evaporation: A multi-modal evaluation of thermally degraded model lightweight high-entropy alloy

Abstract

Lightweight high-entropy alloys (LHEAs) have the potential to replace conventional lightweight materials due to their superior mechanical properties and thermal stability. However, the thermal degradation pattern of LHEAs from phase decomposition to evaporation is not clear. We develop a new Al-based dual phase (FCC + HCP) LHEA—AlTi$_{0.45}$CuZn, and further investigate its thermal degradation behavior for potential high-temperature structural applications. Using multimodal advanced characterization techniques such as differential scanning calorimetry/thermogravimetric analysis, scanning/transmission electron microscopy, and synchrotron X-ray diffraction/pair distribution function (XRD/PDF), a sequence of thermal degradation events beyond the thermal phase stability limit—between 250 and 360 °C—is observed. These include phase decomposition at ~360 °C, Zn evaporation at ~750 °C, and LHEA melting at 880 °C which results in ~25% cumulative weight loss. The formation of Al-Ti phase off the AlTi$_{0.45}$CuZn matrix is due to the largest negative mixing enthalpy for Al-Ti than other binary pairs. Similarly, Zn evaporation from AlTi$_{0.45}$CuZn LHEA is due to its faster evaporation rate than other constituent elements. The high-resolution synchrotron XRD and PDF results support the aforementioned observations; in addition, they reveal local atomic arrangements, local strain, and sluggish grain growth in the LHEA. Among other LHEAs of close density range ($5.55 \leq \rho \leq 5.85$ g/cc), the investigated LHEA exhibits outstanding nano-indentation hardness values due to the coupled grain size effect and HCP phase strengthening of the FCC matrix. As the search for LHEAs for lightweight applications grows, this study shows the potential use of AlTi$_{0.45}$CuZn LHEA for structural applications even at elevated temperatures.

3.1 Introduction

The use of lightweight materials with high strength-to-weight ratio are extensively sought especially in the military, energy, transportation, and aerospace sectors; this is because they lower component weights, and in turn, decrease energy consumption and greenhouse gas emissions [50]. A new class of alloy that meets this urgent need is the high-entropy alloys (HEAs). HEAs are multicomponent solid-solution alloys with at least four principal elements in equal or non-equal concentration; they have outstanding mechanical and functional properties compared to traditional alloys with one or two principal elements [4,104]. The multi-elemental mixtures in HEAs result in sluggish diffusion, high-entropy, severe lattice distortion, and cocktail effects [22,23]. The sluggish diffusion effect results in superior thermal stability [105], while the ability to develop a combination of phases, including amorphous structure, results in high resistance against oxidation and corrosion, and other outstanding mechanical properties [104], for different structural and functional applications [106]. While there are extensive studies on five or more equiatomic HEAs, those with four principal elements in non-equimolar ratios have recently garnered attention because of the ease of tailoring dual-phase microstructures to access a combination of properties that are typically exclusive to each of the individual phases [26].

There are several classes of HEAs, including the lightweight class for aerospace and transportation applications [6]. Lightweight HEAs (LHEAs) are based on elements such as Al, Ti, Zn, Cr, Fe, Be, Li, Mg, Ca, Mn, Sc, Si, Ni, Sn, Mo, Zr, Cu, Nb, and V, and they (LHEAs) possess low density (typically <7 g/cc [50]), high specific hardness and strength, high oxidation resistance, and excellent wear and corrosion resistance [6,50]. LHEAs are believed to exhibit better performance than traditional lightweight materials, including Al-, Ti-, and Mg- alloys; for instance, the hardness

values of $Al_{20}Li_{20}Mg_{10}Sc_{20}Ti_{30}$ LHEA and traditional aerospace Al-Cu alloys of comparable densities are 599 and 131 HV, respectively [33,51,52]. In addition, $Al_{20}Be_{20}Fe_{10}Si_{15}Ti_{35}$ LHEA with density of 3.91 g/cc possesses a good hardness value of 911 HV and greater oxidation resistance compared to the Ti-6Al-4V alloy [53,54]. Relatively new $Al_{35}Cr_{14}Mg_6Ti_{35}V_{10}$ LHEA has a hardness value of 460 HV, which is greater than all classes of traditional titanium alloy [50,107]. $Al_{80}Li_5Mg_5Zn_5Cu_5$ and $Al_{80}Li_5Mg_5Zn_5Sn_5$ low-density alloys reported by Yang et al. [34] exhibited good compressive strengths of 879 and 836 MPa along with 16% and 17% plastic strains, respectively.

Although traditional lightweight Al-based alloys have been widely used in automotive, construction and aerospace industries, their mechanical properties and phase stability deteriorate at a much lower temperature than most LHEAs; this can impedes their (traditional Al-based alloys) extensive applications at elevated temperatures [62,63]. For instance, the compressive strengths of 10 h solution-treated $Al_{70}Mg_{10}Si_{10}Cu_5Zn_5$ LHEA are 723 ± 8 MPa at room temperature and 113 MPa at 350 °C, which are higher than that of the conventional cast alloys (A356 and A390) [63,108]. Again, the yield strength of conventional 2024-T6 Al-Cu wrought alloy is 395 MPa at room temperature, which drops to 95 and 55 MPa after annealing at 315 °C for 0.5 h and 100 h, respectively [109]. Similarly, the yield strengths of 5083-H116 and 6061-T651 Al-alloys at room temperature are ~275 and ~320 MPa, respectively, and they drop to ~90 and ~100 MPa, respectively, at 300 °C [110]; these values are low compared to the ones reported for LHEAs [50,55,62,63]. For example, low-density $Al_{77}Cu_{17}Zn_3Mg_2Cr_1$ alloy exhibited a yield strength of 588 MPa at room temperature, while it retained a yield strength of 199 MPa after 100 h of annealing at 300 °C [62]. AlNbTiV LHEA showed high compressive yield strength values of 1020 MPa at room temperature and 685 MPa at 800 °C [55]. The yield strengths of

$Al_{78}Cu_{18}Zn_2Cr_1Fe_1$, $Al_{78}Cu_{18}Zn_1Cr_2V_1$, and $Al_{78}Cu_{18}Zn_1Cr_2Ti_1$ alloys are 351, 387, and 383 MPa, respectively, and they show outstanding thermal stability after annealing at 300 °C—224, 204, and 223 MPa yield strengths, respectively [63]. On phase stability of Al-containing LHEAs, nanocrystalline (NC) AlMgSiCrFeNi showed phase stability up to 400 °C after which intermetallic phase formed [9], while AlMgMnZnCu shows high phase stability up to 700 °C [111]. Furthermore, $AlTiV_{0.5}CrMo$ LHEA exhibited excellent phase stability when heat-treated at 800 °C, but with accompanied grain growth from 8 to 51.4 nm [112]. According to differential thermal analysis of as-milled AlFeCuCrMg-based HEAs, thermal phase stability was observed up to 500 °C [113].

Despite all these works suggesting Al-containing LHEAs' potential for high-temperature applications, further detailed multimodal studies are needed to understand their thermal deteriorative behavior. We recently designed and developed novel AlTiCuZn-based LHEAs by mechanical alloying process [7]. Among the AlTiCuZn-based LHEAs, the most promising $AlTi_{0.45}CuZn$ LHEA with a theoretical density of 5.71 g/cc showed a rare FCC + HCP dual-phase solid-solution structure. Until now, $Fe_{38.5}Mn_{20}Co_{20}Cr_{15}Si_5Cu_{1.5}$ [93], $Co_{1.75}CrFeMnNi_{0.25}$ [114], $Fe_{50}Mn_{30}Co_{10}Cr_{10}$ [47,65], $Fe_{39}Mn_{20}Co_{20}Cr_{15}Si_5Al_1$ [93], and $Co_{20}Cr_{20}Fe_{34}Mn_{20}Ni_6$ [92] are among the few HEAs with FCC + HCP dual-phase structure, but their theoretical densities (7.35-8.04 g/cc) are much higher compared to $AlTi_{0.45}CuZn$ LHEA. The presence of an HCP phase in an FCC-type HEA is known to enhance its mechanical properties. For instance, Wang et al. [114] reported that among their developed $Co_xCrFeMnNi_{2-x}$ (x = 0.25–1.75) alloys, $Co_{1.75}CrFeMnNi_{0.25}$ showed the highest hardness of 213 HV due to the substantial amount of HCP phase within the FCC matrix. Even after annealing, the hardness of $Co_{1.75}CrFeMnNi_{0.25}$ was higher than other FCC alloys without the HCP phase [114]. Li et al. [47,65] reported FCC phase transition in

Fe$_{80-x}$Mn$_x$Co$_{10}$Cr$_{10}$ to FCC + HCP dual-phase as the Mn content decreased from 45 at.% to 30 at.%. The FCC + HCP dual-phase HEA with 28% HCP phase exhibited higher ultimate tensile and yield strengths than several other FCC single phase HEAs [94]. Again, Li et al. [92] prepared FCC + HCP dual-phase Co$_{20}$Cr$_{20}$Fe$_{40-x}$Mn$_{20}$Ni$_x$ (x = 0-20 at.%) HEAs with 6%-69% HCP phase via a similar method, and superior tensile strength and strain-hardening ability were exhibited by the dual-phase HEA containing 69% HCP phase. These results pave a new way for designing FCC-structured HEAs with targeted mechanical properties via HCP phase strengthening [114].

Based on the potentials of Al-containing LHEAs for high-temperature applications and the advantages of FCC + HCP dual-phase crystal structure formation, we investigate the thermal stability and mechanical performance of AlTi$_{0.45}$CuZn LHEA—the first Al-based FCC + HCP dual-phase LHEA to the best of our knowledge. The goal is to understand the complex relationships that exist between alloy composition, microstructure, and properties that span a wide range of temperatures to provide the basis for improved thermal stability in the design of modern alloys. Upon mechanical alloying, as-milled/annealed AlTi$_{0.45}$CuZn LHEA samples were characterized using differential scanning calorimetry/thermogravimetric analysis (DSC/TGA) to determine materials' behavior as a function of temperature, scanning/transmission electron microscopy (S/TEM) for microstructural evaluation, and synchrotron-based X-ray diffraction/pair distribution function (s-XRD/PDF) for evaluation of crystal structure (at a higher resolution) and local atomic arrangements. This was followed by mechanical characterization of as-milled and annealed LHEA samples by nano-indentation method.

3.2 Materials and Methods

3.2.1 Mechanical Alloying Process

The semi-equiatomic $AlTi_{0.45}CuZn$ LHEA was developed by milling elemental powders—Al, Ti, Cu, and Zn—in an atomic ratio of 29:13:29:29. The milling process was performed in a planetary ball mill (PBM-04, MicroNano Tools) using stainless steel balls (with a ball-to-powder ratio of 10:1) and 1 wt.% ethanol process control agent. During milling, an inert gas atmosphere was maintained inside the zirconia vacuum grinding jars with stainless steel jackets. The elemental powders were first premixed at 100 rpm for 1 h, followed by the actual milling at 350 rpm for up to 60 h; samples were intermittently taken out for scanning electron microscopy (SEM) and powder XRD characterizations. More details about the milling process and parameters can be found in Ref. [7].

3.2.2 Heat Treatment and Characterizations of Samples

The SEM analyses of the as-milled samples were carried out via Bruker Nano GmbH Berlin, Germany, which is equipped with a XFlash 5030 type energy dispersive spectroscopy (EDS) detector and operated at 20 keV—for evaluating particle morphology and elemental distribution. The long-range DSC/TGA analysis of the as-milled sample was conducted in a 50-915 °C temperature range using Mettler Toledo TGA/DSC3+ equipment in a nitrogen gas inert atmosphere with a heating rate of 10 K/min. To observe the effect of different heating rates (5, 10, 15, and 20 K/min), a short-range DSC analysis (30-550 °C) was carried out on the as-milled sample using Mettler Toledo DSC3 equipment in a similar inert environment. The DSC curves were analyzed using STAR^e software (v. 14.00) from Mettler Toledo.

Based on the DSC analysis, the annealing of the as-milled powder was performed at 250, 450 and 650 °C temperatures for 4 h at each temperature in a LINDBERG SOLA BASIC+ tube furnace. The powder was first mounted in a platinum crucible, and then, the crucible was placed inside the furnace's quartz glass tube where an inert argon gas environment (with ~200 mL/min flow rate) was constantly maintained. The furnace temperature was augmented from room temperature to the desired temperatures at 25 °C/min heating rate; after each heating cycle, the annealed samples were instantaneously quenched in water at room temperature.

The grain sizes and crystal structures of the as-milled and annealed samples were determined via an X-ray powder diffractometer (Bruker D8 Advance (ECO), with a highly sensitive Lynxeye XE energy dispersive 1D detector) with Cu K_α ($\lambda = 0.15418$ nm) radiation over a scanning angle range (2θ) of 10º-90º and 2.3 º/min scanning rate. The phase formation and grain size were evaluated through DIFFRAC.EVA (v. 5.2, Bruker) software. The TEM lamella was prepared via a ThermoFisher Scientific Helios G5 DualBeam focused ion beam (FIB) using an in-situ lift-out process; afterwards, the sample thickness was progressively reduced by gradually decreasing the Ga^+ beam voltages, until ~50 nm thickness was attained. Using a TEM Cu grid, ThermoFisher Scientific X-FEG Talos F200X with a Super-X EDS detection system, operating at an accelerating voltage of 200 keV, was employed for the S/TEM analyses on both as-milled and annealed samples.

The phase and long-range order of the as-milled and annealed samples were measured using transmission mode, high-energy synchrotron-based XRD (s-XRD) and PDF at the National Synchrotron Light Source II (NSLS-II), Brookhaven National Laboratory, Beamline 28-ID-2. The transmitted X-rays were collected with a flat-panel X-ray detector (Dexela 2923 CMOS, 75 μm pixel size). The energy of the incident X-rays was 68.2 keV, with a beam size of approximately

0.25 mm wide and 0.25 mm high. Lanthanum Hexaborate (LaB_6 – NIST SMR660c) powder was used as a calibrant to refine the sample-to-detector distance and the tilts of the detector with respect to the x-ray beam. The sample-to-detector distance was 0.7143 m. (0.3467 m.) for XRD (PDF) setup. The detector acquisition time was set as 0.1 second. To improve statistics, multiple frames were averaged. The resultant 2-D data were transformed into 1-D pattern by utilizing the PyFAI software [115]. The grain size of the samples was calculated using the Scherrer equation [116], while their lattice strain was obtained using the Williamson-Hall equation as given below [23]:

$$\beta cos\theta = \frac{0.89\lambda}{D} + 4\varepsilon sin\theta \dots \dots \dots (3.1)$$

where, θ is the diffraction angle, λ is the wavelength of the X-ray beam, D is the grain size, β is full-width at half maximum intensity of the diffraction peak, and ε is the lattice strain. The phase analysis of the powder diffraction data was evaluated using Match 3! Software, which includes the crystallography open database [117]. An insight into the local atomic arrangements and the associated changes due to annealing were assessed by the PDF. The PDF data was obtained by the Fourier transformation of the structural function, S(Q), using the PDFgetX3 [118] over a radial range of $r = 0.5 – 20$ Å.

3.2.3   Nano-indentation Experiment

The as-milled and annealed samples were cold pressed using a YLJ-15 hydraulic pellet press with a 6 mm diameter die and 2.26 metric ton load. The cold pressing was performed in a vacuum environment to reduce interparticle pores and the displacement of particles during nano-indentation. Before nano-indentation, cold-pressed samples were polished following the standard metallographic polishing steps [119], and subsequently, vibratory polishing was carried out for 4 h using a 0.025 μm colloidal silica polishing solution in a BUEHLER VibroMet2 equipment

operating at 20% vibration amplitude. The nano-indentation test on the polished sample was carried out using a Hysitron TI Premier nano indenter by Brucker using a maximum load of 1000 µN and basic quasi static trapezoid load function to measure the hardness of the samples. A standard Berkovich probe with ~150 nm tip radius was used, and 20 nano-indentation tests were performed for each sample for reliability and repeatability of the results. TriboScan (v. 9) software from Hysitron, which is based on the Oliver-Pharr model [120], was used to analyze nanoindentation data.

3.3   Result and Discussion

3.3.1   Microstructural Evaluation of As-milled AlTi$_{0.45}$CuZn LHEA

The powder XRD patterns for AlTi$_{0.45}$CuZn LHEA as a function of milling time are shown in **Figure 3.1(a)**. At 0 h of milling, the peaks corresponding to FCC-Al, HCP-Ti, FCC-Cu, and HCP-Zn elements are present. With the increasing milling time, lattice diffusion is promoted due to the repeated cold-welding and collision of the particles [82], and the subsequent disappearance of Al and Zn peaks that is suggestive of the onset of alloying can also be observed [7]. At 20 h of milling and above, an FCC + HCP dual-phase solid-solution structure develops, but powders were further milled up to 60 h to ascertain the complete dissolution of alloying elements. **Figures 3.1(b)** and **3.1(c)** show the SEM images with EDS maps of the AlTi$_{0.45}$CuZn LHEA corresponding to 10 h and 40 h milling times, respectively. The constituents of the LHEA are predominantly mixed at 10 h milling time, except for the unmixed Ti. As higher melting point elements have stronger interatomic bonds, Ti which has the highest melting point in the alloy mix has lower alloying rate and thus requires a longer milling time for uniform dissolution compared to other elements [84]. At 40 h milling time, all constituent elements of the LHEA are uniformly mixed, which implies

56

alloy formation in support of the XRD results in **Figure 3.1(a)**. According to the EDS point analysis, the concentrations of Al, Ti, Cu, and Zn elements are 26.2 ± 4, 15.4 ± 2, 28.9 ± 2, and 29.5 ± 2
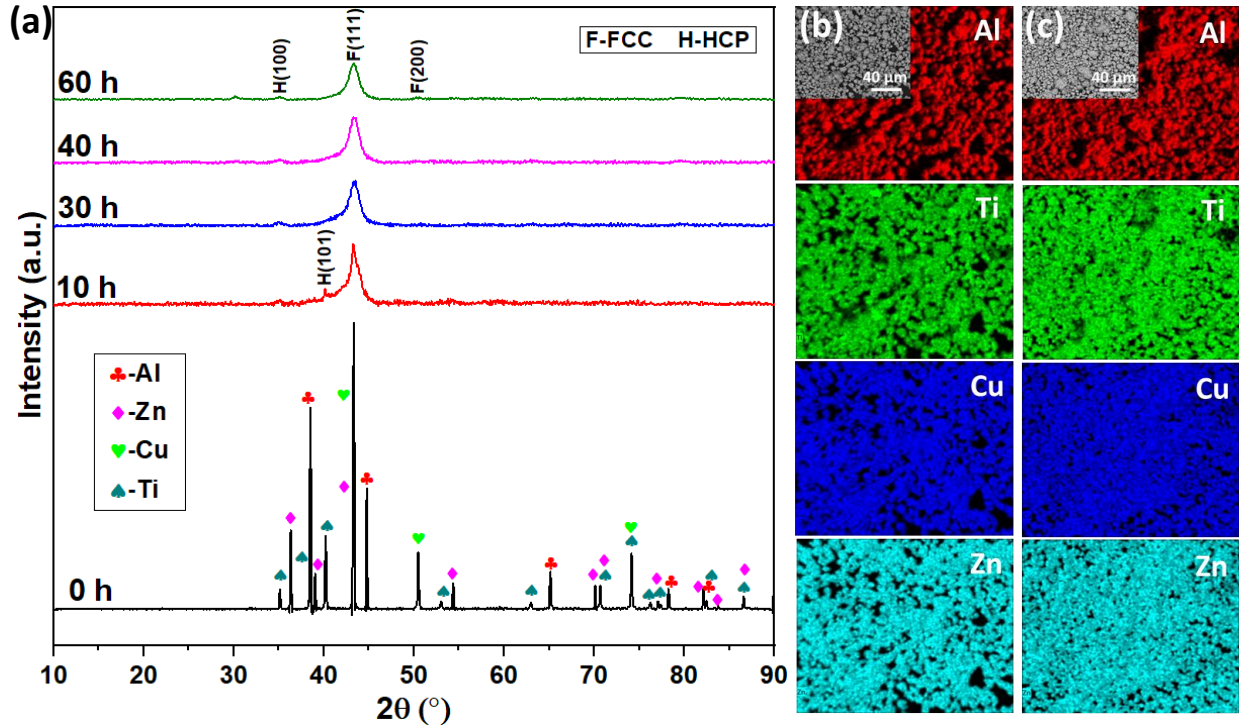
Figure 3.1: (a) Powder XRD patterns for AlTi$_{0.45}$CuZn LHEA milled at different times from 0 h to 60 h; and SEM/EDS maps of the as-milled LHEA at **(b)** 10 and **(c)** 40 h milling times. The SEM/EDS maps in (b) and (c) are reproduced from Ref. [7] for completeness.

at.%, respectively. Furthermore, **Figure 3.1(a)** shows that increasing milling time coincides with peaks' intensity reduction along with their broadening; this is an indication of grain refinement during milling because of the recurring plastic deformation and total dissolution of atoms [85]. By employing DIFFRAC.EVA software that utilizes Scherrer's equation, the grain size of AlTi$_{0.45}$CuZn LHEA (60 h of milling) is determined as ~6 nm using the FCC (111) peak from the X-ray diffractogram. The theoretical melting temperature (T_m) of the AlTi$_{0.45}$CuZn LHEA was calculated as ~845 °C following an empirical equation [7]. In what follows, the nanostructure of 60 h-milled AlTi$_{0.45}$CuZn LHEA sample is examined.
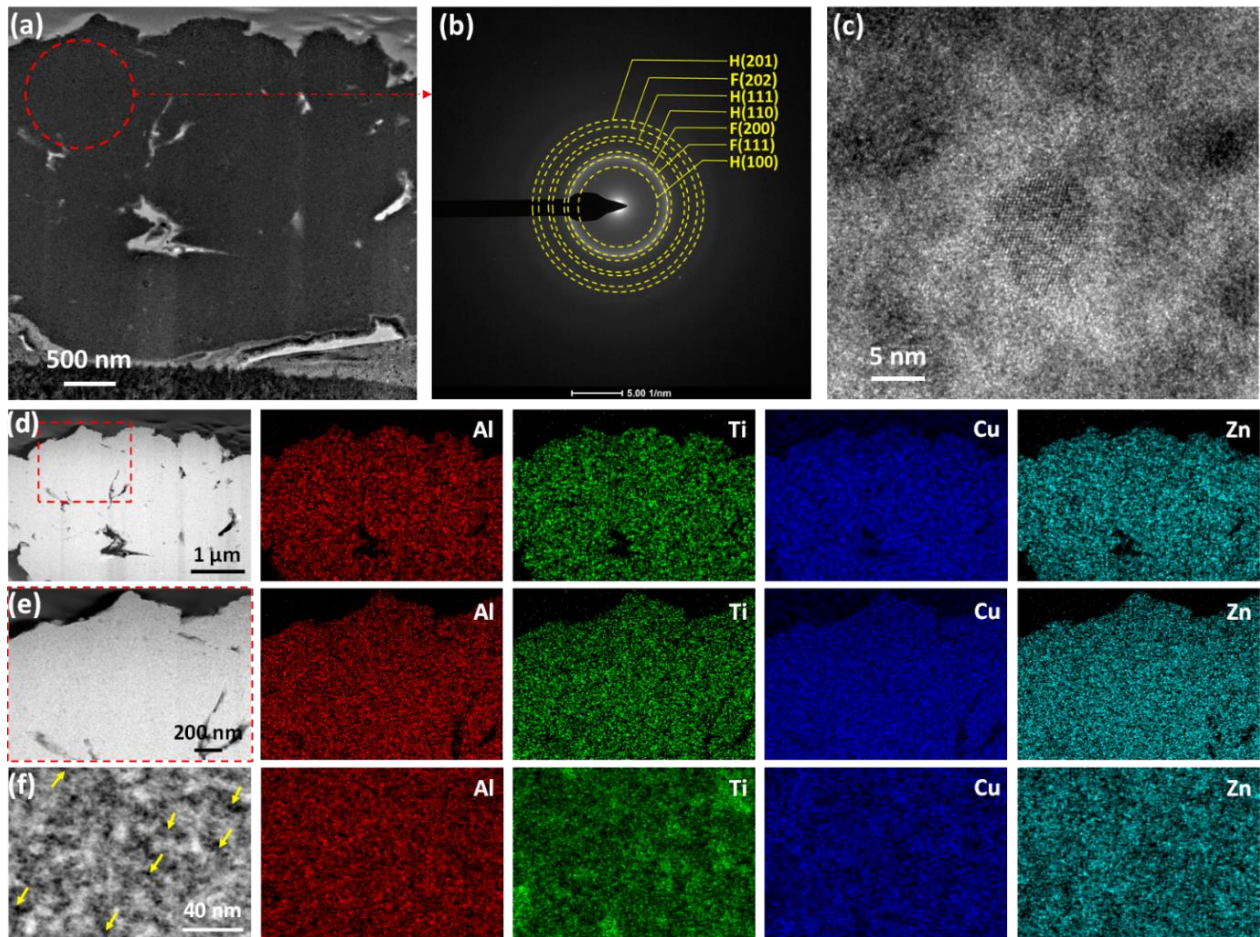
Figure 3.2: S/TEM micrographs and EDS maps of the cross-sectioned LHEA particle in the as-milled condition: **(a)** Low-magnification TEM micrograph and **(b)** the SAED patterns associated with the red-circled region in (a); **(c)** High-resolution TEM micrograph; and **(d-f)** STEM-HAADF micrographs with corresponding EDS maps obtained at **(d)** low-, **(e)** medium-, and **(f)** high-magnifications. The yellow arrows in (f) indicate Ti-rich HCP phase regions. The TEM micrograph in (c) is reproduced from Ref. [7] for completeness.

The cross-sectional TEM image of the LHEA is shown in **Figure 3.2(a)**, while the selected-area electron diffraction (SAED) pattern corresponding to the marked region in **Figure 3.2(a)** is presented in **Figure 3.2(b)**. The SAED pattern confirms the formation of FCC + HCP dual-phase solid-solution structure in AlTi$_{0.45}$CuZn LHEA due to the presence of HCP (100), FCC (111), FCC (200), HCP (110), HCP (111), FCC (202), and HCP (201) diffraction rings; this agrees with the XRD pattern shown in **Figure 3.1(a)**. The high-resolution TEM micrograph in **Figure 3.2(c)**

shows a few nanograin formations with an average size of 8 ± 1 nm using ImageJ software [79], which is close to the estimated grain size from the XRD results (~6 nm).

The chemical homogeneity of the as-milled LHEA is confirmed by the cross-sectional low-and "medium"-magnification STEM high-angle annular dark field (HAADF) micrographs and EDS maps in **Figures 3.2(d)** and **3.2(e)**, respectively. However, at high-magnification (**Figure 3.2(f)**), the EDS map shows that the dark contrast regions in STEM-HAADF image (indicated by yellow arrows) are nano-sized Ti-rich HCP phase regions; the HCP phase is 18 ± 2 nm in average size within the Cu-Zn-Al rich FCC matrix of the LHEA. This agrees well with the XRD results in **Figure 3.1(a)** because the lattice parameters of the HCP phase are similar to that of HCP-Ti ($a =$ 2.95 Å, $c = 4.68$ Å), and the major and minor phases of the LHEA are FCC and HCP, respectively. This is further supported by the closeness in interplanar spacing (d-spacing) values of Ti (0.256, 0.148, 0.139, and 0.123 nm) and those of HCP rings (0.25, 0.15, 0.14, and 0.12 nm) shown in the SAED pattern in **Figure 3.2(b)**. A similar dual phase (Co-rich BCC and Ti-rich HCP) was observed for AlTiCoZn HEA produced via mechanical alloying process [121]. Also, AlCrCuFeNiZn HEA developed by Pradeep et al. [122] via mechanical alloying possessed a Cu-Zn-rich FCC phase similar to this work. In what follows, the thermal degradation behavior of AlTi$_{0.45}$CuZn LHEA is investigated as a function of temperature.

3.3.2 Thermal Stability of NC-AlTi$_{0.45}$CuZn LHEA

3.3.2.1 *DSC/TGA Analyses of NC-AlTi$_{0.45}$CuZn LHEA Reveal Multistep Decomposition*

To understand the decomposition kinetics of the as-milled AlTi$_{0.45}$CuZn LHEA, long-range "50 - 915 °C" DSC and TGA analyses were first conducted at a constant heating rate of 10 K/min. The associated curves within this temperature range are presented in **Figure 3.3(a)**, and it shows that

the alloy went through a multistep decomposition process. One exothermic peak at ~360 °C and endothermic peaks at 750 and 880 °C, respectively, can be observed in the DSC plot; the presence of two endothermic peaks in the DSC curve instead of one peak suggests that the dual-phase-AlTi$_{0.45}$CuZn LHEA is not a eutectic alloy [123]. Furthermore, the TGA plot shows no noticeable weight loss in the sample between the starting temperature of 50 °C and the temperature corresponding to the rising of the first endothermic peak at ~700 °C of the DSC curve. However, ~7.9% weight loss of the sample occurs near the completion of the first endothermic peak, as shown in the TGA plot in **Figure 3.3(a)**. At higher temperatures (>800 °C), i.e., the temperature between the first and second endothermic peaks, a further 17.1% weight loss of the sample occurs.

To determine the kinetics of major microstructural phenomena that set on at the exothermic and endothermic peaks, as-milled powders were annealed before (250 °C) and after (450 °C) the exothermic DSC peak, and just before the first endothermic peak (650 °C) in **Figure 3.3(a)**, for four hours; these samples are hereafter referred to AlTi$_{0.45}$CuZn-250, AlTi$_{0.45}$CuZn-450, and AlTi$_{0.45}$CuZn-650, respectively. The second endothermic peak at 880 °C was not further probed because it occurs at a temperature close to the melting point of AlTi$_{0.45}$CuZn LHEA (845 °C); this endothermic peak therefore corresponds to melting [124]. The XRD patterns of the LHEA as a function of the selected annealing temperatures are presented in **Figure 3.3(b)**. Phase stability occurs in AlTi$_{0.45}$CuZn-250: although the HCP (100) peak found in the as-milled LHEA persists, deconvolution of HCP (101) and FCC (111) peaks occurs (this is clearly seen in the -s-XRD patterns in **Figure 3.7(a)**). For AlTi$_{0.45}$CuZn-450, an additional Al-Ti phase is observed along with the previous HCP (101) and FCC (111) peaks. Finally, AlTi$_{0.45}$CuZn-650 shows the same characteristics as AlTi$_{0.45}$CuZn-450, except that a slight peak shift to the right occurs in AlTi$_{0.45}$CuZn-650. Peak shift to higher 2θ angles is a signature of reduction in lattice parameter

60
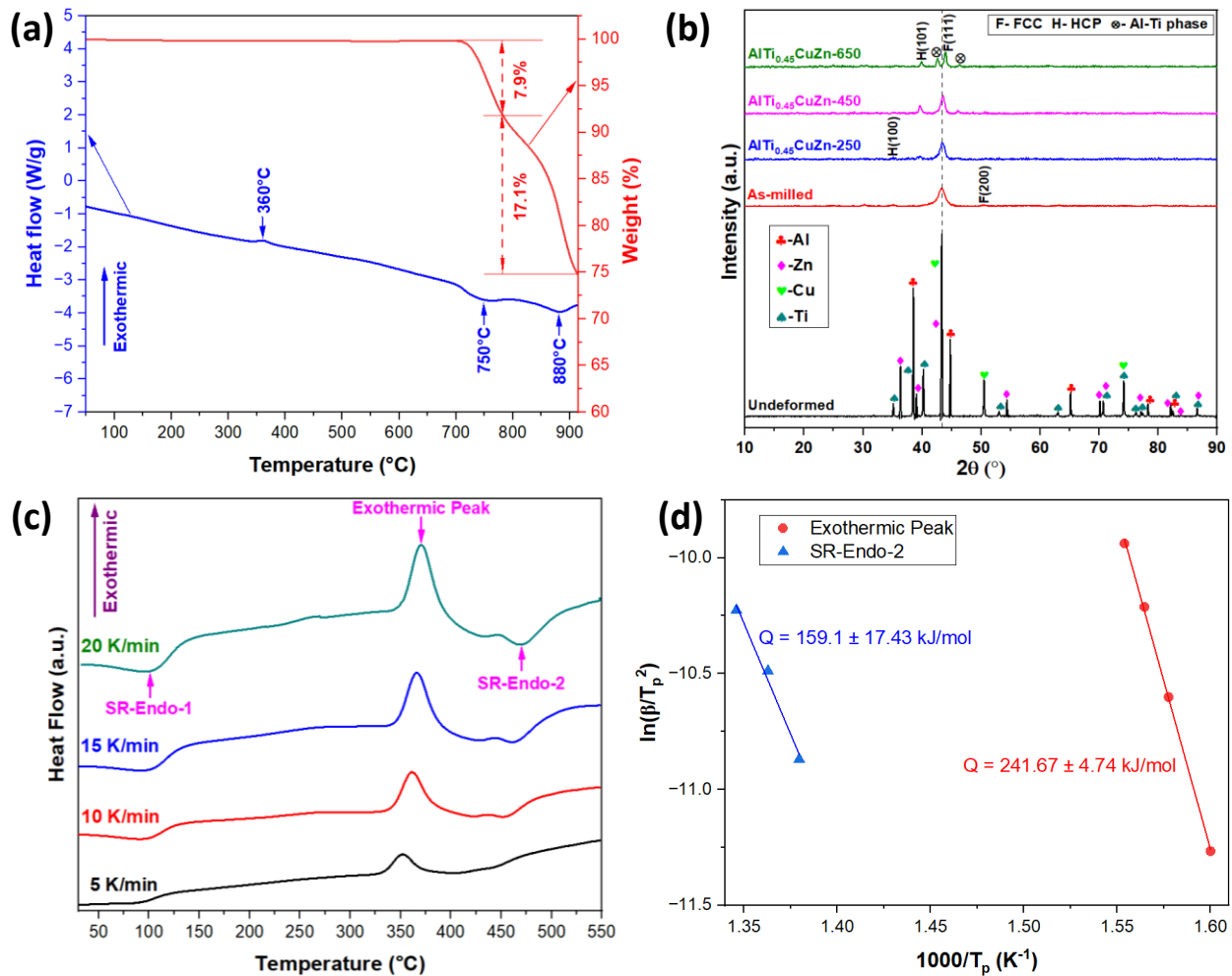
Figure 3.3: (a) Long-range DSC and TGA curves for the as-milled LHEA obtained at 10 K/min heating rate; **(b)** Powder XRD patterns of the undeformed, as-milled, and 250, 450, and 650 °C-annealed samples; **(c)** Short-range DSC curves attained at different heating rates: 5, 10, 15, and 20 K/min; and **(d)** Kissinger plot based on the exothermic and SR-Endo-2 peaks of short-range DSC curves in (c). SR-Endo-1 and SR-Endo-2 in (c) and (d) are the first and second endothermic peaks of the short-range DSC plot, respectively.

[125],[126]. Cataloguing the above observations, we conclude that the phase stability of AlTi$_{0.45}$CuZn LHEA occurs up to a temperature between 250 and 360 °C, while the DSC exothermic peak at 360 °C signifies the occurrence of phase decomposition with no weight loss; this is in agreement with what exothermic peak in DSC curve represents—nanophase precipitation, phase transformation, structure relaxation [123], grain growth [127], formation of new phase (including intermetallic phases) [128,129], release of strain that forms due to mechanical alloying

process [130], and recovery/recrystallization [131]. In other LHEAs in the literature, phase stability occurs up to 400 °C (AlMgSiCrFeNi [9]), 500 °C (AlCoCrFeNi [132]), 900 °C (AlNb$_2$TiV [133]), and 500 °C (AlFeMgNiTi [134]).

As a next step, we focused on the exothermic peak located at 360 °C in the long-range DSC scan to determine the activation energy for phase decomposition: a short-range DSC analysis at 5-20 K/min heating rates within 30-550 °C temperature range was conducted, the result of which is shown in **Figure 3.3(c)**. The exothermic peak of interest in **Figure 3.3(c)** can be found between 350 and 370 °C depending on the heating rate, while two additional endothermic peaks that are not seen in long-range DSC are positioned around 97-102 °C and 452-470 °C, and are referred to SR-Endo-1 and SR-Endo-2, respectively; SR and Endo are short-range and endothermic, respectively. While we posit that the SR-Endo-1 peaks around 100 °C correspond to the energy absorption during the evaporation of residual process control agent [82], the SR-Endo-2 will be discussed later in the manuscript. Using a Kissinger-style analysis in Eqn. (2) [135], the activation energy (Q) for phase decomposition (exothermic peaks in **Figure 3.3(c)**) is determined, as shown in **Figure 3.3(d)**;

$$\frac{d\left(\ln\frac{\beta}{T_p^2}\right)}{d\left(\frac{1}{T_p}\right)} = -\frac{Q}{R} \ldots \ldots \ldots (3.2)$$

where, β is the heating rate, T_P is the absolute peak temperature, and R is the gas constant. Based on the Kissinger plot, the calculated activation energy for the Al-Ti phase formation is 241.67 ± 4.74 kJ/mol. In addition, the corresponding formation enthalpy of the Al-Ti phase is 14.37 J/g at 10 K/min heating rate, as determined by the STAR^e software.

3.3.2.2 S/TEM Analyses of Annealed NC-AlTi$_{0.45}$CuZn LHEA Reveals Zn Evaporation

So far, only the phenomenon that corresponds to the exothermic peak in the DSC plots in **Figures 3.3(a)** and **3.3(c)** is established—*phase decomposition*. It is however not clear which phenomena set on at higher temperatures, especially those that lead to sample weight loss. In what follows, we focus on S/TEM analysis for evaluating nanostructural changes that occur as a function of annealing temperature. The TEM micrographs with the associated SAED patterns and STEM-HAADF/EDS maps for AlTi$_{0.45}$CuZn-250, AlTi$_{0.45}$CuZn-450, and AlTi$_{0.45}$CuZn-650 are shown in **Figure 3.4**. While the TEM micrographs in **Figure 3.4(a)** show homogenous FCC + HCP dual-phase solid-solution structure in AlTi$_{0.45}$CuZn-250, those of AlTi$_{0.45}$CuZn-450 (**Figure 3.4(b)**) and AlTi$_{0.45}$CuZn-650 (**Figure 3.4(c)**) show decomposed regions that reflect as new Al-Ti phase diffraction rings in the inset SAED patterns, in good agreement with the XRD patterns in **Figure 3.3(b)**.

The STEM-HAADF/EDS maps of the LHEA powder shown in **Figure 3.4(d)** confirm the chemical homogeneity in AlTi$_{0.45}$CuZn-250 which is similar to the as-milled sample in **Figure 3.2(e)**. For AlTi$_{0.45}$CuZn-450 in **Figure 3.4(e)**, the occurrence of phase decomposition is confirmed: evolution of Al-Ti-rich region with a darker contrast (indicated by a blue arrow) where Cu and Zn are nearly depleted. However, complex heterogeneous phase structures are observed in the STEM/EDS maps of AlTi$_{0.45}$CuZn-650 in **Figure 3.4(f)**: Al-Ti-, Al-, and Ti-rich regions, as indicated by blue, green, and yellow arrows, respectively. An important observation in **Figure 3.4(f)** is the significant drop in the intensity of Zn compared to those of AlTi$_{0.45}$CuZn-250 (**Figure 3.4(d)**) and AlTi$_{0.45}$CuZn-450 (**Figure 3.4(e)**); this is a signature of Zn *evaporation*. Zn evaporation was reported in AlTiCoZn HEA when annealed at 800 °C [121].
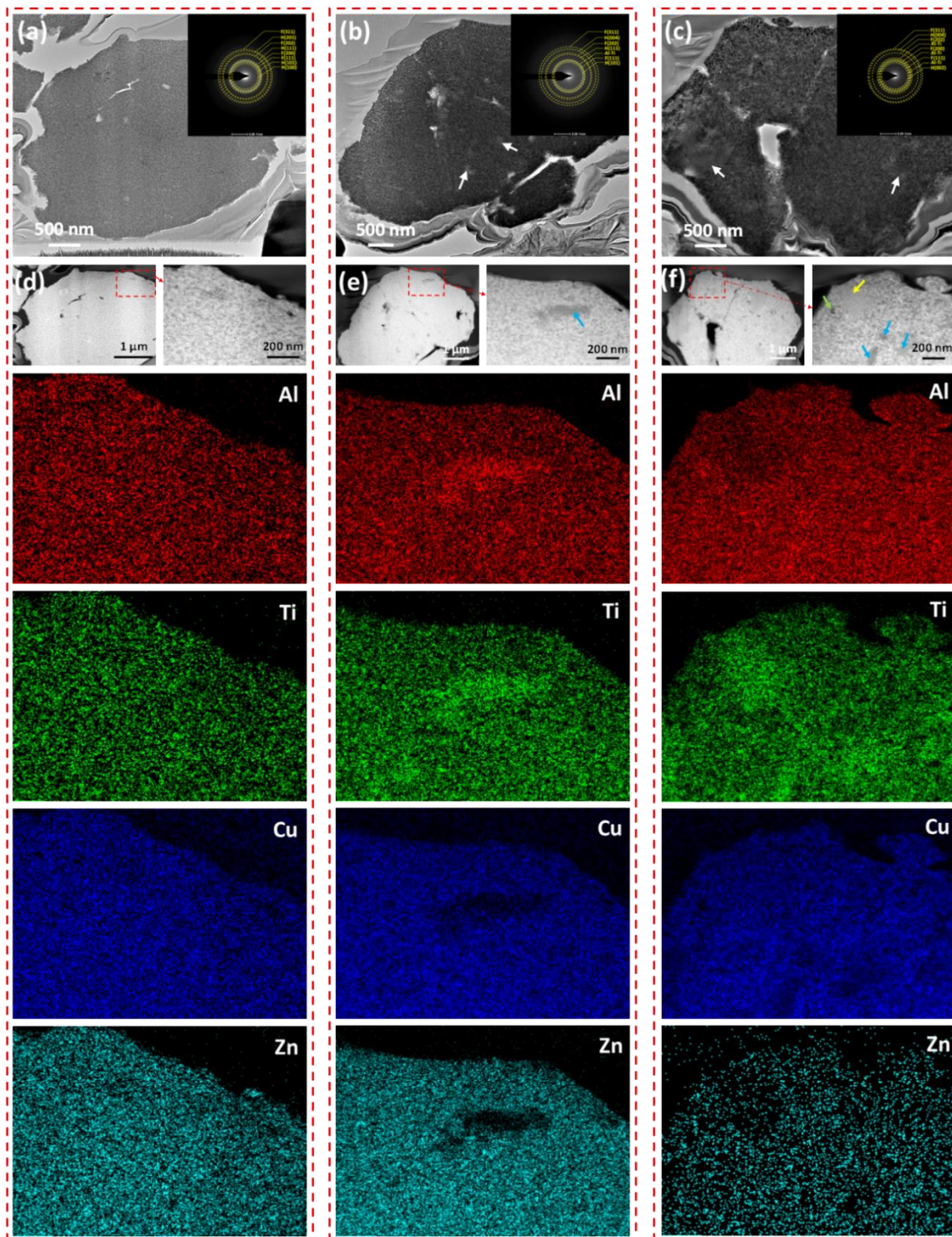
Figure 3.4: TEM micrographs with associated SAED patterns (inset) for the samples annealed at **(a)** 250 °C, **(b)** 450 °C, and **(c)** 650 °C temperatures; and STEM HAADF micrographs with corresponding EDS maps of a lamella cross-section of LHEA particle annealed at **(d)** 250 °C, **(e)** 450 °C, and **(f)** 650 °C temperatures. The white arrows in (b) and (c) indicate decomposed regions. The blue arrows in (e) and (f) indicate the Al-Ti-rich region, while the yellow and green arrows in (f) indicate the Ti- and Al-rich regions, respectively.
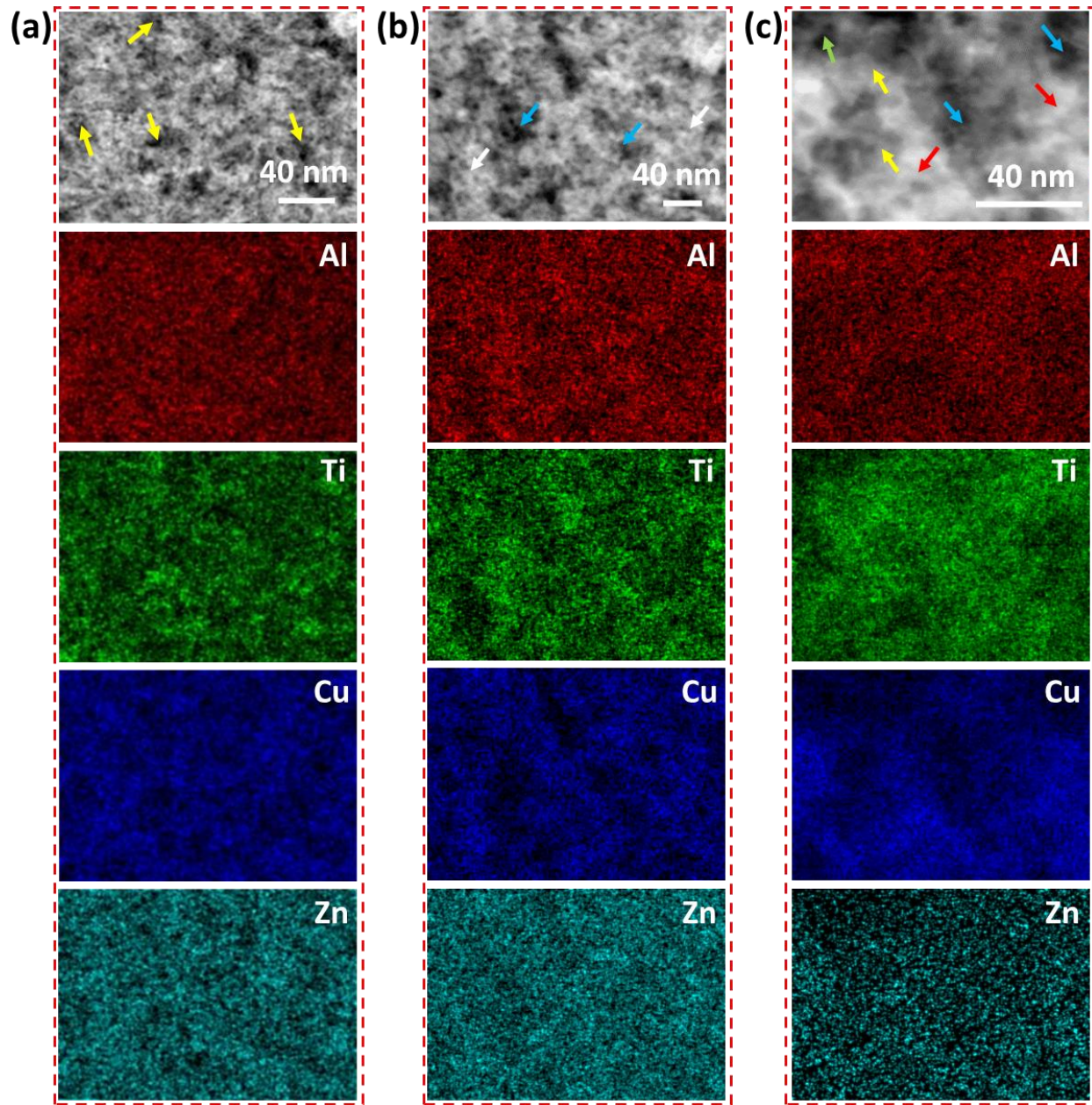
Figure 3.5: High-magnification STEM HAADF micrographs with corresponding EDS maps of a lamella cross-section of LHEA particle annealed at **(a)** 250 °C, **(b)** 450 °C, and **(c)** 650 °C temperatures. The yellow arrows in (a) and (c) indicate the Ti-rich regions, the blue arrows in (b) and (c) indicate the Al-Ti-rich regions, the white arrows in (b) indicate the Cu-Zn-rich regions, and the green and red arrows in (c) indicate the Al- and Cu-rich regions, respectively.

For a better visualization of the phenomena occurring at the nanoscale, high-magnification STEM (HAADF)/EDS maps for each of the annealed samples are presented in **Figure 3.5**. Similar to the as-milled sample (**Figure 3.2(f)**), the nano-sized Ti-rich HCP phase (21 ± 2 nm size) in

65

AlTi$_{0.45}$CuZn-250 can be seen (darker contrast regions marked with yellow arrows) within the bright contrast Cu-Zn-Al rich FCC matrix of the LHEA (**Figure 3.5(a)**). However, in the STEM/EDS map of AlTi$_{0.45}$CuZn-450 in **Figure 3.5(b)**, two separate types of regions can be seen: Al-Ti-rich region with a darker contrast (indicated by blue arrows) and Cu-Zn-rich region with a brighter contrast (indicated by white arrows). This is supported by the STEM/EDS line profile of AlTi$_{0.45}$CuZn-450 sample as shown in **Figure 3.6(a)**. To explain the underlying reasons behind the observed preferential elemental selection during phase decomposition in AlTi$_{0.45}$CuZn-450, the enthalpy of mixing (ΔH_{mix}) for binary elemental pairs that indicate strong interactions between elements [122,136,137] is considered. As can be discerned in **Figure 3.6(b)**, the largest negative ΔH_{mix} value is for Al-Ti for -30 kJ/mol, and it is attributed to the formation of Al-Ti-rich phase.
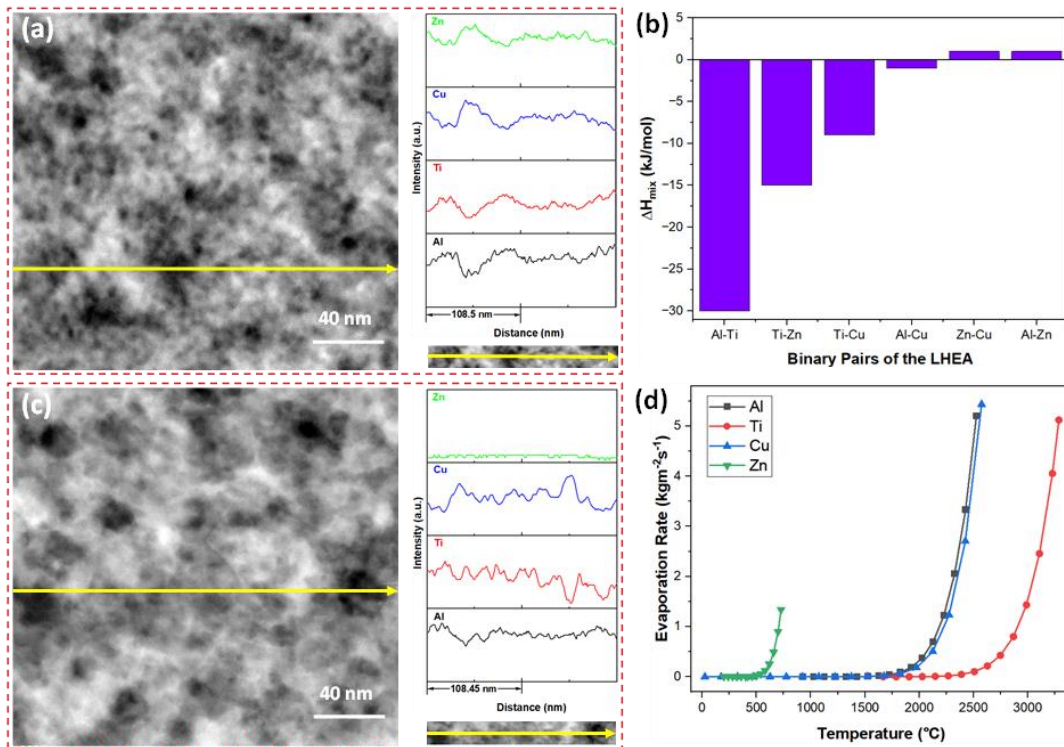
Figure 3.6: (a) STEM/EDS line profile of a lamella cross-section of LHEA particle annealed at 450 °C; **(b)** Enthalpy of mixing (ΔH_{mix}) values for the binary pairs of constituting elements in AlTi$_{0.45}$CuZn LHEA [8]; **(c)** STEM/EDS line profile of a lamella cross-section of LHEA particle annealed at 650 °C; and **(d)** Evaporation rate vs temperature plot for each constituting element of AlTi$_{0.45}$CuZn LHEA.

66

Furthermore, the STEM/EDS maps of AlTi$_{0.45}$CuZn-650 in **Figure 3.5(c)**, show complex Al-Ti, Al-, Ti-, and Cu-rich regions, as identified by blue, green, yellow, and red arrows, respectively. The formation of Al- and Ti-rich phases at elevated temperature may be due to further decomposition of Al-Ti-rich phase formed in AlTi$_{0.45}$CuZn-450; this can be due to the weakening of phase decomposition by atom diffusion and composition homogenization at an elevated temperature [136]. A similar observation (the decomposition of Fe-Cr-rich phases into Fe- and Cr-rich regions) is reported in AlCoCrCuFeNi HEA annealed at 500 °C [136]. In the Cu-rich locations in **Figure 3.5(c)**, Al and Ti concentrations are low, while the intensity of Zn is significantly lower than what is present in AlTi$_{0.45}$CuZn-450 (**Figure 3.5(b)**). This is supported by the STEM/EDS line profile of AlTi$_{0.45}$CuZn-650 in **Figure 3.6(c)**: Zn is almost depleted from the whole sample due to its evaporation, Cu-rich locations are generally low in Ti and Al (despite Al being in nearly uniform concentration across the whole line scan), and Al-Ti-rich phase decomposes to form Al- and Ti-rich regions (Al and Ti signals are no longer in phase or alternating period). Despite the strong Cu signal from the TEM Cu grid that hampers the reliability of elemental composition, attempted quantification of Zn from the STEM/EDS maps in **Figures 3.2(f)** and **3.5** confirms the evaporation and significant loss of Zn from only AlTi$_{0.45}$CuZn-650 sample, as shown in **Figure A1** of **Appendix Section**.

To provide a physical basis for Zn evaporation from AlTi$_{0.45}$CuZn-650, the *evaporation rate* vs. *temperature* plot for each constituting element in AlTi$_{0.45}$CuZn LHEA is shown in **Figure 3.6(d)**. The evaporative flux (J) of an element is dependent on the absolute temperature (T) that can be expressed by Langmuir's equation [138,139]:

$$J = \frac{\lambda p_v}{\sqrt{2\pi M T R_g}} \dots \dots \dots (3.3)$$

where, R_g is the ideal gas constant and M is the molar mass of the evaporating species. λ is a positive constant that considers the portion of the vaporized atoms that inevitably condense at atmospheric pressure; λ is 1 when vaporization sets on under perfect vacuum, but it is taken as 0.1 for the calculation of J in this work by considering that the vaporization happened at 1 atm pressure [139]. p_v is the vapor pressure that can be calculated from the Clausius-Clapeyron equation [138]:

$$\log \bar{p}_v = -\frac{A}{T} + B + C \log T + 10^{-3}DT \dots \dots \dots (3.4)$$

where, the pressure is given in torr, and A, B, C, and D are the constants related to the evaporating species that can be obtained from Ref. [140]. The evaporation rate (in $\text{kgm}^{-2}\text{s}^{-1}$ unit) of each constituting element of $\text{AlTi}_{0.45}\text{CuZn}$ LHEA is the product of its (constituting element's) respective J and M values. It can be observed from **Figure 3.6(d)** that Zn reaches the maximum evaporation rate of 1.34 $\text{kgm}^{-2}\text{s}^{-1}$ at just 727 °C. This is significantly faster than the rest of the elements–Al, Cu, and Ti; they reach their corresponding maximum evaporation rate values of 5.20, 5.44, and 5.12 $\text{kgm}^{-2}\text{s}^{-1}$ at 2527, 2597, and 3287 °C, respectively. The Zn evaporation temperature, 727 °C, is close to the first endothermic peak at 750 °C in the long-range DSC curve, and it supports and explains the Zn evaporation behavior in $\text{AlTi}_{0.45}\text{CuZn}$-650. Because Zn melting precedes evaporation, we also conclude that the SR-Endo-2 peak around 460 °C corresponds to the melting of Zn; Zn melting temperature is 419.7 °C [7].

Based on the XRD, TEM, and STEM/EDS results and analyses, the decomposition stages in DSC/TGA curves in **Figures 3.3(a)** and **3.3(c)** can be completely identified with a greater degree of confidence as further summarized below:

- The *SR-Endo-1 peaks* around 100 °C: they correspond to the energy absorption during the *evaporation* of residual process control agent;

68

- The *only exothermic peak* at around 360 °C in both the short- and long-range DSC plots in **Figures 3.3(a)** and **3.3(c)**: it is attributed to *phase decomposition*—the formation of new Al-Ti phase found in $AlTi_{0.45}CuZn$-450 sample [128,129];

- The *SR-Endo-2 peaks* around 460 °C: they correspond to the *melting of Zn*;

- The *first endothermic peak* at 750 °C in the long-range DSC plot: it indicates the onset of *Zn evaporation* from the LHEA [141], and the corresponding weight loss of 7.9% in the TGA curve shown in **Figure 3.3(a)**.

- The *second endothermic peak* at 880 °C (**Figure 3.3(a)**) indicates the melting of LHEA [124]; this is because the theoretical melting temperature of the $AlTi_{0.45}CuZn$ LHEA is 845 °C. The further weight loss of about 17.1% can be due to further evaporation of Zn from the LHEA sample.

Based on the Kissinger plot in **Figure 3.3(d)**, the calculated activation energies for Zn melting is 159.1 ± 17.43 kJ/mol (SR-Endo-2 peak). Moreover, according to the $STAR^e$ software, the enthalpies for the melting of Zn, evaporation of Zn, and melting of LHEA are -1.4, -101.2, -66.1 J/g, respectively, at 10 K/min heating rate. As a next step, we analyze and evaluate the as-milled and annealed LHEA samples' synchrotron XRD results to determine their crystal structure, grain size, and lattice strain at a higher resolution, and PDF results to evaluate their local atomic arrangements.

3.3.3   Synchrotron-based XRD and PDF Analysis

3.3.3.1   Lattice strain and sluggish grain growth revealed by s-XRD

Figure 3.7(a) shows the s-XRD patterns of the as-milled and annealed samples, where the peak positions are shown in terms of scattering vector, q ($q = 4\pi\lambda^{-1}\sin\theta$, where θ is half of the scattering

angle, and $\lambda = 0.1818$ Å is the X-ray wavelength) [142]. Although the s-XRD patterns are mostly in good agreement with the XRD patterns shown in **Figures 3.1(a)** and **3.3(b)**, additional peaks are observed in the s-XRD patterns that match well with the SAED patterns shown in **Figures 3.2(b)** and **3.4(a-c)**. The s-XRD analysis also confirms an FCC + HCP dual-phase solid-solution structure of the as-milled sample. Notable observations from the s-XRD pattern for $AlTi_{0.45}CuZn$-250 are the deconvolution of HCP (101) and FCC (111) peaks and the minor Al-Ti phase peaks that are not clearly discernible in the tabletop XRD (**Figure 3.3(b)**) and TEM-SAED (**Figure 3.4(a)**) patterns; this underscores the high-resolution capability of the s-XRD technique. Using FullProf package (integrated with Match 3! software) for Rietveld refinement analysis as shown in **Figure A2** of **Appendix Section**, FCC phase in $AlTi_{0.45}CuZn$-250 has a lattice parameter of $a = 3.5819$ Å, while the HCP phase's lattice parameters are $a = 2.7716$ Å and $c = 4.7129$ Å. The comparison of the s-XRD patterns for $AlTi_{0.45}CuZn$-450 and $AlTi_{0.45}CuZn$-650 shows that additional Al-Ti phase appears and the peaks shift slightly to the right—an indication of reduced lattice parameter due to annealing [125] and the release of internal stresses [126]. This peak shift to the right (lattice parameter reduction) can also be associated with the evaporation of Zn from the $AlTi_{0.45}CuZn$ lattice. Finally, the pronounced diffraction intensity in **Figure 3.7(a)** with the higher annealing temperatures is due to the release of internal energy and coarsening of the crystal during the annealing process [143].

Figure 3.7(b) is the grain size calculated using Scherrer equation and lattice strain estimated from Williamson-Hall equations plots for as-milled, $AlTi_{0.45}CuZn$-250, and $AlTi_{0.45}CuZn$-450 samples; they were obtained from the s-XRD patterns in **Figure 3.7(a)**, and only the FCC (111) and HCP (110) peaks are considered. Also, the grain size and lattice strain are not calculated for $AlTi_{0.45}CuZn$-650 due to the severe Zn evaporation that occurs in that sample. Considering the

70

FCC (111) peak, the grain sizes of the as-milled (0.27 T_m), AlTi$_{0.45}$CuZn-250 (0.47 T_m), and AlTi$_{0.45}$CuZn-450 (0.65 T_m) samples were determined as ~4, ~7, and ~9 nm, respectively, which are close to the grain sizes obtained from the XRD patterns (**Figure 3.1(a)** and **3.3(b)**) of the same samples: ~6, ~9, and ~11 nm, respectively. For the HCP phase, considering the HCP (110) peak, the grain sizes of the aforementioned samples are ~7, ~8, and ~9 nm, respectively. It is well-known that grain growth—a decrease in the total grain boundary area—sets on during the post-processing of nanocrystalline metal powders (e.g., sintering) due to the presence of a thermodynamic driving force—excess GB energy [144]. The grain growth behavior of mechanically alloyed nanocrystalline HEAs during different annealing temperatures has been well-investigated: grain size in as-milled Al$_{20}$Li$_{20}$Mg$_{10}$Sc$_{20}$Ti$_{30}$ (0.23 T_m) [49], CoCrFeNiMn$_{0.5}$Ti$_{0.5}$ (0.16 T_m) [145], and AlTiV$_{0.5}$CrMo (0.15 T_m) [112] LHEAs increased from 12 to 26 nm, 14 to ~50 nm, and 8 to 51.4 nm after annealing them at 500 (0.59 T_m; 1 hr), 700 (0.53 T_m; 1 hr), and 800 (0.53 T_m; 0.5 hr) °C, respectively. The growth rate for the alloy under investigation is interestingly sluggish considering the starting grain size is on the lower end of a nanoscale (grain boundary mobility is typically high for finer grain size [146]) and the annealing temperatures (0.47 T_m-0.65 T_m) are above the temperature where rapid grain coarsening is expected in traditional alloys.
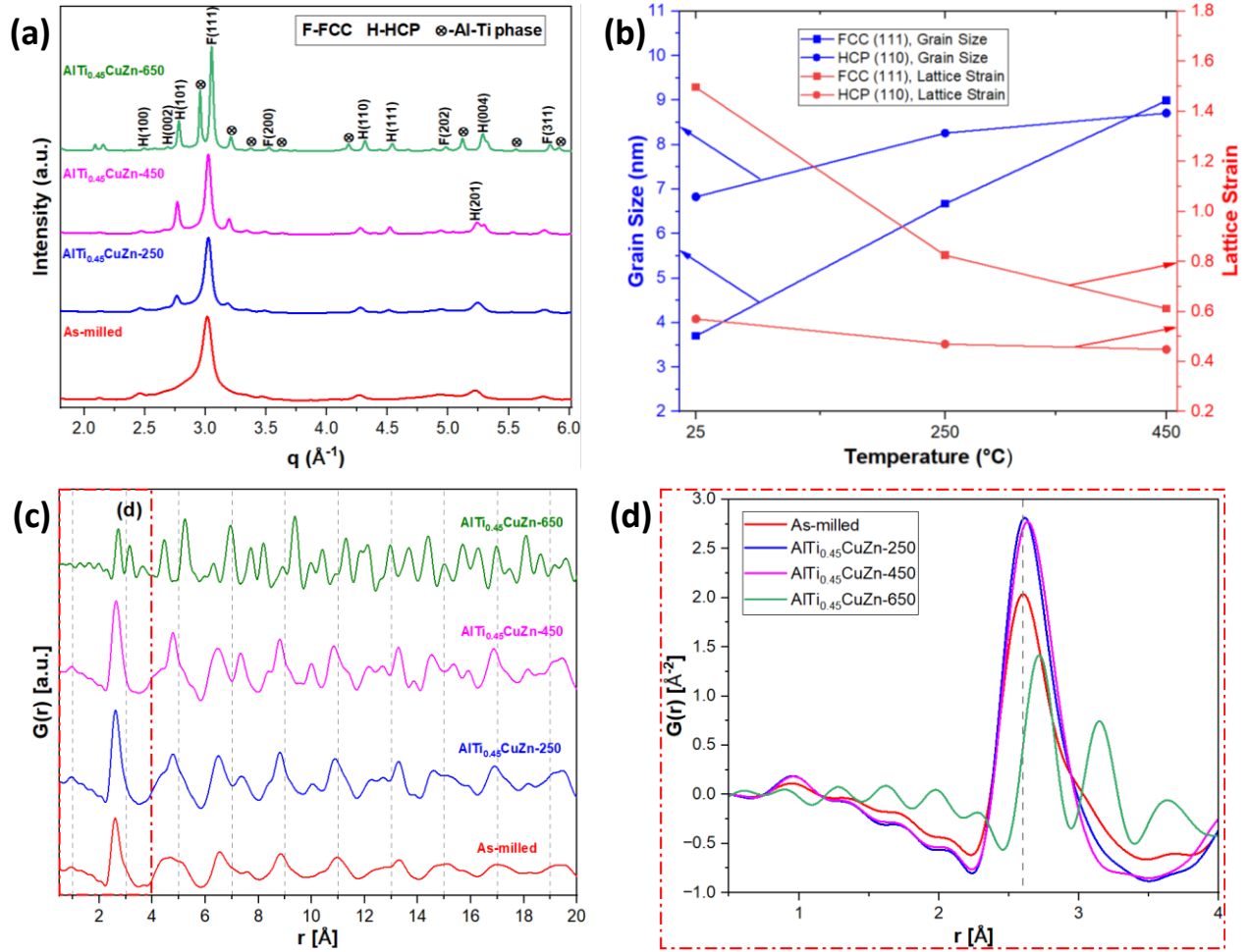
Figure 3.7: (a) s-XRD patterns of the as-milled and annealed samples; **(b)** Grain size and lattice strain plots obtained from the s-XRD patterns of (a); and PDF profiles with **(c)** $r = 0.5$ to 20 Å and **(d)** $r = 0.5$ to 4 Å for the as-milled and annealed samples. The as-milled sample in (b) is indicated by 25 °C room temperature.

Generally, grain size increases (from the as-milled) as the annealing temperature increases, but the opposite holds for lattice strain as shown in **Figure 3.7(b)**. During the mechanical alloying process, dislocation density and lattice strain in the alloy greatly increase via severe plastic deformation [23,147]. This lattice strain is reduced during the annealing of the as-milled alloy because of the decrease in internal strain and density of lattice defects [148]. In **Figure 3.7(b)**, there is a significant drop in lattice strain between the as-milled and AlTi$_{0.45}$CuZn-250 samples, and the

lattice strain declines at a slower rate at higher temperatures; similar behavior was previously reported elsewhere [144].

3.3.3.2 Local atomic arrangement revealed by PDF

For further insight into the local atomic arrangement of the as-milled and annealed samples, the PDF profiles from $r = 0.5$ to 20 Å are plotted and shown in **Figure 3.7(c)**, where $G(r)$ is the reduced pair distribution function. The PDF profiles contain diffuse scattering that explains local changes in the crystal structure, and the probability of finding a pair of atoms upon a distance (r) and local information surrounding each atom [149]. The peak positions in the PDF profiles provide information on the interatomic distances, whereas the peak widths and peak areas provide information on the atomic thermal vibrations (along with accumulated disorder) and co-ordination numbers, respectively [150]. In **Figure 3.7(c)**, significant differences in the PDF profile of $AlTi_{0.45}CuZn$-650 as compared to as-milled, $AlTi_{0.45}CuZn$-250, and $AlTi_{0.45}CuZn$-450 samples can be noticed, and to further probe this departure, PDF profiles between $r = 0.5$ to 4 Å of each sample are provided in **Figure 3.7(d)**. To correlate the lengths of different bonds possible for the constituent elements with the peak positions in **Figure 3.7(d)**, the bond lengths between different binary pairs are collected from literature along with the sum of atomic radii (of both elements of the binary pair) as shown in **Table 3.1**. We can observe from **Table 3.1** that the sum of atomic radii of both elements of each binary pair is close to the previously reported bond length values of the binary pair which indicates the applicability of these bond length values. Clearly, the bond length ranges between 2.5 and 3.1 Å, and that also informs the selected range of r (from 0.5 to 4 Å) in the PDF profiles in **Figure 3.7(d)**.

Table 3.1: The lengths of bonds between different constituent elements of $AlTi_{0.45}CuZn$.

| Atomic Bond	Bond Length (Å)	Sum of Atomic Radii (Å) [7]
Al-Ti	2.90-2.91 [151], 2.83 [152]	2.89
Al-Cu	2.63 [153], 2.73 [154]	2.71
Al-Zn	2.59 [155]	2.82
Cu-Ti	2.73 [154]	2.74
Cu-Zn	2.53-2.83 [156]	2.67
Zn-Ti	3.02 [157]	2.85

The first major peak is observed at 2.62 Å for as-milled, $AlTi_{0.45}CuZn$-250, and $AlTi_{0.45}CuZn$-450 samples in **Figure 3.7(d)**; however, the peak for the as-milled sample has lower intensity and different width compared to those of $AlTi_{0.45}CuZn$-250 and $AlTi_{0.45}CuZn$-450. Also, it can be noticed that the major peak is slightly shifted to the right (from the as-milled) as the annealing temperature increases up to 450 °C. The variation in peak width and shift in peak position for different samples can be attributed to the change in local lattice strain due to annealing which can also be confirmed in **Figure 3.7(b)** [149]. Because of the closeness in bond length, the first major peak at 2.62 Å can correspond to Al-Cu, Cu-Zn, and/or Al-Zn bonds for as-milled, $AlTi_{0.45}CuZn$-250, and $AlTi_{0.45}CuZn$-450 samples, as shown in **Table 3.1**. But for $AlTi_{0.45}CuZn$-650, the first major peak is found at 2.71 Å, thus there is a shift in peak position, which is accompanied by lower peak width and intensity compared to the rest of the samples. This peak could also correspond to Al-Cu, Cu-Zn, or Cu-Ti bonds for $AlTi_{0.45}CuZn$-650 based in **Table 3.1**. Because of the significant evaporation of Zn in $AlTi_{0.45}CuZn$-650 (**Figures 3.3-3.6**), the Cu-Zn bond cannot be dominant, hence the major peak at 2.71 Å may correspond to either Al-Cu or Cu-Ti bond or both. Meanwhile, additional peaks are observed in the PDF profile of $AlTi_{0.45}CuZn$-650 at 3.15 and 3.64 Å, which

are absent in other annealed samples. Although the exact bond type is not clear for these two new peaks, they may be related to the Al- and Ti- rich regions (both elements have the highest atomic radius) that decompose from Al-Ti phase. In what follows, we evaluate and discuss the nano-mechanical performance of the as-milled and annealed but stable $AlTi_{0.45}CuZn$ LHEA— $AlTi_{0.45}CuZn$-250 via nano-indentation experiments.

3.3.4 Mechanical Properties of the As-milled and $AlTi_{0.45}CuZn$-250 LHEA

The nano-indentation results provide a load-displacement response at the nanometre level to determine the mechanical properties of the micro-zone with good accuracy [158]. **Figure 3.8(a)** shows the representative load-displacement curves for as-milled and $AlTi_{0.45}CuZn$-250 samples. The average hardness values of as-milled and $AlTi_{0.45}CuZn$-250 samples are 7.50 ± 0.1 and 8.58 ± 0.4 GPa, respectively; these hardness values indicate the resistance of materials against elastic deformation [158]. The hardness is contingent upon other mechanical properties, including ductility, strength, and elastic stiffness [159]. A linearly proportional relationship between the nano-hardness and yield strength of the material has already been developed, but the indentation depth needs to be considered in such relation [160]. According to **Figure 3.7(b)**, the grain size of $AlTi_{0.45}CuZn$-250 is larger than that of the as-milled sample, but both of their grain sizes are under 10 nm; hence, based on the "inverse Hall-Petch relationship", the strength of materials can decline with the reduction in grain size [161]. This softening can occur due to grain boundary-mediated deformation mechanisms in NC materials–grain boundary sliding, rotation, and migration [162], and it can be responsible for the lower hardness values recorded for the as-milled sample compared to the $AlTi_{0.45}CuZn$-250. Similarly, since the average grain sizes of the as-milled and $AlTi_{0.45}CuZn$-250 are relatively close, and the change in grain size can in fact be negligible, it is possible that the increase in hardness after annealing at 250 °C could be attributed to *grain*

75
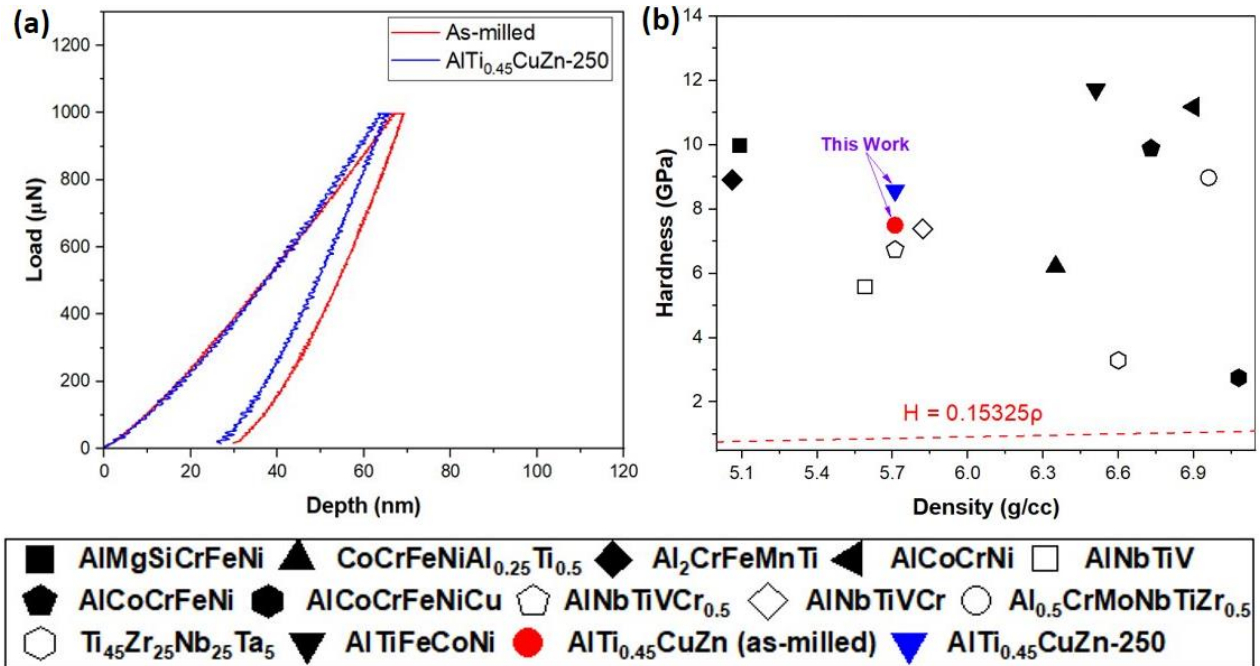
Figure 3.8: (a) Representative load-displacement curves of as-milled and 250 °C-annealed samples; and **(b)** Comparison of the hardness values of as-milled and 250 °C-annealed samples with other previously reported LHEAs for which nanoindentation tests were carried out. These other LHEAs are: AlMgSiCrFeNi (mechanical alloying + spark plasma sintering) [9], $Al_{0.5}CrMoNbTiZr_{0.5}$ (BCC phase; arc melting) [10], $CoCrFeNiAl_{0.25}Ti_{0.5}$ (mechanical alloying + sintering) [11], $Al_2CrFeMnTi$ (BCC phase; mechanical alloying + casting) [12], AlCoCrNi and AlCoCrFeNi (arc melting) [13], AlCoCrFeNiCu (laser metal deposition) [14], AlNbTiV, $AlNbTiVCr_{0.5}$, and AlNbTiVCr (vacuum-levitation) [15], $Ti_{45}Zr_{25}Nb_{25}Ta_5$ (arc melting) [16], and AlTiFeCoNi (arc melting + high-pressure torsion) [17]. Traditional alloys' data were collected from *Ansys Granta EduPack 2022 R1* software to establish the $H = 0.15325\rho$ relation represented by the red dashed line. The open symbols indicate refractory LHEAs.

boundary relaxation—a low-temperature process in which highly defective nonequilibrium grain boundaries evolve into a more equilibrated structures by annihilation of excess defects during annealing [163]. The grain boundary relaxation phenomenon in this alloy will require a more detailed study in our future work.

The nano-indentation values of the as-milled and $AlTi_{0.45}CuZn$-250 samples in comparison with those reported for other LHEAs are presented in **Figure 3.8(b)**; the densities of the alloys were either taken from literature or theoretically calculated following the method described in Ref. [7].

While nano-indentation values for all LHEAs are higher than the traditional alloys (represented by a slope of hardness-density ($H - \rho$); data extracted from Ref. [164]), it is apparent that all LHEAs have superior hardness values in the density range evaluated. More interesting is that both as-milled and AlTi$_{0.45}$CuZn-250 samples have superior hardness values when compared to the refractory LHEAs near their density range ($5.55 \leq \rho \leq 5.85$ g/cc). While refractory LHEAs are expected to possess higher hardness values, the excellent hardness values of both as-milled and AlTi$_{0.45}$CuZn-250 samples could be attributed to the grain size effect and HCP phase strengthening of the FCC matrix phase, similar to previous works [47,65,114]. Cataloguing all the observations in this study, this work shows the potential use of AlTi$_{0.45}$CuZn LHEA for lightweight structural applications even at elevated temperatures, and grain refinement to the nanoscale could improve its technological benefits.

3.4   Summary and Conclusion

Al-based traditional lightweight alloys have widespread structural applications, but their mechanical properties and phase stability become significantly degraded at elevated temperatures. In this work, we evaluate the thermal degradation of a novel Al-containing dual-phase LHEA (AlTi$_{0.45}$CuZn) using multi-modal characterization techniques—differential scanning calorimetry/thermogravimetric analysis, scanning/transmission electron microscopy, and synchrotron X-ray diffraction/pair distribution function. The following conclusions can be drawn from this study:

I.   Phase stability of AlTi$_{0.45}$CuZn LHEA is observed up to a temperature below 360 °C, at and above which multistep decomposition sets on. The multistep decomposition involves;

   a.   *phase decomposition* at ~360 °C—the formation of new Al-Ti phase

b. *melting of Zn* at ~460 °C;

c. *evaporation of Zn* and 7.9% LHEA weight loss at ~750 °C; and

d. *melting of LHEA* at 880 °C; this is accompanied by further 17.1% weight loss.

II. The observed preferential elemental selection of Al and Ti during phase decomposition in AlTi$_{0.45}$CuZn is due to the largest negative ΔH_{mix} value for Al-Ti (-30 kJ/mol) that promotes strong interactions between them compared to other binary elemental pairs (Al-Zn—1 kJ/mol, Al-Cu—-1 kJ/mol, Ti-Zn—-15 kJ/mol, Ti-Cu—-9 kJ/mol, and Zn-Cu—1 kJ/mol).

III. The evaporation of Zn from AlTi$_{0.45}$CuZn LHEA is due to its faster evaporation rate of 1.34 kgm^{-2}s^{-1} that occurs at just 727 °C. This is significantly faster compared to other constituent elements—Al (5.20 kgm^{-2}s^{-1} at 2527 °C), Cu (5.44 kgm^{-2}s^{-1} at 2597 °C), and Ti (5.12 kgm^{-2}s^{-1} at 3287 °C).

IV. The observations noted here are supported by high-resolution s-XRD and PDF results; more so, they reveal local atomic arrangements (co-dominant Al-Cu, Cu-Zn, or Al-Zn bonds in as-milled, AlTi$_{0.45}$CuZn-250, and AlTi$_{0.45}$CuZn-450), local strain, and sluggish grain growth in the dual-phase AlTi$_{0.45}$CuZn LHEA.

V. AlTi$_{0.45}$CuZn-250 (8.58 ± 0.4 GPa) shows higher nano-indentation hardness value than the as-milled sample (7.50 ± 0.1 GPa), yet both samples outperform other LHEAs of the same density range of $5.55 \leq \rho \leq 5.85$ g/cc.

In pursuit of the use of LHEAs for lightweight applications, this study critically evaluates the thermal degradation patterns in a novel dual (FCC + HCP) phase AlTi$_{0.45}$CuZn LHEA that is a model for other LHEAs. By extension to other LHEAs, the possible evaporation of constituent

LHEA elements during degradation, as observed in the present study, points to careful elemental selection that can be tacitly made to delay degradation at elevated temperatures. It is encouraging for the HEA community though that the observation in this study points to the potential use of $AlTi_{0.45}CuZn$ LHEA for lightweight structural applications even at substantially elevated temperatures, and grain refinement to the nanoscale could contribute to its technological benefits.

Chapter 4: Conclusions and Future Works

4.1   Conclusions

This thesis reports findings on newly designed, developed, and examined AlTiCuZn-based LHEAs for potential structural applications. Because intermetallic (IM) compounds are mostly deleterious and achieving solid-solution (SS) is highly desirable in HEAs design, the accuracy of the classical empirical phase stability rules that predict SS formation and crystal structure in HEAs was first systematically examined. To probe into the effectiveness of these rules, an existing AlCoCrFe alloy for benchmarking and five novel AlTiCuZn-based quaternary semi-equiatomic LHEAs ($Al_{0.57}TiCuZn$, $AlTi_{0.45}CuZn$, $Al_{0.45}TiCuZn$, $AlTiCu_{1.76}Zn$, and $AlTiCu_2Zn$) were produced and characterized. While the experimentally developed AlCoCrFe possesses a BCC SS structure that correctly follows the classical phase stability rules, violation of these rules can be observed in AlTiCuZn-based LHEAs. Subsequently, all AlTiCuZn-based LHEAs predicted by the classical empirical rules to possess a single-phase FCC SS structure fail when experimentally developed, except $AlTi_{0.45}CuZn$ which shows SS albeit with FCC + HCP dual phase structure, breaking the VEC rule. Using $AlTi_{0.45}CuZn$ as a guide, a more conservative criteria are proposed for AlTiCuZn-based LHEAs: for SS—$\Omega \geq 1.6$, $\delta \leq 5\%$, and $\Delta H_{mix} \geq -8$ kJ/mol; and for dual-phase FCC + HCP structure—VEC range is $7.5 \leq VEC \leq 8.4$. Novel non-equiatomic $AlTi_{0.37}CuZn_{0.97}$ and $AlTi_{0.56}Cu_{1.24}Zn_{1.2}$ LHEAs that validate these revised rules are further developed. These findings affirm that the breakdown of phase stability rules can be alloy-specific, and the microstructure of AlTiCuZn-based LHEAs can be greatly influenced by good chemical compatibility among the constituent elements.

Subsequently, the thermal deteriorative behavior and mechanical properties of novel Al-containing FCC + HCP-structured $AlTi_{0.45}CuZn$ LHEA is probed to assess its potential in structural applications where they can be exposed to elevated temperatures. Based on the results from multi-modal DSC/TGA, STEM/EDS, and s-XRD/PDF analyses, the thermal phase stability limit of $AlTi_{0.45}CuZn$ is observed between 250 and 360 °C. Multistep decomposition occurs beyond this phase stability limit, which includes:

- At ~360 °C: *phase decomposition*, resulting in new Al-Ti phase formation
- At ~460 °C: *Zn melting*
- At ~750 °C: *Zn evaporation,* accompanied by 7.9% weight loss
- At 880 °C: *LHEA melting,* accompanied by a further 17.1% weight loss.

During *phase decomposition*, Al-Ti phase forms off the $AlTi_{0.45}CuZn$ matrix due to the largest negative ΔH_{mix} value for Al-Ti (-30 kJ/mol) than other binary pairs, which favours stronger interactions between Al and Ti. Zn *evaporation* from $AlTi_{0.45}CuZn$ is attributed to its rapid evaporation rate of 1.34 $kgm^{-2}s^{-1}$ occurring at just 727 °C, which is more rapid than other constituent elements. Besides the confirmation of the aforementioned observations, high-resolution synchrotron-XRD and PDF results demonstrate local atomic arrangements, local strain, and slow grain growth in $AlTi_{0.45}CuZn$. Owing to the combined grain size effect and HCP phase strengthening of the FCC matrix, as-milled and $AlTi_{0.45}CuZn$-250 samples show excellent nano-indentation hardness values of ~7.50 and ~8.58 GPa, respectively, thus outperforming other LHEAs with similar density. In the end, the thermal degradation behavior observed for FCC + HCP-structured $AlTi_{0.45}CuZn$ LHEA can be a model in the design of other LHEAs—to circumvent thermal degradation by *phase decomposition* and elemental *evaporation* via the careful selection of constituent elements that inhibit both phenomena.

4.2 Future Works

This thesis demonstrates the technological advantages of novel nanocrystalline $AlTi_{0.45}CuZn$ LHEA for possible lightweight structural applications, even at substantially elevated temperatures. To gain more insight into the mechanical properties of $AlTi_{0.45}CuZn$ LHEA for successful transitioning to industry for scaling and commercialization in the future, the following next steps are recommended to be explored:

- The change in the lattice parameter of $AlTi_{0.45}CuZn$ LHEA as a function of annealing temperature should be extensively investigated based on s-XRD results.

- This thesis examined the nano-indentation hardness of $AlTi_{0.45}CuZn$ LHEA at only one loading condition; examination of hardness behavior under different loading conditions would be of significant interest.

- Grain-boundary relaxation phenomenon in $AlTi_{0.45}CuZn$ LHEA should be investigated at temperatures less than 250 °C to examine the hardening effect caused by the relaxation of non-equilibrium grain boundaries.

- The newly-developed $AlTi_{0.45}CuZn$ LHEA was produced using a powder processing route, and by extension, conventional consolidation method is high-temperature sintering that can significantly deteriorate the mechanical properties of the alloy. To circumvent this problem, a solid-state cold spray additive manufacturing process can be used to consolidate nanocrystalline LHEA into "bulk form". The mechanical and tribological properties of the bulk LHEA can be further investigated at different stain rate/loading conditions.

References

[1]   Y. Zhang, History of High-Entropy Materials, in: High-Entropy Mater., 1st ed., Springer Singapore, Singapore, 2019: pp. 1–31. https://doi.org/10.1007/978-981-13-8526-1.

[2]   W. Zhang, P.K. Liaw, Y. Zhang, Science and technology in high-entropy alloys, Sci. China Mater. 61 (2018) 2–22. https://doi.org/10.1007/s40843-017-9195-8.

[3]   Y. Zhang, Y.J. Zhou, J.P. Lin, G.L. Chen, P.K. Liaw, Solid-Solution Phase Formation Rules for Multi-component Alloys, Adv. Eng. Mater. 10 (2008) 534–538. https://doi.org/10.1002/adem.200700240.

[4]   J.-W. Yeh, S.-K. Chen, S.-J. Lin, J.-Y. Gan, T.-S. Chin, T.-T. Shun, C.-H. Tsau, S.-Y. Chang, Nanostructured High-Entropy Alloys with Multiple Principal Elements: Novel Alloy Design Concepts and Outcomes, Adv. Eng. Mater. 6 (2004) 299–303. https://doi.org/10.1002/adem.200300567.

[5]   W. Li, D. Xie, D. Li, Y. Zhang, Y. Gao, P.K. Liaw, Mechanical behavior of high-entropy alloys, Prog. Mater. Sci. 118 (2021) 100777. https://doi.org/10.1016/j.pmatsci.2021.100777.

[6]   D.B. Miracle, O.N. Senkov, A critical review of high entropy alloys and related concepts, Acta Mater. 122 (2017) 448–511. https://doi.org/10.1016/j.actamat.2016.08.081.

[7]   I. Alam, M.A. Adaan-Nyiak, A.A. Tiamiyu, Revisiting the phase stability rules in the design of high-entropy alloys: A case study of quaternary alloys produced by mechanical alloying, Intermetallics. 159 (2023) 107919. https://doi.org/10.1016/j.intermet.2023.107919.

[8]   A. Takeuchi, A. Inoue, Classification of Bulk Metallic Glasses by Atomic Size

Difference, Heat of Mixing and Period of Constituent Elements and Its Application to

Characterization of the Main Alloying Element, Mater. Trans. 46 (2005) 2817–2829.

https://doi.org/10.2320/matertrans.46.2817.

[9]   N. Singh, Y. Shadangi, V. Shivam, N.K. Mukhopadhyay, MgAlSiCrFeNi low-density

high entropy alloy processed by mechanical alloying and spark plasma sintering: Effect on

phase evolution and thermal stability, J. Alloys Compd. 875 (2021) 159923.

https://doi.org/10.1016/j.jallcom.2021.159923.

[10]   O.A. Waseem, H.J. Ryu, Combinatorial development of the low-density high-entropy

alloy Al10Cr20Mo20Nb20Ti20Zr10 having gigapascal strength at 1000 °C, J. Alloys

Compd. 845 (2020) 155700. https://doi.org/10.1016/j.jallcom.2020.155700.

[11]   A. Erdogan, A. Günen, M.S. Gök, S. Zeytin, Microstructure and mechanical properties of

borided CoCrFeNiAl0.25Ti0.5 high entropy alloy produced by powder metallurgy,

Vacuum. 183 (2021) 109820. https://doi.org/10.1016/j.vacuum.2020.109820.

[12]   H. Jahangiri, S. Mohagheghi, A. Asghari Alamdari, R. Yilmaz, K. Gürcan Bayrak, F. Yu,

H. Ghadbeigi, E. Ayas, A. Motallebzadeh, Microstructure development and mechanical

performance of Al2CrFeMnTi light-weight high entropy alloy, Intermetallics. 139 (2021)

107376. https://doi.org/10.1016/j.intermet.2021.107376.

[13]   E. Jumaev, S.H. Hong, J.T. Kim, H.J. Park, Y.S. Kim, S.C. Mun, J.-Y. Park, G. Song, J.K.

Lee, B.H. Min, T. Lee, K.B. Kim, Chemical evolution-induced strengthening on

AlCoCrNi dual-phase high-entropy alloy with high specific strength, J. Alloys Compd.

777 (2019) 828–834. https://doi.org/10.1016/j.jallcom.2018.11.057.

[14] M. Dada, P. Popoola, N. Mathe, S. Adeosun, S. Pityana, Investigating the elastic modulus and hardness properties of a high entropy alloy coating using nanoindentation, Int. J. Light. Mater. Manuf. 4 (2021) 339–345. https://doi.org/10.1016/j.ijlmm.2021.04.002.

[15] G. Ge, F. Chen, X. Tang, Y. Wang, C. Li, Irradiation damage versus lattice distortion in AlNbTiVCrx (x = 0, 0.5, 1) high-entropy alloys from first-principles calculations and irradiation experiments, J. Nucl. Mater. 563 (2022) 153630. https://doi.org/10.1016/j.jnucmat.2022.153630.

[16] V.T. Nguyen, M. Qian, Z. Shi, T. Song, L. Huang, J. Zou, Compositional design of strong and ductile (tensile) Ti-Zr-Nb-Ta medium entropy alloys (MEAs) using the atomic mismatch approach, Mater. Sci. Eng. A. 742 (2019) 762–772. https://doi.org/10.1016/j.msea.2018.11.054.

[17] P. Edalati, R. Floriano, Y. Tang, A. Mohammadi, K.D. Pereira, A.D. Luchessi, K. Edalati, Ultrahigh hardness and biocompatibility of high-entropy alloy TiAlFeCoNi processed by high-pressure torsion, Mater. Sci. Eng. C. 112 (2020) 110908. https://doi.org/10.1016/j.msec.2020.110908.

[18] S.O. Poulsen, P.W. Voorhees, Early stage phase separation in ternary alloys: A test of continuum simulations, Acta Mater. 113 (2016) 98–108. https://doi.org/10.1016/j.actamat.2016.04.054.

[19] E.P. George, D. Raabe, R.O. Ritchie, High-entropy alloys, Nat. Rev. Mater. 4 (2019) 515–534. https://doi.org/10.1038/s41578-019-0121-4.

[20] M.H. Tsai, J.W. Yeh, High-entropy alloys: A critical review, Mater. Res. Lett. 2 (2014) 107–123. https://doi.org/10.1080/21663831.2014.912690.

[21] Y.F. Ye, Q. Wang, J. Lu, C.T. Liu, Y. Yang, High-entropy alloy: challenges and prospects, Mater. Today. 19 (2016) 349–362. https://doi.org/10.1016/j.mattod.2015.11.026.

[22] J.-W. Yeh, Recent progress in high-entropy alloys, Ann. Chim. Sci. Des Matériaux. 31 (2006) 633–648. https://doi.org/10.3166/acsm.31.633-648.

[23] M.A. Adaan-Nyiak, I. Alam, A.A. Tiamiyu, Ball milling process variables optimization for high-entropy alloy development using design of experiment and genetic algorithm, Powder Technol. 427 (2023) 118766. https://doi.org/10.1016/j.powtec.2023.118766.

[24] J.-W. Yeh, S.-J. Lin, T.-S. Chin, J.-Y. Gan, S.-K. Chen, T.-T. Shun, C.-H. Tsau, S.-Y. Chou, Formation of simple crystal structures in Cu-Co-Ni-Cr-Al-Fe-Ti-V alloys with multiprincipal metallic elements, Metall. Mater. Trans. A. 35 (2004) 2533–2536. https://doi.org/10.1007/s11661-006-0234-4.

[25] B. Cantor, I.T.H. Chang, P. Knight, A.J.B. Vincent, Microstructural development in equiatomic multicomponent alloys, Mater. Sci. Eng. A. 375–377 (2004) 213–218. https://doi.org/10.1016/j.msea.2003.10.257.

[26] L. Zhang, H. Fu, S. Ge, Z. Zhu, H. Li, H. Zhang, A. Wang, H. Zhang, Phase transformations in body-centered cubic NbxHfZrTi high-entropy alloys, Mater. Charact. 142 (2018) 443–448. https://doi.org/10.1016/j.matchar.2018.06.012.

[27] J. Hu, E. Walkar, Z. Yu, A. Abdelmotagaly, B. Schneiderman, Multi-material Component and Methods of Making Thereof, United States Patent 0036840 A1, 2018.

[28] Y. Xin, S. Li, Y. Qian, W. Zhu, H. Yuan, P. Jiang, R. Guo, L. Wang, High-Entropy Alloys

as a Platform for Catalysis: Progress, Challenges, and Opportunities, ACS Catal. 10 (2020) 11280–11306. https://doi.org/10.1021/acscatal.0c03617.

[29]   J. Liu, X. Wang, A. Singh, H. Xu, F. Kong, F. Yang, The Evolution of Intermetallic Compounds in High-Entropy Alloys: From the Secondary Phase to the Main Phase, Metals (Basel). 11 (2021) 2054. https://doi.org/10.3390/met11122054.

[30]   R. Jayasree, R.B. Mane, R. Vijay, D. Chakravarty, Effect of process control agents on mechanically alloyed Al0.3CoCrFeNi, Mater. Lett. 292 (2021) 129618. https://doi.org/10.1016/j.matlet.2021.129618.

[31]   C.C. Koch, Nanocrystalline high-entropy alloys, J. Mater. Res. 32 (2017) 3435–3444. https://doi.org/10.1557/jmr.2017.341.

[32]   Y.-L. Chen, C.-W. Tsai, C.-C. Juan, M.-H. Chuang, J.-W. Yeh, T.-S. Chin, S.-K. Chen, Amorphization of equimolar alloys with HCP elements during mechanical alloying, J. Alloys Compd. 506 (2010) 210–215. https://doi.org/10.1016/j.jallcom.2010.06.179.

[33]   O. Maulik, D. Kumar, S. Kumar, S.K. Dewangan, V. Kumar, Structure and properties of lightweight high entropy alloys: a brief review, Mater. Res. Express. 5 (2018) 052001. https://doi.org/10.1088/2053-1591/aabbca.

[34]   X. Yang, S.Y. Chen, J.D. Cotton, Y. Zhang, Phase Stability of Low-Density, Multiprincipal Component Alloys Containing Aluminum, Magnesium, and Lithium, JOM. 66 (2014). https://doi.org/10.1007/s11837-014-1059-z.

[35]   K. Guruvidyathri, B.S. Murty, J.W. Yeh, K.C. Hari Kumar, Gibbs energy-composition plots as a tool for high-entropy alloy design, J. Alloys Compd. 768 (2018) 358–367.

https://doi.org/10.1016/j.jallcom.2018.07.264.

[36] H.-W. Luan, Y. Shao, J.-F. Li, W.-L. Mao, Z.-D. Han, C. Shao, K.-F. Yao, Phase stabilities of high entropy alloys, Scr. Mater. 179 (2020) 40–44. https://doi.org/10.1016/j.scriptamat.2019.12.041.

[37] S. SARKAR, S. BANERJEE, S. ROY, R. GHOSH, P.P. RAY, B. BAGCHI, Composition dependent non-ideality in aqueous binary mixtures as a signature of avoided spinodal decomposition, J. Chem. Sci. 127 (2015) 49–59. https://doi.org/10.1007/s12039-014-0749-y.

[38] Y. Zhang, T.T. Zuo, Z. Tang, M.C. Gao, K.A. Dahmen, P.K. Liaw, Z.P. Lu, Microstructures and properties of high-entropy alloys, Prog. Mater. Sci. 61 (2014) 1–93. https://doi.org/10.1016/j.pmatsci.2013.10.001.

[39] Y.Y. Zhao, Z.F. Lei, Z.P. Lu, J.C. Huang, T.G. Nieh, A simplified model connecting lattice distortion with friction stress of Nb-based equiatomic high-entropy alloys, Mater. Res. Lett. 7 (2019) 340–346. https://doi.org/10.1080/21663831.2019.1610105.

[40] Y.Y. Zhao, T.G. Nieh, Correlation between lattice distortion and friction stress in Ni-based equiatomic alloys, Intermetallics. 86 (2017) 45–50. https://doi.org/10.1016/j.intermet.2017.03.011.

[41] Z. Wang, Q. Fang, J. Li, B. Liu, Y. Liu, Effect of lattice distortion on solid solution strengthening of BCC high-entropy alloys, J. Mater. Sci. Technol. 34 (2018) 349–354. https://doi.org/10.1016/j.jmst.2017.07.013.

[42] N. Ali, L. Zhang, D. Liu, H. Zhou, K. Sanaullah, C. Zhang, J. Chu, Y. Nian, J. Cheng,

Strengthening mechanisms in high entropy alloys: A review, Mater. Today Commun. 33 (2022) 104686. https://doi.org/10.1016/j.mtcomm.2022.104686.

[43]   J. Chen, X. Jiang, H. Sun, Z. Shao, Y. Fang, R. Shu, Phase transformation and strengthening mechanisms of nanostructured high-entropy alloys, Nanotechnol. Rev. 10 (2021) 1116–1139. https://doi.org/10.1515/ntrev-2021-0071.

[44]   O.N. Senkov, J.M. Scott, S.V. Senkova, D.B. Miracle, C.F. Woodward, Microstructure and room temperature properties of a high-entropy TaNbHfZrTi alloy, J. Alloys Compd. 509 (2011) 6043–6048. https://doi.org/10.1016/j.jallcom.2011.02.171.

[45]   K.-H. Cheng, C.-H. Lai, S.-J. Lin, J.-W. Yeh, Recent progress in multi-element alloy and nitride coatings sputtered from high-entropy alloy targets, Ann. Chim. Sci. Des Matériaux. 31 (2006) 723–736. https://doi.org/10.3166/acsm.31.723-736.

[46]   B. Gludovatz, A. Hohenwarter, D. Catoor, E.H. Chang, E.P. George, R.O. Ritchie, A fracture-resistant high-entropy alloy for cryogenic applications, Science (80-.). 345 (2014) 1153–1158. https://doi.org/10.1126/science.1254581.

[47]   Z. Li, K.G. Pradeep, Y. Deng, D. Raabe, C.C. Tasan, Metastable high-entropy dual-phase alloys overcome the strength–ductility trade-off, Nature. 534 (2016) 227–230. https://doi.org/10.1038/nature17981.

[48]   A. Nowotnik, Nickel-Based Superalloys, in: J.H. Weber (Ed.), Ref. Modul. Mater. Sci. Mater. Eng., Elsevier, 2016: pp. 6154–6155. https://doi.org/10.1016/B978-0-12-803581-8.02574-1.

[49]   K.M. Youssef, A.J. Zaddach, C. Niu, D.L. Irving, C.C. Koch, A Novel Low-Density,

High-Hardness, High-entropy Alloy with Close-packed Single-phase Nanocrystalline Structures, Mater. Res. Lett. 3 (2015) 95–99. https://doi.org/10.1080/21663831.2014.985855.

[50]   W. Xiong, L. Cheng, S. Zhan, A.X.Y. Guo, P.K. Liaw, S.C. Cao, Recent Advances on Lightweight High-Entropy Alloys: Process, Design, and Applications, High Entropy Alloy. Mater. (2023). https://doi.org/10.1007/s44210-023-00014-y.

[51]   Y. Li, Y. Zhang, Light-Weight and Flexible High-Entropy Alloys, in: Eng. Steels High Entropy-Alloys, IntechOpen, 2020. https://doi.org/10.5772/intechopen.88332.

[52]   A.A. Tiamiyu, A.Y. Badmos, A.G. Odeshi, Effects of temper condition on high strain-rate deformation of AA 2017 aluminum alloy in compression, Mater. Des. 89 (2016) 872–883. https://doi.org/10.1016/j.matdes.2015.10.047.

[53]   K. Tseng, Y. Yang, C. Juan, T. Chin, C. Tsai, J. Yeh, A light-weight high-entropy alloy Al20Be20Fe10Si15Ti35, Sci. China Technol. Sci. 61 (2018) 184–188. https://doi.org/10.1007/s11431-017-9073-0.

[54]   J.D. Destefani, Introduction to Titanium and Titanium Alloys, in: Prop. Sel. Nonferrous Alloy. Spec. Mater., ASM International, Ohio, 1990: pp. 586–591. https://doi.org/10.31399/asm.hb.v02.a0001080.

[55]   N.D. Stepanov, D.G. Shaysultanov, G.A. Salishchev, M.A. Tikhonovsky, Structure and mechanical properties of a light-weight AlNbTiV high entropy alloy, Mater. Lett. 142 (2015) 153–155. https://doi.org/10.1016/j.matlet.2014.11.162.

[56]   O.N. Senkov, S.V. Senkova, C. Woodward, D.B. Miracle, Low-density, refractory multi-

principal element alloys of the Cr–Nb–Ti–V–Zr system: Microstructure and phase

analysis, Acta Mater. 61 (2013) 1545–1557.

https://doi.org/10.1016/j.actamat.2012.11.032.

[57]   R. Li, J.C. Gao, K. Fan, Study to Microstructure and Mechanical Properties of Mg

Containing High Entropy Alloys, Mater. Sci. Forum. 650 (2010) 265–271.

https://doi.org/10.4028/www.scientific.net/MSF.650.265.

[58]   O. Maulik, D. Kumar, S. Kumar, D.M. Fabijanic, V. Kumar, Structural evolution of spark

plasma sintered AlFeCuCrMgx (x = 0, 0.5, 1, 1.7) high entropy alloys, Intermetallics. 77

(2016) 46–56. https://doi.org/10.1016/j.intermet.2016.07.001.

[59]   X.H. Du, R. Wang, C. Chen, B.L. Wu, J.C. Huang, Preparation of a Light-Weight

MgCaAlLiCu High-Entropy Alloy, Key Eng. Mater. 727 (2017) 132–135.

https://doi.org/10.4028/www.scientific.net/KEM.727.132.

[60]   G. Zepon, D.R. Leiva, R.B. Strozi, A. Bedoch, S.J.A. Figueroa, T.T. Ishikawa, W.J. Botta,

Hydrogen-induced phase transition of MgZrTiFe0.5Co0.5Ni0.5 high entropy alloy, Int. J.

Hydrogen Energy. 43 (2018) 1702–1708. https://doi.org/10.1016/j.ijhydene.2017.11.106.

[61]   A. Kumar, M. Gupta, An Insight into Evolution of Light Weight High Entropy Alloys: A

Review, Metals (Basel). 6 (2016) 199. https://doi.org/10.3390/met6090199.

[62]   L. Cui, Z. Zhang, X.-G. Chen, Microstructure and mechanical properties of novel Al–Cu–

Mg–Zn lightweight entropy alloys for elevated-temperature applications, Mater. Charact.

200 (2023) 112927. https://doi.org/10.1016/j.matchar.2023.112927.

[63]   L. Cui, Z. Zhang, X.-G. Chen, Development of lightweight Al-based entropy alloys for

elevated temperature applications, J. Alloys Compd. 938 (2023) 168619.

https://doi.org/10.1016/j.jallcom.2022.168619.

[64] L. Rogal, Y. Ikeda, M. Lai, F. Körmann, A. Kalinowska, B. Grabowski, Design of a dual-phase hcp-bcc high entropy alloy strengthened by ω nanoprecipitates in the Sc-Ti-Zr-Hf-Re system, Mater. Des. 192 (2020) 108716. https://doi.org/10.1016/j.matdes.2020.108716.

[65] Z. Li, C.C. Tasan, K.G. Pradeep, D. Raabe, A TRIP-assisted dual-phase high-entropy alloy: Grain size and phase fraction effects on deformation behavior, Acta Mater. 131 (2017) 323–335. https://doi.org/10.1016/j.actamat.2017.03.069.

[66] Y. Qiu, Y.J. Hu, A. Taylor, M.J. Styles, R.K.W. Marceau, A.V. Ceguerra, M.A. Gibson, Z.K. Liu, H.L. Fraser, N. Birbilis, A lightweight single-phase AlTiVCr compositionally complex alloy, Acta Mater. 123 (2017) 115–124. https://doi.org/10.1016/j.actamat.2016.10.037.

[67] S. Guo, C. Ng, J. Lu, C.T. Liu, Effect of valence electron concentration on stability of fcc or bcc phase in high entropy alloys, J. Appl. Phys. 109 (2011) 103505. https://doi.org/10.1063/1.3587228.

[68] S. Yang, J. Lu, F. Xing, L. Zhang, Y. Zhong, Revisit the VEC rule in high entropy alloys (HEAs) with high-throughput CALPHAD approach and its applications for material design-A case study with Al–Co–Cr–Fe–Ni system, Acta Mater. 192 (2020) 11–19. https://doi.org/10.1016/j.actamat.2020.03.039.

[69] S.A. Kube, S. Sohn, D. Uhl, A. Datye, A. Mehta, J. Schroers, Phase selection motifs in High Entropy Alloys revealed through combinatorial methods: Large atomic size difference favors BCC over FCC, Acta Mater. 166 (2019) 677–686.

https://doi.org/10.1016/j.actamat.2019.01.023.

[70]   S. Guo, Q. Hu, C. Ng, C.T. Liu, More than entropy in high-entropy alloys: Forming solid

solutions or amorphous phase, Intermetallics. 41 (2013) 96–103.

https://doi.org/10.1016/j.intermet.2013.05.002.

[71]   Z. Wang, S. Guo, C.T. Liu, Phase Selection in High-Entropy Alloys: From

Nonequilibrium to Equilibrium, JOM. 66 (2014) 1966–1972.

https://doi.org/10.1007/s11837-014-0953-8.

[72]   A. Takeuchi, K. Amiya, T. Wada, K. Yubuta, W. Zhang, A. Makino, Alloy Designs of

High-Entropy Crystalline and Bulk Glassy Alloys by Evaluating Mixing Enthalpy and

Delta Parameter for Quinary to Decimal Equi-Atomic Alloys, Mater. Trans. 55 (2014)

165–170. https://doi.org/10.2320/matertrans.M2013352.

[73]   A. Kumar, A.K. Swarnakar, A. Basu, M. Chopkar, Effects of processing route on phase

evolution and mechanical properties of CoCrCuFeNiSix high entropy alloys, J. Alloys

Compd. 748 (2018) 889–897. https://doi.org/10.1016/j.jallcom.2018.03.242.

[74]   Q. Tang, Y. Huang, H. Cheng, X. Liao, T.G. Langdon, P. Dai, The effect of grain size on

the annealing-induced phase transformation in an Al0·3CoCrFeNi high entropy alloy,

Mater. Des. 105 (2016) 381–385. https://doi.org/10.1016/j.matdes.2016.05.079.

[75]   W. Liao, S. Lan, L. Gao, H. Zhang, S. Xu, J. Song, X. Wang, Y. Lu, Nanocrystalline high-

entropy alloy (CoCrFeNiAl0.3) thin-film coating by magnetron sputtering, Thin Solid

Films. 638 (2017) 383–388. https://doi.org/10.1016/j.tsf.2017.08.006.

[76]   A. Heczel, M. Kawasaki, J.L. Lábár, J. Jang, T.G. Langdon, J. Gubicza, Defect structure

and hardness in nanocrystalline CoCrFeMnNi High-Entropy Alloy processed by High-Pressure Torsion, J. Alloys Compd. 711 (2017) 143–154. https://doi.org/10.1016/j.jallcom.2017.03.352.

[77]   S.-H. Joo, H. Kato, M.J. Jang, J. Moon, E.B. Kim, S.-J. Hong, H.S. Kim, Structure and properties of ultrafine-grained CoCrFeMnNi high-entropy alloys produced by mechanical alloying and spark plasma sintering, J. Alloys Compd. 698 (2017) 591–604. https://doi.org/10.1016/j.jallcom.2016.12.010.

[78]   A. Canakci, T. Varol, C. Nazik, Effects of amount of methanol on characteristics of mechanically alloyed Al–Al 2 O 3 composite powders, Mater. Technol. 27 (2012) 320–327. https://doi.org/10.1179/1753555712Y.0000000014.

[79]   C.A. Schneider, W.S. Rasband, K.W. Eliceiri, NIH Image to ImageJ: 25 years of image analysis, Nat. Methods. 9 (2012) 671–675. https://doi.org/10.1038/nmeth.2089.

[80]   S. Praveen, A. Anupam, R. Tilak, R.S. Kottada, Phase evolution and thermal stability of AlCoCrFe high entropy alloy with carbon as unsolicited addition from milling media, Mater. Chem. Phys. 210 (2018) 57–61. https://doi.org/10.1016/j.matchemphys.2017.10.040.

[81]   L. Zhang, C. Jiang, C. Wu, H. Ju, G. Jiang, W. Liu, C. Zhu, T. Chen, V2O5 as Hole Transporting Material for Efficient All Inorganic Sb2S3 Solar Cells, ACS Appl. Mater. Interfaces. 10 (2018) 27098–27105. https://doi.org/10.1021/acsami.8b09843.

[82]   N. Yazdani, M.R. Toroghinejad, A. Shabani, P. Cavaliere, Effects of Process Control Agent Amount, Milling Time, and Annealing Heat Treatment on the Microstructure of AlCrCuFeNi High-Entropy Alloy Synthesized through Mechanical Alloying, Metals

(Basel). 11 (2021) 1493. https://doi.org/10.3390/met11091493.

[83] B.-L. Huang, R.J. Perez, E.J. Lavernia, M.J. Luton, Formation of supersaturated solid solutions by mechanical alloying, Nanostructured Mater. 7 (1996) 67–79. https://doi.org/10.1016/0965-9773(95)00299-5.

[84] P.G. E. Murch, Diffusion Kinetics in Solids, in: G. Kostorz (Ed.), Phase Transform. Mater., Wiley, 2001: pp. 171–238. https://doi.org/10.1002/352760264X.

[85] M. Huang, J. Jiang, Y. Wang, Y. Liu, Y. Zhang, Effects of milling process parameters and PCAs on the synthesis of Al0.8Co0.5Cr1.5CuFeNi high entropy alloy powder by mechanical alloying, Mater. Des. 217 (2022) 110637. https://doi.org/10.1016/j.matdes.2022.110637.

[86] M.M. Moshksar, M. Mirzaee, Formation of NiAl intermetallic by gradual and explosive exothermic reaction mechanism during ball milling, Intermetallics. 12 (2004) 1361–1366. https://doi.org/10.1016/j.intermet.2004.03.018.

[87] F. Hadef, A. Otmani, A. Djekoun, J.M. Grenèche, Structural and microstructural study of nanostructured Fe50Al40Ni10 powders produced by mechanical alloying, Mater. Charact. 62 (2011) 751–759. https://doi.org/10.1016/j.matchar.2011.05.005.

[88] Y. Qiao, Y. Tang, S. Li, Y. Ye, X. Liu, L. Zhu, S. Bai, Preparation of TiZrNbTa refractory high-entropy alloy powder by mechanical alloying with liquid process control agents, Intermetallics. 126 (2020) 106900. https://doi.org/10.1016/j.intermet.2020.106900.

[89] G. Wang, Q. Liu, J. Yang, X. Li, X. Sui, Y. Gu, Y. Liu, Synthesis and thermal stability of a nanocrystalline MoNbTaTiV refractory high-entropy alloy via mechanical alloying, Int.

J. Refract. Met. Hard Mater. 84 (2019) 104988.

https://doi.org/10.1016/j.ijrmhm.2019.104988.

[90]   F. Salemi, M.H. Abbasi, F. Karimzadeh, Synthesis and thermodynamic analysis of

        nanostructured CuNiCoZnAl high entropy alloy produced by mechanical alloying, J.

        Alloys Compd. 685 (2016) 278–286. https://doi.org/10.1016/j.jallcom.2016.05.274.

[91]   X. Yang, J. Zhang, S. Sagar, T. Dube, B.-G. Kim, Y.-G. Jung, D.D. Koo, A. Jones, J.

        Zhang, Molecular dynamics modeling of mechanical and tribological properties of

        additively manufactured AlCoCrFe high entropy alloy coating on aluminum substrate,

        Mater. Chem. Phys. 263 (2021) 124341.

        https://doi.org/10.1016/j.matchemphys.2021.124341.

[92]   Z. Li, F. Körmann, B. Grabowski, J. Neugebauer, D. Raabe, Ab initio assisted design of

        quinary dual-phase high-entropy alloys with transformation-induced plasticity, Acta

        Mater. 136 (2017) 262–270. https://doi.org/10.1016/j.actamat.2017.07.023.

[93]   S.S. Nene, M. Frank, P. Agrawal, S. Sinha, K. Liu, S. Shukla, R.S. Mishra, B.A.

        McWilliams, K.C. Cho, Microstructurally flexible high entropy alloys: Linkages between

        alloy design and deformation behavior, Mater. Des. 194 (2020) 108968.

        https://doi.org/10.1016/j.matdes.2020.108968.

[94]   C. Huang, Y. Yao, X. Peng, S. Chen, Plastic deformation and strengthening mechanism of

        FCC/HCP nano-laminated dual-phase CoCrFeMnNi high entropy alloy, Nanotechnology.

        32 (2021) 505724. https://doi.org/10.1088/1361-6528/ac2980.

[95]   V.H. Hammond, M.A. Atwater, K.A. Darling, H.Q. Nguyen, L.J. Kecskes, Equal-Channel

        Angular Extrusion of a Low-Density High-Entropy Alloy Produced by High-Energy

Cryogenic Mechanical Alloying, JOM. 66 (2014) 2021–2029.

https://doi.org/10.1007/s11837-014-1113-x.

[96]   J. Qi, A.M. Cheung, S.J. Poon, High Entropy Alloys Mined From Binary Phase Diagrams,

Sci. Rep. 9 (2019) 15501. https://doi.org/10.1038/s41598-019-50015-4.

[97]   W.F. Gale, T.C. Totemeier, eds., Equillibrium Diagrams, in: Smithells Met. Ref. B., 8th

Editio, Elsevier, 2003: pp. 1–534.

[98]   S.-M. Liang, H.K. Singh, H. Zhang, R. Schmid-Fetzer, Phase equilibria of the Zn-Ti

system: Experiments, first-principles calculations and Calphad assessment, Calphad. 64

(2019) 213–224. https://doi.org/10.1016/j.calphad.2018.12.009.

[99]   R. Bateni, J. A. Szpunar, F. Ashrafizadeh, M. Zandrahimi, THE EFFECT OF NOVEL Ti -

Cu INTERMETALLIC COMPOUNDCOATINGS ON TRIBOLOGICAL PROPERTIES

OF COPPER, in: Ann. Univ. "DUNĂREA JOS" GALAŢIFASCICLE VIII, Tribol., 2003:

pp. 55–62.

[100] F. Otto, A. Dlouhý, K.G. Pradeep, M. Kuběnová, D. Raabe, G. Eggeler, E.P. George,

Decomposition of the single-phase high-entropy alloy CrMnFeCoNi after prolonged

anneals at intermediate temperatures, Acta Mater. 112 (2016).

https://doi.org/10.1016/j.actamat.2016.04.005.

[101] F. Otto, Y. Yang, H. Bei, E.P. George, Relative effects of enthalpy and entropy on the

phase stability of equiatomic high-entropy alloys, Acta Mater. 61 (2013) 2628–2638.

https://doi.org/10.1016/j.actamat.2013.01.042.

[102] A. Takeuchi, T. Wada, H. Kato, Solid Solutions with bcc, hcp, and fcc Structures Formed

in a Composition Line in Multicomponent Ir–Rh–Ru–W–Mo System, Mater. Trans. 60 (2019) 2267–2276. https://doi.org/10.2320/matertrans.MT-M2019212.

[103] A. Takeuchi, T. Wada, H. Kato, High-Entropy Alloys with Hexagonal Close-Packed Structure in Ir26Mo20Rh22.5Ru20W11.5 and Ir25.5Mo20Rh20Ru25W9.5 Alloys Designed by Sandwich Strat, Mater. Trans. 60 (2019) 1666–1673. https://doi.org/10.2320/matertrans.M2019037.

[104] X. Feng, R. Zheng, Z. Wu, Y. Zhang, Z. Li, X. Tan, H. Xu, Study on a new high-entropy alloy Nd20Pr20La20Fe20Co10Al10 with hard magnetic properties, J. Alloys Compd. 882 (2021) 160640. https://doi.org/10.1016/j.jallcom.2021.160640.

[105] Y. Liu, N. Qu, X. Zhao, J. Chen, J. Zhu, Z. Lai, Stability of FeCrNiTiAl high-entropy alloy at high temperature, Heat Treat. Surf. Eng. 3 (2021) 29–36. https://doi.org/10.1080/25787616.2021.2019390.

[106] D. Miracle, J. Miller, O. Senkov, C. Woodward, M. Uchic, J. Tiley, Exploration and Development of High Entropy Alloys for Structural Applications, Entropy. 16 (2014) 494–525. https://doi.org/10.3390/e16010494.

[107] P. Chauhan, S. Yebaji, V.N. Nadakuduru, T. Shanmugasundaram, Development of a novel light weight Al35Cr14Mg6Ti35V10 high entropy alloy using mechanical alloying and spark plasma sintering, J. Alloys Compd. 820 (2020) 153367. https://doi.org/10.1016/j.jallcom.2019.153367.

[108] E.-J. Baek, T.-Y. Ahn, J.-G. Jung, J.-M. Lee, Y.-R. Cho, K. Euh, Effects of ultrasonic melt treatment and solution treatment on the microstructure and mechanical properties of low-density multicomponent Al70Mg10Si10Cu5Zn5 alloy, J. Alloys Compd. 696 (2017) 450–

459. https://doi.org/10.1016/j.jallcom.2016.11.305.

[109] J.G. Kaufman, ed., Properties of Aluminum Alloys: Tensile, Creep, and Fatigue Data at High and Low Temperatures, ASM international, 1999.

[110] P.T. Summers, Y. Chen, C.M. Rippe, B. Allen, A.P. Mouritz, S.W. Case, B.Y. Lattimer, Overview of aluminum alloy mechanical properties during and after fires, Fire Sci. Rev. 4 (2015) 3. https://doi.org/10.1186/s40038-015-0007-5.

[111] R. Li, J.C. Gao, K. Fan, Microstructure and Mechanical Properties of MgMnAlZnCu High Entropy Alloy Cooling in Three Conditions, Mater. Sci. Forum. 686 (2011) 235–241. https://doi.org/10.4028/www.scientific.net/MSF.686.235.

[112] F. Gao, Y. Sun, L. Hu, J. Shen, W. Liu, M. Ba, C. Deng, Microstructural evolution and thermal stability in a nanocrystalline lightweight TiAlV0.5CrMo refractory high-entropy alloy synthesized by mechanical alloying, Mater. Lett. 329 (2022) 133179. https://doi.org/10.1016/j.matlet.2022.133179.

[113] O. Maulik, V. Kumar, Synthesis of AlFeCuCrMgx (x=0, 0.5, 1, 1.7) alloy powders by mechanical alloying, Mater. Charact. 110 (2015) 116–125. https://doi.org/10.1016/j.matchar.2015.10.025.

[114] Y. Wang, C. Wu, Y. Liu, M. Tian, X. Lu, X. Su, Insight into the FCC→HCP Transformation in Co-Rich Co-Cr-Fe-Mn-Ni High-Entropy Alloys, Metals (Basel). 13 (2023) 504. https://doi.org/10.3390/met13030504.

[115] J. Kieffer, D. Karkoulis, PyFAI, a versatile library for azimuthal regrouping, J. Phys. Conf. Ser. 425 (2013) 202012. https://doi.org/10.1088/1742-6596/425/20/202012.

[116] W. Guo, B. Liu, Y. Liu, T. Li, A. Fu, Q. Fang, Y. Nie, Microstructures and mechanical properties of ductile NbTaTiV refractory high entropy alloy prepared by powder metallurgy, J. Alloys Compd. 776 (2019) 428–436. https://doi.org/10.1016/j.jallcom.2018.10.230.

[117] H. Putz, K. Brandenburg, Match! - Phase Analysis using Powder Diffraction, Version 3.x, Crystal Impact, (2023). https://www.crystalimpact.de/match (accessed October 18, 2023).

[118] P. Juhás, T. Davis, C.L. Farrow, S.J.L. Billinge, PDFgetX3 : a rapid and highly automatable program for processing powder diffraction data into total scattering pair distribution functions, J. Appl. Crystallogr. 46 (2013) 560–566. https://doi.org/10.1107/S0021889813005190.

[119] ASTM, E3-11 Standard Guide for Preparation of Metallographic Specimens 1, 2017. https://doi.org/10.1520/E0003-11.2.

[120] W.C. Oliver, G.M. Pharr, Measurement of hardness and elastic modulus by instrumented indentation: Advances in understanding and refinements to methodology, J. Mater. Res. 19 (2004) 3–20. https://doi.org/10.1557/jmr.2004.19.1.3.

[121] S. Yebaji, A. Saurav, P. Chauhan, B.S. Murty, B. Patil, A. Babu, V. Poddar, T. Shanmugasundaram, Phase Stability of AlCoTiZn High-Entropy Alloy Prepared by Mechanical Alloying, J. Mater. Eng. Perform. 32 (2023) 3668–3677. https://doi.org/10.1007/s11665-022-07332-z.

[122] K.G. Pradeep, N. Wanderka, P. Choi, J. Banhart, B.S. Murty, D. Raabe, Atomic-scale compositional characterization of a nanocrystalline AlCrCuFeNiZn high-entropy alloy using atom probe tomography, Acta Mater. 61 (2013) 4696–4706.

https://doi.org/10.1016/j.actamat.2013.04.059.

[123] Q. Cheng, Y. Zhang, X.D. Xu, D. Wu, S. Guo, T.G. Nieh, J.H. Chen, Mechanistic origin of abnormal annealing-induced hardening in an AlCoCrFeNi2.1 eutectic multi-principal-element alloy, Acta Mater. 252 (2023) 118905. https://doi.org/10.1016/j.actamat.2023.118905.

[124] Y.C. Kim, W.T. Kim, D.H. Kim, A development of Ti-based bulk metallic glass, Mater. Sci. Eng. A. 375–377 (2004) 127–135. https://doi.org/10.1016/j.msea.2003.10.115.

[125] C. Nagarjuna, S.K. Dewangan, H. Lee, B. Ahn, Evolution of phase stability and structural properties in CrFeNiTiV high-entropy alloy under high-temperature heat treatment conditions, Mater. Sci. Eng. A. 886 (2023) 145680. https://doi.org/10.1016/j.msea.2023.145680.

[126] I. Chicinas, V. Pop, O. Isnard, Synthesis of the Supermalloy Powders by Mechanical Alloying, J. Mater. Sci. 39 (2004) 5305–5309. https://doi.org/10.1023/B:JMSC.0000039234.58490.78.

[127] A.P. Zhilyaev, G. V. Nurislamova, S. Surinach, M.D. Baró, T.G. Langdon, Calorimetric measurements of grain growth in ultrafine-grained nickel, Mater. Phys. Mech. 5 (2002) 23–30.

[128] T.H. Chou, J.C. Huang, C.H. Yang, S.K. Lin, T.G. Nieh, Consideration of kinetics on intermetallics formation in solid-solution high entropy alloys, Acta Mater. 195 (2020) 71–80. https://doi.org/10.1016/j.actamat.2020.05.015.

[129] N. Singh, Y. Shadangi, N.K. Mukhopadhyay, Phase Evolution and Thermal Stability of

Low-Density MgAlSiCrFe High-Entropy Alloy Processed Through Mechanical Alloying, Trans. Indian Inst. Met. 73 (2020) 2377–2386. https://doi.org/10.1007/s12666-020-02039-y.

[130] M. Abdellaoui, T. Barradi, E. Gaffet, Mechanism of mechanical alloying phase formation and related magnetic and mechanical properties in the Fe☐Si system, J. Alloys Compd. 198 (1993) 155–164. https://doi.org/10.1016/0925-8388(93)90159-K.

[131] P.T. Hung, M. Kawasaki, J.-K. Han, J.L. Lábár, J. Gubicza, Microstructure evolution in a nanocrystalline CoCrFeNi multi-principal element alloy during annealing, Mater. Charact. 171 (2021) 110807. https://doi.org/10.1016/j.matchar.2020.110807.

[132] K.R. Lim, K.S. Lee, J.S. Lee, J.Y. Kim, H.J. Chang, Y.S. Na, Dual-phase high-entropy alloys for high-temperature structural applications, J. Alloys Compd. 728 (2017) 1235–1238. https://doi.org/10.1016/j.jallcom.2017.09.089.

[133] X.P. Zhu, N. Gao, Z.C. Bai, K. Wang, J.Q. Yao, Z.T. Fan, Z.D. Wang, X.W. Liu, Phase stability of a light-weight AlNb2TiV refractory high-entropy alloy at high temperature, Mater. Lett. 325 (2022) 132897. https://doi.org/10.1016/j.matlet.2022.132897.

[134] R.K. Mishra, R.R. Shahi, A novel low-density semi-hard magnetic Al20Fe20Mg20Ni20Ti20 high entropy alloy, J. Magn. Magn. Mater. 516 (2020) 167342. https://doi.org/10.1016/j.jmmm.2020.167342.

[135] R.M.R. Wellen, E.L. Canedo, On the Kissinger equation and the estimate of activation energies for non-isothermal cold crystallization of PET, Polym. Test. 40 (2014) 33–38. https://doi.org/10.1016/j.polymertesting.2014.08.008.

[136] Y. Zhang, Z. Chen, D. Cao, J. Zhang, P. Zhang, Q. Tao, X. Yang, Concurrence of spinodal decomposition and nano-phase precipitation in a multi-component AlCoCrCuFeNi high-entropy alloy, J. Mater. Res. Technol. 8 (2019) 726–736. https://doi.org/10.1016/j.jmrt.2018.04.020.

[137] Y. Yu, J. Wang, J. Li, H. Kou, W. Liu, Characterization of BCC phases in AlCoCrFeNiTix high entropy alloys, Mater. Lett. 138 (2015) 78–80. https://doi.org/10.1016/j.matlet.2014.09.100.

[138] A. Powell, U. Pal, J. van den Avyle, B. Damkroger, J. Szekely, Analysis of multicomponent evaporation in electron beam melting and refining of titanium alloys, Metall. Mater. Trans. B. 28 (1997) 1227–1239. https://doi.org/10.1007/s11663-997-0078-3.

[139] X. He, T. DebRoy, P.W. Fuerschbach, Alloying element vaporization during laser spot welding of stainless steel, J. Phys. D. Appl. Phys. 36 (2003) 3079–3088. https://doi.org/10.1088/0022-3727/36/23/033.

[140] D.F. Heaney, Vacuum sintering, in: Sinter. Adv. Mater., Elsevier, 2010: pp. 189–221. https://doi.org/10.1533/9781845699949.2.189.

[141] X. Li, F. He, F. Behrendt, Z. Gao, J. Shi, C. Li, Inhibition of K2SO4 on evaporation of KCl in combustion of herbaceous biomass, Fuel. 289 (2021) 119754. https://doi.org/10.1016/j.fuel.2020.119754.

[142] S.J.L. Billinge, The rise of the X-ray atomic pair distribution function method: a series of fortunate events, Philos. Trans. R. Soc. A Math. Phys. Eng. Sci. 377 (2019) 20180413. https://doi.org/10.1098/rsta.2018.0413.

[143] C. Wang, W. Ji, Z. Fu, Mechanical alloying and spark plasma sintering of CoCrFeNiMnAl high-entropy alloy, Adv. Powder Technol. 25 (2014) 1334–1338. https://doi.org/10.1016/j.apt.2014.03.014.

[144] L. Li, Z. Li, A. Kwiatkowski da Silva, Z. Peng, H. Zhao, B. Gault, D. Raabe, Segregation-driven grain boundary spinodal decomposition as a pathway for phase nucleation in a high-entropy alloy, Acta Mater. 178 (2019) 1–9. https://doi.org/10.1016/j.actamat.2019.07.052.

[145] B. Niu, W. Ji, N. Li, F. Zhang, Y. Wu, Alloying and thermal behaviour of CoCrFeNiMn 0.5 Ti 0.5 high-entropy alloy synthesised by mechanical alloying, Mater. Sci. Technol. 32 (2016) 94–98. https://doi.org/10.1179/1743284715Y.0000000124.

[146] S. Simoes, R. Calinas, M.T. Vieira, M.F. Vieira, P.J. Ferreira, In situ TEM study of grain growth in nanocrystalline copper thin films, Nanotechnology. 21 (2010). https://doi.org/10.1088/0957-4484/21/14/145701.

[147] P. Cao, L. Lu, M.O. Lai, Grain growth and kinetics for nanocrystalline magnesium alloy produced by mechanical alloying, Mater. Res. Bull. 36 (2001) 981–988. https://doi.org/10.1016/S0025-5408(01)00578-5.

[148] M. Jalaly, M.H. Enayati, P. Kameli, F. Karimzadeh, Effect of composition on structural and magnetic properties of nanocrystalline ball milled Ni1−xZnxFe2O4 ferrite, Phys. B Condens. Matter. 405 (2010) 507–512. https://doi.org/10.1016/j.physb.2009.09.044.

[149] P. Thirathipviwat, S. Sato, G. Song, J. Bednarcik, K. Nielsch, J. Han, Compositional complexity dependence of lattice distortion in FeNiCoCrMn high entropy alloy system, Mater. Sci. Eng. A. 823 (2021) 141775. https://doi.org/10.1016/j.msea.2021.141775.

[150] D. Drey, E. O'Quinn, S. Finkeldei, J. Neuefeind, M. Lang, Local ordering in disordered Nd Zr1-O2-0.5 pyrochlore as observed using neutron total scattering, Acta Mater. 225 (2022) 117590. https://doi.org/10.1016/j.actamat.2021.117590.

[151] Q.-H. Gao, A. Du, Z.-J. Yang, Structural inheritance and difference between Ti 2 AlC, Ti 3 AlC 2 and Ti 5 Al 2 C 3 under pressure from first principles, Mod. Phys. Lett. B. 31 (2017) 1750016. https://doi.org/10.1142/S0217984917500166.

[152] The Materials Project, Materials Data on TiAlV2 by Materials Project, (2020). https://doi.org/10.17188/1758747.

[153] The Materials Project, Materials Data on Li4(AlCu2)3 by Materials Project., (2020). https://doi.org/10.17188/1679744.

[154] The Materials Project, Materials Data on Ti2AlCu by Materials Project, (2020). https://doi.org/10.17188/1317466.

[155] The Materials Project, Materials Data on Sm(AlZn)2 by Materials Project, (2020). https://doi.org/10.17188/1275197.

[156] The Materials Project, Materials Data on Zn8Cu5 by Materials Project, (2017). https://doi.org/10.17188/1189714.

[157] Y. Yang, H. Chen, C. Ye, EXAFS and DFT studies of microscopic structure with different density upon Zn(II) adsorption on anatase TiO2, Adsorption. 19 (2013) 1019–1025. https://doi.org/10.1007/s10450-013-9510-y.

[158] Y. Zhang, H. Wu, X. Yu, D. Tang, R. Yuan, H. Sun, Microstructural evolution and strengthening mechanisms in CrxMnFeNi high-entropy alloy, J. Mater. Res. Technol. 12

(2021) 2114–2127. https://doi.org/10.1016/j.jmrt.2021.04.020.

[159] X. Liu, C. Zhang, C. Zhu, K. Vecchio, Creating heterogeneous lamella structure in a multiphase Al-Cr-Fe-Co-Ni complex concentrated alloy, Mater. Sci. Eng. A. 858 (2022) 144150. https://doi.org/10.1016/j.msea.2022.144150.

[160] R. RODRIGUEZ, I. GUTIERREZ, Correlation between nanoindentation and tensile propertiesInfluence of the indentation size effect, Mater. Sci. Eng. A. 361 (2003) 377–384. https://doi.org/10.1016/S0921-5093(03)00563-X.

[161] E.N. Hahn, M.A. Meyers, Grain-size dependent mechanical behavior of nanocrystalline metals, Mater. Sci. Eng. A. 646 (2015) 101–134. https://doi.org/10.1016/j.msea.2015.07.075.

[162] L. Zhang, Y. Shibuta, Inverse Hall-Petch relationship of high-entropy alloy by atomistic simulation, Mater. Lett. 274 (2020) 128024. https://doi.org/10.1016/j.matlet.2020.128024.

[163] T.J. Rupert, J.R. Trelewicz, C.A. Schuh, Grain boundary relaxation strengthening of nanocrystalline Ni-W alloys, J. Mater. Res. 27 (2012) 1285–1294. https://doi.org/10.1557/jmr.2012.55.

[164] Ansys GRANTA EduPack software, ANSYS, Inc., Cambridge, UK. (2022). www.ansys.com/materials.

Appendix

Supplementary Section of Chapter 3
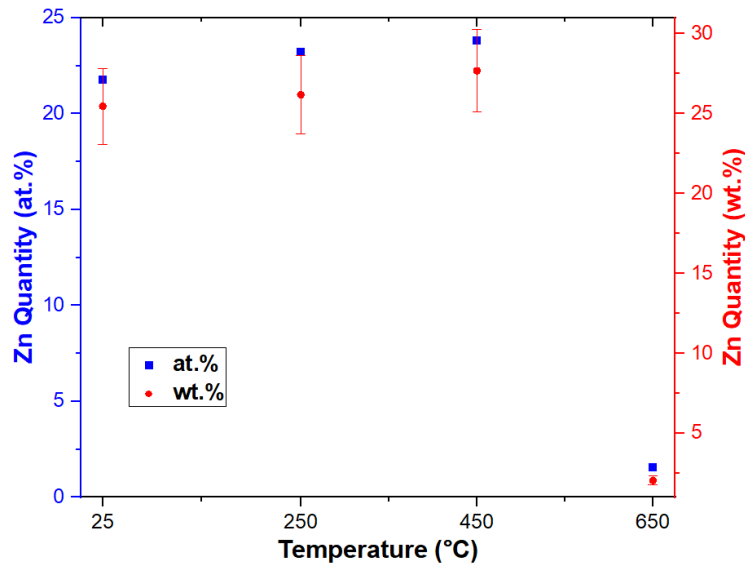
Figure A1: Variation in wt.% and at.% of Zn for the as-milled and annealed AlTi$_{0.45}$CuZn LHEA based on the quantification from the STEM/EDS maps. Although the quantification is not reliable due to the strong Cu signal from the TEM Cu grid used during measurement, this result shows evidence of evaporation and significant loss of Zn from only AlTi$_{0.45}$CuZn-650. The as-milled sample is indicated by 25 °C room temperature.
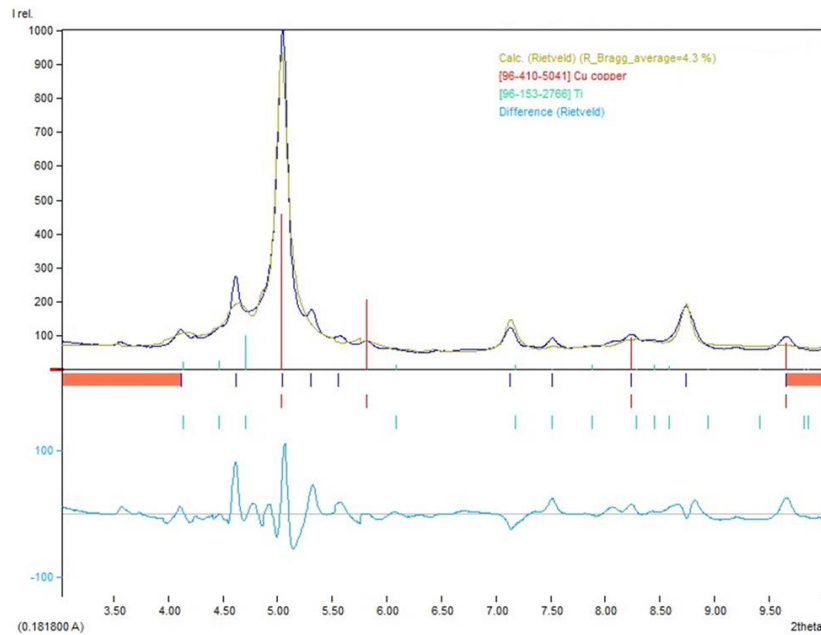
Figure A2: Rietveld refinement analysis plot of the s-XRD pattern of AlTi$_{0.45}$CuZn LHEA annealed at 250 °C, where 2θ was used instead of q. Cu and Ti indicate FCC and HCP crystal structures, respectively. The R_{wp} factor has a value of 4.3%.

Copyright Permission

Figures 1.1(a) is reproduced from Y. Zhang, History of High-Entropy Materials, in: High-Entropy Mater., 1st ed., Springer Singapore, Singapore, 2019: pp. 1–31. https://doi.org/10.1007/978-981-13-8526-1.

Figures 1.1(b) is reproduced from W. Zhang, P.K. Liaw, Y. Zhang, Science and technology in high-entropy alloys, Sci. China Mater. 61 (2018) 2–22. https://doi.org/10.1007/s40843-017-9195-8.

Figures 1.2(a-d) is reproduced from E.P. George, D. Raabe, R.O. Ritchie, High-entropy alloys, Nat. Rev. Mater. 4 (2019) 515–534. https://doi.org/10.1038/s41578-019-0121-4.

Figures 1.3(a-c) are reproduced from Y. Zhang, Y.J. Zhou, J.P. Lin, G.L. Chen, P.K. Liaw, Solid-Solution Phase Formation Rules for Multi-component Alloys, Adv. Eng. Mater. 10 (2008) 534–

538. https://doi.org/10.1002/adem.200700240.

Figures 1.4 is reproduced from J.-W. Yeh, S.-K. Chen, S.-J. Lin, J.-Y. Gan, T.-S. Chin, T.-T. Shun, C.-H. Tsau, S.-Y. Chang, Nanostructured High-Entropy Alloys with Multiple Principal Elements: Novel Alloy Design Concepts and Outcomes, Adv. Eng. Mater. 6 (2004) 299–303. https://doi.org/10.1002/adem.200300567.

Figures 1.5 is reproduced from W. Li, D. Xie, D. Li, Y. Zhang, Y. Gao, P.K. Liaw, Mechanical behavior of high-entropy alloys, Prog. Mater. Sci. 118 (2021) 100777. https://doi.org/10.1016/j.pmatsci.2021.100777. The publisher has a Creative Commons policy, and users can use the content for non-commercial purpose with attribution.

Order Completed

Thank you for your order.

This Agreement between University of Calgary -- Intekhab Alam ("You") and Elsevier ("Elsevier") consists of your license details and the terms and conditions provided by Elsevier and Copyright Clearance Center.

Your confirmation email will contain your order number for future reference.

🖶 Printable Details

License Number	5672291153406
License date	Nov 19, 2023

✅ **Licensed Content**

Licensed Content Publisher	Elsevier
Licensed Content Publication	Progress in Materials Science
Licensed Content Title	Mechanical behavior of high-entropy alloys
Licensed Content Author	Weidong Li,Di Xie,Dongyue Li,Yong Zhang,Yanfei Gao,Peter K. Liaw
Licensed Content Date	May 1, 2021
Licensed Content Volume	118
Licensed Content Issue	n/a
Licensed Content Pages	1

📋 **Order Details**

Type of Use	reuse in a thesis/dissertation
Portion	figures/tables/illustrations
Number of figures/tables/illustrations	1
Format	both print and electronic
Are you the author of this Elsevier article?	No
Will you be translating?	No

📄 **About Your Work**

Title of new work	Design, Development, and Examination of New Lightweight High-Entropy Alloy for Structural Applications
Institution name	University of Calgary
Expected presentation date	Dec 2023

📁 **Additional Data**

Portions	Figure 1.2 Diffusion coefficients of Ni in a series of FCC alloys including high-entropy alloys against the inverse homologous temperature

Figures 1.6 is reproduced from D.B. Miracle, O.N. Senkov, A critical review of high entropy alloys and related concepts, Acta Mater. 122 (2017) 448–511. https://doi.org/10.1016/j.actamat.2016.08.081. The publisher has a Creative Commons policy, and users can use the content for non-commercial purpose with attribution.